

# **Designing Diamond Adiabatic Quantum Computing Processors**

**Milan Leonard**

**A thesis submitted for the degree of  
Bachelor of Philosophy (Honours) - Science  
with Honours in Physics at  
The Australian National University**

**October 2021**

---

# Declaration

---

This thesis is an account of research undertaken between February 2021 and October 2021 at the Research School of Physics, The Australian National University, Canberra, Australia.

Except where acknowledged in the customary manner, the material presented in this thesis is, to the best of my knowledge, original and has not been submitted in whole or part for a degree at any other university.

---

Milan Leonard  
October 2021

---

# Acknowledgements

---

In my first three years of Uni whenever I would talk to someone doing their physics honours, I would see the despair in their eyes as they warned me either not to do it or to be prepared for a very painful year. That being said, with enough hands on deck any load can be shared, and is it by sharing the load that I have enjoyed this year.

A particular thanks must go to be supervisor Marcus, for teaching and hopefully sometimes being taught by me, and for laughing with and definitely sometimes at me. Without his help and oversight, I would never have been able to achieve writing this thesis. Most importantly however, without his friendship I wouldn't have had as many laughs this year as I have ended up having. This gratitude must also be extended to my group members, in particular Yun Heng, Sophie and Lachlan who helped directly with the thesis, and Liam who showed me the best places to go and eat.

Special mentions must go to Angus and Micheal, my fellow Honours students in my group, who happily listened to many hours of my nonsense and who, even as the due date drew near, would happily jump into a call with me to make sure what I was saying sounded sensible, and to make sure I kept my sanity.

---

# Abstract

---

Quantum computing promises to launch humanity into a new age of computational ability. To achieve this end, there is competition in developing two types of quantum computation, adiabatic, and gate-based. Furthermore, there is much competition in executing these two types on many different quantum systems. Currently, the majority of effort is being expended into developing gate-based quantum computing, due to its stronger theoretical foundations. As part of this effort, the Nitrogen-Vacancy Centre in diamond is a forerunner for a potential gate-based quantum computer, based on its ability to operate at room temperature, and clear paths being laid out for scaling and manufacturing. However, the engineering and algorithm development problems involved with gate-based quantum computing make utilising them in the near-term difficult. Therefore, adiabatic quantum computation could produce immense value as an intermediate technology. Currently, the only commercially available adiabatic quantum computer, from D-Wave, is built using a particular quantum system, the superconducting flux qubit. Understanding which, if any, of the many other quantum systems could be used for adiabatic quantum computation requires understanding what differentiates adiabatic quantum computer designs.

This thesis addresses the above problem by proposing and evaluating designs of an adiabatic quantum computer that use the Nitrogen-Vacancy Centre in diamond as its quantum system. This is done in two stages, firstly in the ideal case that would require atom-precise fabrication, and secondly leveraging existing manufacturing techniques to allow for near-term construction. This design is then optimised computationally, where even without simple possible engineering improvements it performs as well as the D-Wave device. I then compare the ideal and realistic designs against D-Wave's physical quantum computer using Instance Space Analysis. This highlighted the major difficulties in comparing with the D-Wave device, which made comparisons between the diamond simulation and the D-Wave device extremely challenging. Fortunately, the comparison between ideal and diamond showed promising results, indicating that the diamond quantum computer would scale better than competing technologies.

---

# Contents

---

<b>Declaration</b>	<b>ii</b>
<b>1 Introduction</b>	<b>2</b>
<b>2 Background</b>	<b>7</b>
2.1 The Basic Building Block - Qubits . . . . .	7
2.2 Extending to Multiple Qubits . . . . .	9
2.3 Qubit Connectivity Graphs . . . . .	11
2.4 Sources of Quantum Noise . . . . .	12
2.4.1 Equivalence between dephasing and inhomogeneous broadening .	15
2.5 Gate-Based Quantum Computing . . . . .	16
2.6 Adiabatic Quantum Computation and the Adiabatic Theorem . . . . .	19
2.7 Quantum Annealing and Quadratic Unconstrained Binary Optimisation Problems . . . . .	21
2.8 The Nitrogen-Vacancy Centre in Diamond . . . . .	23
2.8.1 The Structure and Quantum Properties of the NV Diamond Quantum Processor . . . . .	24
2.8.2 Creating NV Centres (Semi-)Deterministically . . . . .	28
2.9 Instance Space Analysis . . . . .	29
<b>3 Design for an Ideal Diamond Quantum Annealer Using an Array of N-V Centres</b>	<b>33</b>
3.1 Array of Diamond N-V Centres . . . . .	33
3.2 Derivation of the Quantum Annealing Hamiltonian from the N-V Hamiltonian . . . . .	36
3.2.1 Example of the Transformations on a Single Qubit . . . . .	36
3.2.2 Deriving the Full Annealing Hamiltonian with Multiple N-V Centres . . . . .	41
3.3 The Possible Qubit Connectivity Graphs . . . . .	44
<b>4 Using Ensembles of Diamond NV Centres as Effective Qubits</b>	<b>47</b>
4.1 Effective Qubits . . . . .	47
4.2 The Design for a Diamond Quantum Computer based on Effective Qubits	49

4.3 Optimising the Geometry for the Quality Factor . . . . .	53
4.4 Implications and Avenues for Future Work . . . . .	56
<b>5 Understanding the Diamond Quantum Annealer compared to D-Wave Advantage and an Ideal Quantum Annealer through Instance Space Analysis</b>	<b>57</b>
5.1 The Maximum Cut Problem . . . . .	57
5.2 Methods . . . . .	59
5.3 Projecting the Instance Space into 2-Dimensions . . . . .	60
5.4 How Legitimate are Comparisons to the D-Wave Device? . . . . .	62
5.5 The Computational Cost of Decoherence . . . . .	63
<b>6 Conclusion</b>	<b>67</b>
<b>Bibliography</b>	<b>73</b>

# Introduction

---

As soon as an Analytical Engine [Computer] exists, it will necessarily guide future course of the science. Whenever any result is sought by its aid, the question will then arise — by what course of calculation can these results be arrived at by the machine in the shortest time?

---

*Charles Babbage*  
*Life of a Philosopher* (1864) [1]

Quantum computing (QC) has the potential to be one of the most revolutionary technologies of the 21<sup>st</sup> century. By leveraging quantum mechanics, quantum computing promises to dramatically expand the space of computational problems that we can solve. While the true magnitude of its importance is hard to predict, there are quantum algorithms, such as Shor’s algorithm, which have been mathematically proven to reduce the computing time from billions of years on a classical computer to fractions of a second on a quantum computer [2]. With enormous competition between countries and companies using various underlying technologies, asking the right research questions and exploiting the benefits of these different approaches will be critical for accelerating the development of these promising devices.

The potential impact of quantum computers is brought further into clarity when considering the difficulties faced for current classical computing. Since the invention of silicon integrated circuits (in particular, the MOSFET) by Bell Labs in 1959 [3], there has been a continuous exponential improvement in the power of classical computing hardware (Moore’s Law) [4]. To continue Moore’s law in its original formulation, transistor sizes will need to continue to shrink. To achieve this, photolithographic techniques have moved to extreme ultraviolet technologies, which highlights classical computing’s approach of the physical limits, both in terms of quantum electron tunnelling effects, and in terms of silicon’s optical properties [5]. Over the next three years, TSMC, the world’s largest and highest performing semiconductor manufacturer, will spend 100 Billion USD on production and research and development to continue pushing the boundary. This is on average more than double its annual spend from 2016 to 2019 [6]. Furthermore, the total energy consumption and environmental impact of supercomputers is becoming unsustainable, with individual large supercomputers using as much energy as tens of thousands of average households [7]. Quantum computing is

emerging at a perfect time to help humanity achieve its computational goals without the economic or environmental cost of improving and scaling the existing technologies.

The current state of quantum computing is comparable to the early days of classical computing when bits were physically represented using thermionic valves. During this time, sources of physical noise in analog signals were frequent causes of errors, the devices themselves were large, consumed lots of power, expensive, and had extremely few accessible bits. This stopped early computer scientists from being able to work at high levels of abstraction and also forced them to deeply understand the inner workings of the physical device to find success. This is exactly the current situation for quantum computation scientists. Despite this, early computers still had major applications in all of scientific, military, and business endeavours. Similarly, this is the hope for current quantum computers. Due to the importance of noise and the intermediate-scale of existing devices, we call the current era of quantum computation the Noisy Intermediate-Scale Quantum (NISQ) era [8]. Whilst in 2018 quantum computers demonstrated an advantage over their best classical counterparts [9], a major milestone for the field will be the discovery of a *useful quantum advantage*, where a quantum computer makes a meaningful contribution to society that would be currently impossible on existing devices.

There are three major challenges that must be solved to graduate from the NISQ era. Firstly, the impact of noise and analog error will need to be drastically reduced. This will likely be achieved through the use of quantum error correction codes [10, 11] and improvements in quantum device engineering. Secondly, we will need to improve our ability to imprint classical data into a quantum state, thereby giving us access to a quantum RAM (qRAM)[12]. While it seems likely that there will be important limitations as to which data can be represented efficiently, understanding this boundary will be crucial to understanding which of the proposed quantum algorithms will be successful. Lastly, as the number of qubits increase, we will need to improve our ability to ‘entangle’, or connect, distant qubits, through improving our understanding of qubit connectivity graphs [13].

There are important fundamentally different types of quantum computer that are being developed. These are gate-based quantum computing, and adiabatic quantum computing (AQC).

Gate-based quantum computers function similarly to classical computers, using atomic operations to transform from one explicit state to another [14]. To design algorithms that run on a gate-based quantum computer (quantum algorithm), the programmer must make explicit use of quantum superposition and entanglement. This has meant that quantum algorithm development is a slow and difficult process. This has produced work into automatic generation of quantum algorithms using machine

learning techniques discussed in Section 2.5. Whilst this is still a very productive and promising research direction, there are remaining open questions that pose an existential threat to their wide applicability [15, 16].

Adiabatic quantum computers instead operate as analog computers, leveraging the behaviour of underlying physical laws to perform computation instead of performing specific operations on specific (qu)bits [17]. Specifically, they take advantage of the adiabatic theorem, which theoretically allows for the discovery of the ground state of a vast range of quantum Hamiltonians. Therefore, if the solution to an interesting problem can be written such that it must be the ground state of a Hamiltonian, then adiabatic quantum computers should be able to find that ground state. However, the theoretical foundation for AQC is much weaker than for gate-based QC, with limited knowledge of how these quantum computers will scale with extra qubits, or as to whether they will be able to demonstrate a quantum advantage. The computational power of AQC is a field of active research in both empirical studies and theoretical quantum mechanics. Despite this, adiabatic quantum computers are known to be particularly attractive for the NISQ era because:

1. they are resilient to certain sources of noise that plague gate-based quantum computers.
2. they are simpler to manufacture.
3. the algorithm development process is trivially simple compared to gate-based quantum computers.

Currently the major research in AQC is driven by D-Wave [18, 19, 20], who are building a quantum annealer, a specific type of AQC. Quantum annealing will be covered in Section 2.7. Importantly, the experimental and theoretical evidence for whether D-Wave is actually taking advantage of quantum effects is subject to vigorous debate [21, 22, 23], which highlights the need for the construction of a new device that is demonstrably quantum mechanical by nature. It is known that quantum annealers cannot perform all of the computations as in AQC or gate-based QC [19, 24, 17]. Despite this, we know that it solves many interesting problems that classical computers struggle to perform, and can become universal with slight modifications [25].

The NV Centre in diamond has established itself as a potential major competitor in the race to build a quantum computer. With the longest electronic spin coherence time of a defect in any solid at room temperature [26], it allows for applications of quantum computation that cannot be competed with. In particular, by running at room temperature, its applications are not relegated to a data centre, and as such could be used in mobile phones, cars, planes or satellites which would otherwise not be

able to do real-time processing on a quantum computer. Furthermore, it has a different set of challenges that seem intrinsically less difficult than of some other technologies. In particular, as explored in this thesis, decoherence doesn't necessarily scale with size, which is a major problem of superconducting flux qubits that need to operate in super-cold environment [27].

Since there are limited resources in research, understanding whether to invest in gate-based quantum computers or adiabatic quantum computers will enable better decision-making that will accelerate quantum computation development. Currently, the vast majority of these resources are being deployed towards gate-based quantum computers because concrete claims can be made about an algorithm's performance and the relative performance of one device to another. Alternatively, it is unclear whether the adiabatic theorem can be exploited for quantum advantage. Furthermore, there is a lack of ability to compare different implementations of adiabatic quantum computers. This is of particular importance, because it makes it difficult for researchers to know whether it is worthwhile to convert a gate-based quantum computer based on some underlying technology into an adiabatic quantum computer and compete with the existing technologies..

This thesis compares the viability of adiabatic quantum computers to one another as well as to gate-based quantum computers. This will provide future quantum engineers a guide and a set of metrics for producing an adiabatic quantum computer, and determining whether it is worthwhile attempting to construct it. In particular, the thesis will provide frameworks which answer:

1. how physical properties of different quantum systems affect their ability to perform quantum annealing.
2. how to prioritise trade-offs between noise and qubit connectivity.
3. how to model non-quantum effects, most importantly thermal relaxation.

To do so, I will propose the first design for a quantum annealer using the NV-Centres in diamond and compare this design both in terms of physical parameters and via numerical simulations to competing device designs. This will proceed as follows.

In Chapter 2, I will provide the information required to understand the rest of the thesis. In particular, I provide the theoretical foundations for quantum computing and describe gate-based approaches are so promising, however also highlighting the large shortcomings which makes their realisation in the near-term high risk. Then, I explain how adiabatic quantum computing solves some of the major challenges facing quantum computing more broadly. Furthermore, I introduce computational complexity discussions which play a key role in understanding the limitations of AQC. I then

introduce the idea of quantum annealing, and explain why the theoretical and experimental results within the field are on unstable foundations, but highlight its potential applications for near-term advantages over gate-based approaches. Lastly, I introduce the NV Centre in diamond, a candidate technology for quantum computation, through discussing its optical and quantum mechanical properties that allow for it to be used as a quantum computer. Furthermore, I introduce the different fabrications, both proposed and existing, that will become relevant in Chapters 3 and 4.

In Chapter 3, I discuss the current approach for building a diamond gate-based quantum computer that assumes atom-scale fabrication capability. In this chapter, I present the first derivation showing how the NV Centre spin Hamiltonian introduced in Section 2.8 can be converted into the quantum annealing Hamiltonian. Furthermore, I discuss some of the limitations that exist in scaling the current design. With the assumption of atom-scale fabrication, I will describe exactly how a grid of NV Centres can be used as a quantum annealer.

However, producing this grid is currently impossible using current manufacturing techniques. I will overcome this obstacle through introducing a design for fabricating an annealer using existing fabrication techniques in Chapter 4. I introduce the concept of ‘effective qubits’, and show how region-based frequency selection can be leveraged to create them natively in diamond. I then analyse the costs of this design, specifically in terms of the inhomogeneous broadening created, and justify these costs relative to the state-of-the-art devices. This design will be parameterised, and therefore can be optimised to maximise or minimise a metric. I will define this metric, and then perform this optimisation.

Finally, in Chapter 5 I will perform the first Instance Space Analysis comparing different types of adiabatic quantum computers by using the common benchmark problem, Maximum Cut, and compare an ideal quantum annealer, the diamond quantum annealer, and D-Wave’s Advantage physical device accessed through their online Leap service. This will provide evidence as to whether D-Wave’s devices, which operate at milliKelvin temperature and so leverage thermal effects, view the difficulty of a particular problem in the same way as other quantum annealers that would operate without thermal effects. Furthermore, by comparing the diamond annealer and an ideal annealer, I aim to understand exactly what are the costs of decoherence to a quantum annealer.

---

# Background

---

At its core, quantum computing uses superposition and entanglement of coupled 2-state quantum systems (qubits). The aim of this section is to introduce each of these components, and to demonstrate how they enable advantages for computational tasks. This section does not aim to describe or derive the underlying quantum mechanics, but instead highlight how quantum mechanical principles translate to computation.

To do so, I will make use of the direct equivalence between quantum mechanics and linear algebra. For the linear algebra, I will be making use of *Dirac notation* and be defining the *computational basis*, where  $|0\rangle := (1, 0)^T$  and  $|1\rangle := (0, 1)^T$ , giving a complete basis for a 2-dimensional space.

The following two sections are a summarisation of the relevant information from Nielsen and Chuang (2000) [28].

## 2.1 The Basic Building Block - Qubits

A qubit is a two-state quantum system. There are many physical examples of this, one of which is the spin of an electron which can be only up or down. Since all two-state quantum systems are mathematically equivalent, we will discuss an abstract (or computational) two-state system; one with states  $\{|0\rangle, |1\rangle\}$ . When we measure a qubit in state  $|0\rangle$ , it returns the value 0, and when we measure a qubit in state  $|1\rangle$  it returns the value 1.

Quantum systems have the property that they can exist in ‘superposition’, the property of being in ‘multiple states at the same time’. This is simply that, unlike a bit in a classical computer which is exclusively binary, i.e. *either* 0 or 1, a qubit is a mathematical object written as

$$|\Psi\rangle = \alpha|0\rangle + \beta|1\rangle = \begin{pmatrix} \alpha \\ \beta \end{pmatrix}. \quad (2.1)$$

In the above equation,  $\alpha$  and  $\beta$  are complex numbers called *probability amplitudes*. When we perform a measurement of a qubit, we never see the superposition. Instead, it will appear to be in state  $|0\rangle$  with probability  $|\alpha|^2$  and in state  $|1\rangle$  with probability

$|\beta|^2$ . Since probabilities must sum to 1, this adds the constraint

$$|\alpha|^2 + |\beta|^2 = 1. \quad (2.2)$$

Due to this probabilistic nature, the outcome of a quantum computer is *probabilistic* and *stochastic*, dictated by complex-valued entries which can be written as a vector.

This gives rise to a linear improvement in the number of bits needed to encode a variable. For example, if we wanted to store an integer,  $\lambda$ , between the values 0 and 255, we would use 8 bits to do so. On a qubit however, we can store this as

$$|\Psi\rangle = \sqrt{1 - \lambda} |0\rangle + \sqrt{\lambda} |1\rangle. \quad (2.3)$$

However, to then extract the value of  $\lambda$  from the quantum computer, we would need to run many *computational shots* and use statistics to get a predicted value and a confidence in that value.

This highlights two important design considerations for quantum algorithms. Firstly, they should not require high precision in the coefficients of the individual qubits, since sources of error will make this initialisation difficult. Secondly, the solution to the computational problem should not depend upon a detailed understanding of the final probability distribution, and should instead concentrate the probability density into few states. If the answer relies on knowing the probability distribution, then an exponentially large number of shots will be required to build up a statistical picture of this distribution.

Since a qubit is represented by a vector in  $\mathbb{C}^2$ , operations on qubits are represented by matrices in  $\mathbb{C}^{2 \times 2}$  called *operators*. The most important of these operators is the Hamiltonian, usually denoted  $\hat{H}$ , as this determines the evolution of the qubit according to the Schrodinger equation

$$i\hbar \frac{\partial}{\partial t} |\Psi(t)\rangle = \hat{H} |\Psi(t)\rangle. \quad (2.4)$$

Hamiltonians have the property that their eigenvalues correspond to energies of specific states. Since we never measure complex energies, this means that the eigenvalues must be real. The set of complex-valued square matrices with real eigenvalues are called *Hermitian* matrices, with the condition that the matrix is equal to its conjugate transpose, denoted  $\dagger$ , as in

$$\hat{H}^\dagger = \hat{H}. \quad (2.5)$$

The solution to the Schrodinger equation (for a stationary Hamiltonian) is then

immediately

$$|\Psi(t)\rangle = e^{i\hat{H}t} |\Psi(0)\rangle. \quad (2.6)$$

The set of matrices that can be expressed as  $\hat{U} = e^{i\hat{H}}$  for a Hermitian matrix  $\hat{H}$  are called *unitary matrices*, and have the property that

$$\hat{U}^\dagger \hat{U} = \hat{U} \hat{U}^\dagger = \mathbb{1}, \quad (2.7)$$

where  $\mathbb{1}$  is the identity matrix with correct dimension.

Since this equation governs the evolution of qubits, designing a physical quantum computer depends on being able to apply different Hamiltonians that will cause the desired evolution of the qubits. The first layer of abstraction is through the use of *gates*, which describe the change in state of applying a specific Hamiltonian for a fixed amount of time. This allows for descriptions of quantum algorithms that are hardware independent. All of these gates must therefore be able to be written as  $\hat{U}_\lambda = e^{i\hat{H}_\lambda t}$ , and are therefore all unitary.

Some of the most common quantum gates are shown in Equations 2.8 to 2.14.

$$\hat{H} = \frac{1}{\sqrt{2}} \begin{pmatrix} 1 & 1 \\ 1 & -1 \end{pmatrix} \text{ The Hadamard Gate} \quad (2.8)$$

$$\hat{X} = \begin{pmatrix} 0 & 1 \\ 1 & 0 \end{pmatrix} \text{ The X Gate} \quad (2.9)$$

$$\hat{R}_X(\theta) = \begin{pmatrix} \cos\left(\frac{\theta}{2}\right) & -i \sin\left(\frac{\theta}{2}\right) \\ -i \sin\left(\frac{\theta}{2}\right) & \cos\left(\frac{\theta}{2}\right) \end{pmatrix} \text{ The X rotation gate} \quad (2.10)$$

$$\hat{Y} = \begin{pmatrix} 0 & -i \\ i & 0 \end{pmatrix} \text{ The Y Gate} \quad (2.11)$$

$$\hat{R}_Y(\theta) = \begin{pmatrix} \cos\left(\frac{\theta}{2}\right) & -\sin\left(\frac{\theta}{2}\right) \\ \sin\left(\frac{\theta}{2}\right) & \cos\left(\frac{\theta}{2}\right) \end{pmatrix} \text{ The Y rotation gate} \quad (2.12)$$

$$\hat{Z} = \begin{pmatrix} 1 & 0 \\ 0 & -1 \end{pmatrix} \text{ The Z Gate} \quad (2.13)$$

$$\hat{R}_Z(\theta) = \begin{pmatrix} e^{-\frac{i\theta}{2}} & 0 \\ 0 & e^{\frac{i\theta}{2}} \end{pmatrix} \text{ The Z Rotation Gate.} \quad (2.14)$$

## 2.2 Extending to Multiple Qubits

To describe multiple qubits we need to introduce one more mathematical object, the *tensor product* and *tensor product space*. Formally, the tensor product is a binary

operation that takes two abstract vector spaces (over the same field) and maps them to a third vector space. It is denoted by

$$\otimes : V, W \rightarrow Q. \quad (2.15)$$

It has the properties that the dimensions of the spaces multiply, such that for example if  $\dim(V) = m$ ,  $\dim(W) = n$ , then  $\dim(Q) = m \times n$ . Furthermore the vector space has basis that is the tensor product of each of the component vector spaces as in

$$V = \text{span}(\{\mathbf{v}_i\}) \quad (2.16)$$

$$W = \text{span}(\{\mathbf{w}_j\}) \quad (2.17)$$

$$V \otimes W = \text{span}(\{\mathbf{v}_i \otimes \mathbf{w}_j\}), \quad (2.18)$$

where the lower indices can range freely across their respective dimensions.

To simplify notation the following are all equivalent representations.

$$|0\rangle \otimes |0\rangle \equiv |0,0\rangle \equiv |00\rangle. \quad (2.19)$$

If we bring two qubits together, each with basis  $Q = \text{span}(\{|0\rangle, |1\rangle\})$ , they multiply according to the tensor product to give a resultant space

$$Q \otimes Q = \text{span}(\{|00\rangle, |01\rangle, |10\rangle, |11\rangle\}). \quad (2.20)$$

The state of the two qubits is now described as

$$|\Psi\rangle = a_{00}|00\rangle + a_{01}|01\rangle + a_{10}|10\rangle + a_{11}|11\rangle, \quad (2.21)$$

which still has to obey the normalisation constraint for probability that  $\sum_i |a_i|^2 = 1$ . This gives rise to the second type of quantum advantage, which is that to describe  $n$  qubits, you need a vector of  $2^n$  probability amplitudes. This allows for *super-dense encoding*, where a dataset of length  $N$  of values  $\{\lambda_i\}$  is imprinted onto the probability amplitude of the  $i^{\text{th}}$  state, using  $\log_2(N)$  qubits, or exponentially fewer bits than to do so on a classical computer.

Operations on multiple qubits are described by the *Kronecker product*, which is also denoted  $\otimes$  and is defined by

$$\begin{pmatrix} a & b \\ c & d \end{pmatrix} \otimes \begin{pmatrix} e & f \\ g & h \end{pmatrix} = \begin{pmatrix} ae & af & be & bf \\ ag & ah & bg & bg \\ ce & cf & de & df \\ cg & ch & dg & dh \end{pmatrix}. \quad (2.22)$$

Under the Kronecker product, we can see that an operation on any of the individual qubits has an effect on the entire vector. This gives rise to the first type of quantum parallelism, where an operation on a single qubit allows for a transformation on the entire state.

This section has so far introduced the ways in which ideal quantum computers take advantage of quantum superposition and entanglement to generate three types of advantage. Firstly, a linear advantage through having access to continuous variables. Secondly, an exponential advantage through being able to encode  $2^n$  classical variables onto  $n$  qubits using super-dense encoding. Lastly, an exponential advantage through quantum parallelism, where operations on single qubits affect an exponentially long vector. This section also introduced the idea of computational shots in its discussion of the fundamental limit to the ability to determine the underlying state through the probabilistic and stochastic measurement process, which meant that there was always uncertainty in the statistically constructed distribution of the underlying probabilities of each state. We will now discuss two of the major research questions that are problematic to the development of quantum computers; in qubit connectivity and quantum noise.

## 2.3 Qubit Connectivity Graphs

In a real quantum computer there is a limit to our ability to couple qubits together. For example, consider the Ising model

$$\hat{H} = \sum_{i,j} J_{ij} \hat{Z}_i \hat{Z}_j. \quad (2.23)$$

Here, the nonzero terms of  $J$  are realised using programmable *couplers*. To be able to realise this coupling on a real quantum computer, we need to have the same term in our physical Hamiltonian describing the quantum system. However, in reality these couplings only exist between qubits that are physically close to each other. Qubit connectivity graphs are used to represent the possible couplings between qubits.

Consider the simplest non-trivial example, with a fully connected Ising Hamiltonian with 3 qubits

$$\hat{H} = J_{01} \hat{Z}_0 \hat{Z}_1 + J_{12} \hat{Z}_1 \hat{Z}_2 + J_{02} \hat{Z}_0 \hat{Z}_2. \quad (2.24)$$

Now, consider Fig. (2.1). Due to the physical placement of the qubits in the left graph (the nodes in the graph), it is not possible to realise the coupling term  $J_{02}$ . However, if we add an additional qubit and have connectivity like the right graph, then we can logically set some qubits to be identical, and add a connection between qubit 0 and qubit 2, along with a duplicated 0 element in the right graph. Theoretically, this is

done by making the coupling between logically identical qubits infinitely large. The process of embedding a smaller graph into a larger fixed graph with repeated nodes such that the two graphs are equivalent is the *minor embedding* problem [29], and is not universally possible. Therefore, designing a qubit connectivity graph which is both dense (has many connections) and which can accommodate a large range of minor embeddings is crucial to building a useful quantum computer.

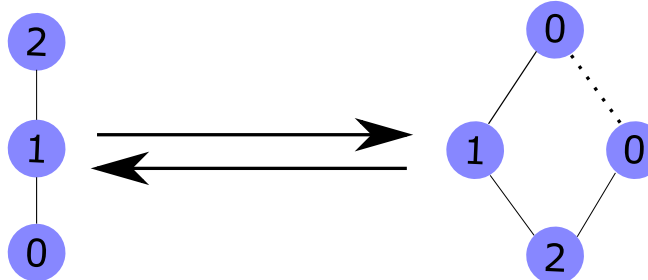


Figure 2.1: It is impossible to realise Eq. (2.24) given the left qubit connectivity graph. However, by introducing a fourth physical qubit (right) we can clearly see that we could contract over the dashed edge to find a minor embedding of a fully connected graph and realise the previously impossible connection.

When the coupling is infinitely large, then the quantum systems are perfectly degenerate, and will operate truly as a single quantum system. However, in reality the coupling can never be infinitely large, and as such they will be non-degenerate. This highlights a major problem in minor embedding, which is that with each additional qubit there are twice as many distinct energy levels, which will naturally decrease an important parameter, the minimum gap, explored in Section 2.6. This will have major implications for both quantum annealing and gate-based quantum computing which will be discussed in their respective sections.

It has been shown that it is possible to embed a fully connected qubit connectivity graph with  $N$  nodes into a square lattice graph with  $N(N - 1)/2 \sim O(N^2)$  nodes[13]. However, this technique has major caveats discussed in Section 3.3. An example of the qubit connectivity graph used by D-Wave's previous generation of quantum annealers is shown in Fig. (2.2).

## 2.4 Sources of Quantum Noise

In this section I will introduce some of the relevant sources of noise plaguing quantum computers and highlight a specific duality between types of noise that I will exploit in Chapter (4). There are two important types of quantum noise.

1. *error*, characterised by the quantum computer not behaving the way logically

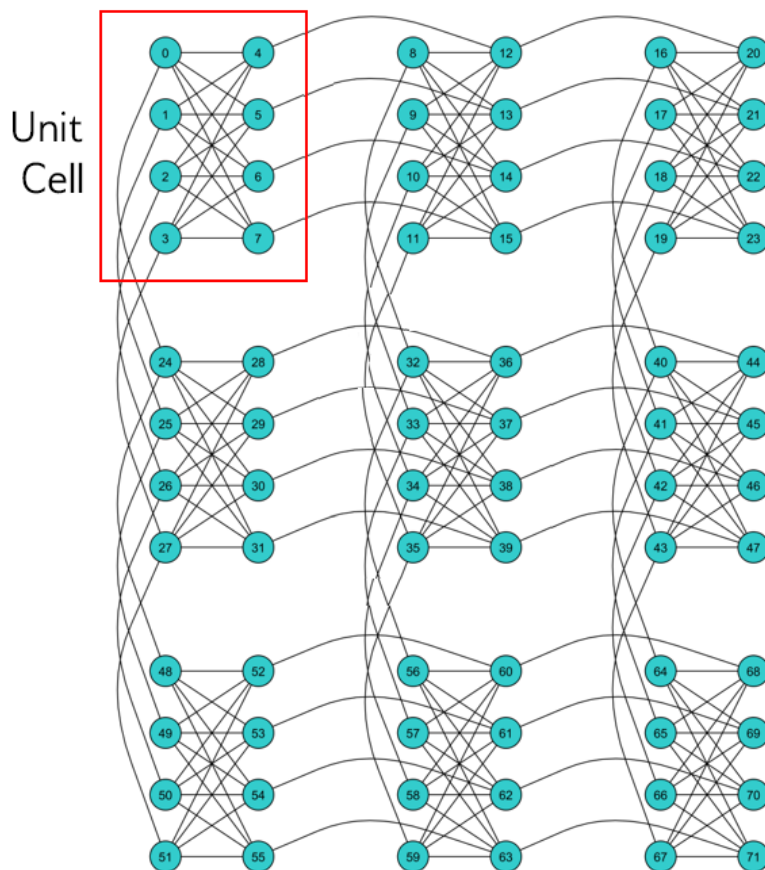


Figure 2.2: D-Wave's previous generation qubit connectivity graph, called the Chimera graph, involves highly connected (formally,  $K_{4,4}$  complete bipartite) cells repeated. Due to the less restrictive requirements for a quantum annealer [30], they can have much denser and larger qubit connectivity graphs.

specified.

2. *decoherence*, an intrinsic and unavoidable deterioration of the quality of qubits over time.

The types of error I will introduce *initialisation* error, *readout* error, and *control* error. The decoherence process is mainly driven by *dephasing* and *relaxation*.

To describe the statistics of error processes we make use of the *density matrix* formulation of quantum mechanics. Starting with a quantum mechanical state  $|\Psi_1\rangle$ , then the density matrix corresponding to  $\Psi_1$  is given by

$$\hat{\rho}_1 = |\Psi_1\rangle \langle \Psi_1|. \quad (2.25)$$

Density matrices are usually not used to describe a single state, but instead are used to describe a probabilistic ensemble of quantum states. That is, they describe the overall statistics of running a quantum mechanical calculation beginning with a collection of different states  $|\Psi_i\rangle$  with probability  $p_i$ . This gives the final density matrix as

$$\hat{\rho} = \sum_i p_i \hat{\rho}_i = \sum_i p_i |\Psi_i\rangle \langle \Psi_i|. \quad (2.26)$$

The density matrix evolves according to the *Linblad master equation*

$$\frac{d\hat{\rho}}{dt} = -i[\hat{H}, \hat{\rho}] + \sum_i \gamma_i \left( \hat{L}_i \hat{\rho} \hat{L}_i^\dagger - \frac{1}{2} \{ \hat{L}_i^\dagger \hat{L}_i, \hat{\rho} \} \right) \quad (2.27)$$

$$= i[\hat{H}, \hat{\rho}] + \sum_i \gamma_i \mathcal{L}(\hat{L}_i). \quad (2.28)$$

where  $[\hat{A}, \hat{B}]$  and  $\{\hat{A}, \hat{B}\}$  are the commutator and anti-commutator respectively. The first term is directly equivalent to evolution under the Schrodinger equation, and the second term corresponds to modelling environmental effects, which in the context of quantum computing is modelling decoherence. The second term has two free parameters. First, the strength  $\gamma_i$  of the decoherence channel, which controls how rapidly the system decoheres according to the second free parameter, the choice of the operators  $L_i$  in  $\mathcal{L}(L_i)$  that induce environmental effects.

There are three main types of error; initialisation, readout, and control error. Initialisation error and readout error are the process by which the state of a qubit is incorrectly initialised or read out. Since initialisation and readout each happen only once, these are modelled by transforming the density matrix once before and once after the computation. Control error comes about when various sources of noise come into the control mechanisms for the qubit, and usually have the effect of increasing the strength of certain decoherence parameters.

There are two major types of decoherence; dephasing and relaxation. Dephasing is the process by which the phase information of a qubit is randomised, limiting an algorithm's ability to exploit the interference of the wave-like nature of quantum mechanics. Dephasing is modelled by adding a Lindblad term  $\gamma_{\text{dephasing}} \mathcal{L}(\hat{Z})$ . The decoherence time for dephasing is

$$T_2 = \frac{1}{\gamma_{\text{dephasing}}} \quad (2.29)$$

Relaxation is the process by which energy is exchanged with an environment. For example, if you leave the quantum system for long enough, it will enter an equilibrium state with the thermal bath, where the distribution over the states will follow the Boltzmann distribution. This is modelled by raising and lowering operators on the qubits as

$$\Gamma \left( \frac{e^{-\Delta E/k_b T}}{1 + e^{-\Delta E/k_b T}} \mathcal{L}(|1\rangle\langle 0|) + \frac{1}{1 + e^{-\Delta E/k_b T}} \mathcal{L}(|0\rangle\langle 1|) \right), \quad (2.30)$$

where  $\Gamma$  is the overall decoherence rate,  $\Delta E$  is the qubit energy difference.

#### 2.4.1 Equivalence between dephasing and inhomogeneous broadening

A specific result that will be important in Chapter 4 is the equivalence between pure dephasing and inhomogeneous broadening, which is shown here.

In a physical system, there is no single, well-defined time-independent energy gap of a single qubit. In reality, there is a statistical distribution of the energy gap. This is generated by an underlying Markovian process, which could include vibrations due to temperature, or many other effects. Since the underlying mechanism is Markovian, when we take the time-average of the transition energy this produces the Lorentzian lineshape of the power spectrum, with functional form

$$\omega_0 \sim \frac{1}{2\pi} \frac{\gamma}{(\omega_0 - \bar{\omega})^2 + (\gamma/2)^2}. \quad (2.31)$$

This creates a pure dephasing that depends on the scale parameter of the Lorentzian, which is also the rate of pure dephasing

$$\mathcal{L}_{\text{pure dephasing}} = \gamma \mathcal{L}(\hat{Z}). \quad (2.32)$$

Importantly, the only assumption here is that the lineshape of the power spectrum of the qubit was a Lorentzian function.

Instead of using a time-average to produce the Lorentzian distribution, we consider producing the distribution by having a collection of physical qubits. Supposing each of these physical qubits were degenerate, each would experience the same underlying time-averaged dephasing. However, if there was *inhomogeneous broadening* caused

by having distinct transitions, then there would also be a spatial distribution of the power spectrum. If this spatial distribution was a Lorentzian, then we could treat the collection of physical qubits as if they were a single qubit with an added pure dephasing term.

## 2.5 Gate-Based Quantum Computing

Gate-based quantum computing is a strategy by which quantum mechanical systems can be manipulated to obtain a guaranteed quantum advantage (if ideal). They were the computing devices used when Google claimed to have achieved quantum advantage in 2018[9]. As suggested by their name, they are specified fully by gates, described in Section (2.1). An example algorithm (with no practical application) on a two-qubit gate-based quantum computer is

$$(\hat{H} \otimes \hat{Z})(\hat{C}_X^{01})(\hat{\mathbb{1}} \otimes \hat{Y}) |00\rangle. \quad (2.33)$$

However, this is an unwieldy way to describe an algorithm, especially with a larger number of qubits. Instead, we represent them using a *circuit diagram*, such as in Fig. (2.3). Importantly, circuit diagrams are read left to right, whilst the matrix multiplication is read right to left. The convention for initialisation of a quantum computer is to drive it into the  $|0\dots0\rangle$  state, such that the probability amplitude vector looks like  $(1, 0, \dots, 0)^T$ . This means that to encode data into the quantum state, there needs to be a *state preparation* routine before executing the logic.

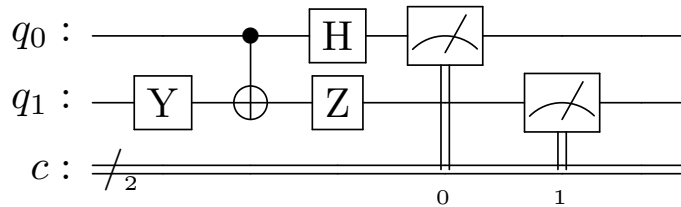


Figure 2.3: An example circuit diagram corresponding to Eq. (2.33). Circuit diagrams are used because they are simpler ways to describe gate-based quantum algorithms.

When we build a physical quantum computer, we will usually only have access to a subset of the total gates, called the *hardware-native gates*. To perform the rest of the gates, the algorithm goes through a compilation process to produce a (possibly approximate) representation in terms of the native gates. To do so, this leverages the Solobay-Kitaev theorem [31, 32], which states that an arbitrary gate (unitary, trace-preserving, in  $\mathbb{C}^{2 \times 2}$ ) operation, can be approximated by a relatively short sequence of

---

transforms as long as they come from a universal set of transforms. The length of this sequence  $M$  is related to the approximation precision  $p$  by

$$M = \log^{C_0} \frac{1}{p}, \quad C_0 \approx 3.97. \quad (2.34)$$

There are currently two types of quantum algorithms; hard-coded quantum algorithms and variational hybrid quantum-classical algorithms.

Hard-coded quantum algorithms are algorithms where each gate has been hand-selected by a quantum programmer. To come up with an algorithm, the programmer must make explicit use of the wave-nature of quantum mechanics. Currently, quantum programmers have to work ‘close to the metal’, not having access to many high-level programming constructs, meaning that the development process is slow, requires a deep understanding of quantum mechanics, and requires domain specialisation.

Importantly, there exist *only two* hard-coded quantum subroutines that have a provable quantum advantage over their classical counterpart. These are the quantum Fourier transform (QFT), leveraged by Shor’s algorithm, and Amplitude Amplification, leveraged by Grover’s search algorithm. However, even these algorithms’ ability to realise the advantage is brought into question. Shor’s algorithm is extremely sensitive to decoherence, meaning that until a quantum computer exists with many thousands (or millions) of high quality physical qubits this algorithm will not be able to outperform a classical computer. For QFT and Grover’s algorithm, it assumes access to a ‘quantum oracle’, which is an unspecified gate operation that applies a specific transformation that may or may not be implementable in an efficient manner.

The assumption of a quantum oracle or an arbitrary initial state is the *quantum RAM*, or qRAM problem. Many algorithms, for example QFT, require a quantum oracle before the ‘body’ of the algorithm to encode the classical data into a quantum state. This is *arbitrary state preparation*. It is known that to prepare  $N = 2^n$  complex probability amplitudes must have at least  $O(2^n)$  quantum gates [33], which implies that algorithms that arbitrarily take use of super-dense encoding will never obtain an exponential advantage. Whilst there is much active research into improving state preparation routines for specific cases, progress is slow, and the problem is hard. The commonly suggested solution, and the reason for its name, to the qRAM problem, is to attach the quantum computer to a physical quantum RAM, where the exponential effort is done upfront and qubits are initialised from the quantum state registers. Whilst practical designs have been suggested [12, 34], none of these designs scale well enough to be a total solution to the problem.

The second type of quantum algorithms are variation algorithms. To alleviate the problems associated with generating hard-coded quantum algorithms, these algorithms

are parameterised quantum circuits. To determine the parameters, they take advantage of the differentiability of quantum circuits with respect to the measurement statistics to perform a gradient descent or coordinate descent and find optimal parameters with respect to some task [35, 36]. This reduces the types of problems to *supervised learning tasks*, where there is an *objective function*. Fortunately, these are being invented alongside an explosion in classical optimisation techniques and where there is an enormous multitude of supervised learning tasks to perform.

This is an extremely promising and productive research endeavour, however there are major questions surrounding how variational algorithms will scale. In particular, there is the problem of barren plateaus, where for an enormous part of the possible initialisation space, the gradient information goes to zero exponentially as the number of qubits increases [15]. Secondly, the gradient of each parameter has to be calculated independently, which dramatically limits the number of logic gates that can be utilised [35]. With a smaller number of gates, the subset of useful transformations that can be approximated might be dramatically reduced.

Fig. (2.4) shows that the landscape of gate-based quantum algorithms has a deeply interconnected structure, and that breakthroughs will likely have carry-on effects. However, it also shows that the majority of algorithms depend on a technique with unknown performance, assume access to something which currently doesn't exist, or trade a quantum advantage for the ability to be implementable.

### Inheritance structure of quantum algorithms

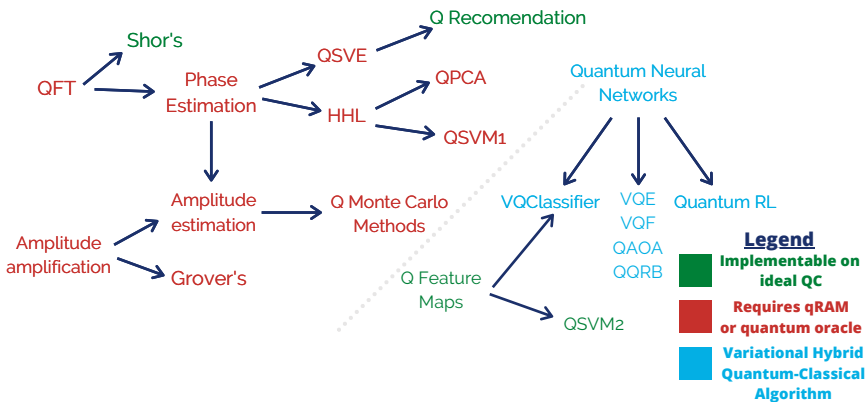


Figure 2.4: The inheritance structure of quantum algorithms. Only Shor's algorithm has a provable end-to-end quantum advantage, whilst the others might be able to handle larger or more complex operations.

For the reasons that constructing gate-based quantum computers is extremely difficult, and that there is an extremely limited number of existing algorithms that provide

a speedup, gate-based quantum computation seems to be a fair way off, and therefore the pursuit of intermediate technologies is important.

## 2.6 Adiabatic Quantum Computation and the Adiabatic Theorem

Adiabatic quantum computation (AQC) is principally different from the gate-based model, where instead of the computation being specified in terms of discrete operations, a physical analog of the computational problem is constructed. Instead of the problem being solved by a sequence of explicit operations, the problem is encoded into a model which has a particular construction, and every computation proceeds according to the same operation leveraging the *adiabatic theorem* [37].

The adiabatic theorem states that if a quantum system is prepared in the  $j^{\text{th}}$  eigenstate of an initial Hamiltonian  $H_0$ , then it will remain in the  $j^{\text{th}}$  eigenstate as long as all perturbations to the Hamiltonian occur *slowly enough*. There have been many iterations of the adiabatic theorem, focusing on what exactly ‘slowly enough’ means. The first was proposed by Born and Frock (1928), before being put on solid mathematical foundations by Kato (1950) [37]. The definition that I will use, in Eq. 2.36, is proposed by Amin (2009) [38], and focuses on the type of adiabatic evolutions that are generally considered in AQC. In AQC, we are almost always concerned with the ground state, and as such we will consider the initial eigenstate to be the ground state.

Adiabatic evolution in AQC works by interpolating between a time-independent initial Hamiltonian  $\hat{H}_i$  and a time-independent target Hamiltonian  $\hat{H}_f$ . The interpolating function, or *scheduling function*,  $s(t) : t \in [0, 1]$ , has a total annealing time  $t_f$ , and the interpolation proceeds as

$$\hat{H}(t) = (1 - s(\frac{t}{t_f}))\hat{H}_i + s(\frac{t}{t_f})\hat{H}_f, \quad (2.35)$$

with  $s(0) = 0, s(1) = 1$ . The adiabatic condition derived by Amin is

$$\frac{1}{t_f} \max_{s \in [0, 1]} \left( \frac{\langle \varepsilon_i(s) | \partial_s \hat{H}(s) | \varepsilon_j(s) \rangle}{|\varepsilon_j(s) - \varepsilon_i(s)|^2} \right) \ll 1 \quad \forall i \neq j. \quad (2.36)$$

However, this is only an approximate condition, as it does not provide strict lower bounds on the probability of being in the ground state after evolution in the general case.

In AQC, we consider only the time-dependent (possibly degenerate) ground and first excited state energies of  $\hat{H}(t)$ ,  $\varepsilon_0(t)$  and  $\varepsilon_1(t)$ .

In this case, it is generally enough to consider only the denominator of Eq. (2.36) where the instantaneous energy gap is

$$\Delta(s) = \varepsilon_1(s) - \varepsilon_0(s), \quad (2.37)$$

with minimum energy gap

$$\Delta = \min_{s \in [0,1]} \varepsilon_1(s) - \varepsilon_0(s). \quad (2.38)$$

This gives rise to an approximate adiabatic condition which suffices for the purposes of this thesis

$$t_f \gg \max_{s \in [0,1]} \frac{\langle \varepsilon_0(s) | \delta_s H(s) | \varepsilon_1(s) \rangle}{\Delta^2}, \quad (2.39)$$

giving rise to the widely accepted criterion that the timescale should be large relative to the inverse square of the minimum gap.

We know that there exists a direct equivalence between AQC as defined here and the circuit-based quantum computing [39]. Furthermore, an adiabatic Grover's algorithm has been presented and proven to have the same quadratic quantum advantage as the circuit-based version [40]. However, this algorithm still has a dependence on quantum oracles.

Now, we introduce an important subclass of AQC called *stoquastic* AQC (stoqAQC) [41]. StoqAQC focuses on a particular class of Hamiltonians called stoquastic Hamiltonians, which are characterised by having non-positive off-diagonal elements in the computational basis. In particular, this thesis will focus on transverse stoquastic Hamiltonians, which have the form

$$\hat{H}_{\text{trans\_stoq}} = - \sum_i \hat{X}_i + \hat{H}_Z, \quad (2.40)$$

where  $\hat{H}_Z$  is diagonal in the computational basis and  $\hat{X}_i$  corresponds to the  $\hat{X}$  gate on the  $i^{\text{th}}$  qubit.

This raises the question as to whether these types of stoquastic Hamiltonians could be efficiently simulated on a classical computer. While an algorithm to do so has not been found, there is strong evidence to believe they should be. For stoqAQC to have the same computational power as a universal quantum computer, the polynomial hierarchy would have to collapse, which would bring about a revolution in computational complexity theory, and is considered extremely unlikely [41].

However, if we relax the conditions on adiabatic evolution, it is known that stoqAQC is in fact universal [25], which leads to the introduction of quantum annealing.

## 2.7 Quantum Annealing and Quadratic Unconstrained Binary Optimisation Problems

Quantum annealing (QA) is an approximate algorithm that can run on any adiabatic quantum computer, with the following conditions:

1. the target Hamiltonian is a two-local Ising Hamiltonian of the form  $\hat{H}_T = \sum_i J_i \hat{Z}_i + \sum_{i,j} J_{ij} \hat{Z}_i \hat{Z}_j$ , with initial Hamiltonian  $\hat{H}_i = \sum_i \hat{X}_i$ .
2. the computation can violate the adiabatic condition and can partially proceed in excited states.

Importantly, it is an approximate algorithm, implying that it's not measured by its ability to find the true optimal solution, but to provide a better solution than other existing algorithms in the same time. Approximate algorithms for combinatorial NP problems are ubiquitous, and include problems like the Travelling Salesman Problem, Scheduling, Protein Folding, among many others.

The basic form of QA is

$$\hat{H}(t) = (1 - s(t)) \sum_i \hat{X}_i + s(t) \left( \sum_i J_i \hat{Z}_i + \sum_{i,j} J_{ij} \hat{Z}_i \hat{Z}_j \right). \quad (2.41)$$

There are two directions being heavily pursued to improve its performance.

Firstly, careful variations of the scheduling function  $s(t)$  have been shown to improve performance. By allowing  $s(t)$  to take different functional forms, we can violate the adiabatic condition and proceed with probability in the excited states. This technique has also been pursued to great success in fields like simulated thermal annealing, as well as in many other optimisation problems [42]. This has been shown empirically to radically improve the performance of QA [43]. The two most promising annealing schedules are

- the power law schedule,  $s(t) = At^a$ . [44, 45]
- the exponential schedule,  $s(t) = Ae^{at}$ ,  $a < 0$ . [46, 45]

Secondly, the introduction of intermediate Hamiltonians to change the energy landscape, which changes the Hamiltonian to

$$\hat{H}(t) = \underbrace{(1 - s(t)) \sum_i \hat{X}_i}_{\text{initial}} + \underbrace{g_i(t) \sum_i \hat{H}_i}_{\text{intermediate}} + \underbrace{s(t) \left( \sum_i J_i \hat{Z}_i + \sum_{i,j} J_{ij} \hat{Z}_i \hat{Z}_j \right)}_{\text{target}}, \quad (2.42)$$

where  $g_i(t)$  has  $g_i(0) = g_i(1) = 0 \forall i$ , and  $\hat{H}_i$  are usually chosen from a set of easily implemented Hamiltonians. This was studied extensively by Zeng (2016) [47], where they showed empirically the extreme improvements possible, and derived a technique that in some limit was provably optimal. However, in their scheme the optimisation process was itself exponential, meaning that there need to be heuristics introduced to make this a feasible technique for real-world use.

The main focus of quantum annealing is to solve quadratic unconstrained binary optimisation (QUBO) Problems [48]. This is the problem of finding the bitstring  $x_0 \dots x_n$  which minimises a quadratic polynomial

$$f_Q(x_0 \dots x_n) = \sum_{ij} q_{ij} x_i x_j \quad | \quad x_i \in \{0, 1\}. \quad (2.43)$$

This is a combinatorial optimisation problem part of the complexity class NP-Complete. I prove this in Section 5.1 by showing an isomorphism between a commonly known NP-Complete problem and QUBO.

This looks similar to the Ising Hamiltonian  $\hat{H}_T$ , however the eigenvalues of  $\hat{Z}$  are  $1/2, -1/2$  instead of the binary  $0, 1$ . However, we can simply transform each  $x_i$  term as

$$x_i \rightarrow \frac{1}{2}(1 - \hat{Z}_i) \quad (2.44)$$

to generate the QUBO form from an Ising Hamiltonian.

The only available device that claims to perform QA is owned by D-Wave. However, there is vigorous debate over just how ‘quantum’ D-Wave really is [24, 49] Fundamentally, this derives from the decoherence time ( $\approx 5\text{ns}$ ) of the superconducting qubits that D-Wave uses being far smaller than the total annealing time ( $\approx 20\mu\text{s}$ ). Given this, the computation can only proceed taking advantage of any quantum effects for a tiny fraction of the total annealing time. However, because their device operates at milliKelvin temperature, relaxation will play a major role as the qubits equilibrate. This leads many to suggest that D-Wave is actually more likely to be a classical annealer. If this is the case, devices which perform simulated annealing in classical silicon, or which implement better physical coupling and thermal annealing, are more likely to provide value.

Unfortunately, this means that the evidence for, or against, an experimental speedup is extremely difficult to interpret. There are theoretical results that showed quantum annealing advantage on a variety of problems [50, 51], however the most important theoretical result is probably from Crosson and Harrow (2016) [52], which showed that simulated quantum annealing (SQA) could be exponentially faster than classical simulated annealing. This result showed that a Markov Chain Monte Carlo method which (in the limit of samples going to infinite) performed the same operation

as quantum annealing, could outperform simulated annealing. Importantly, however, this is still an implementable classical algorithm. Being a classically implemented classical algorithm means that there will likely be no exponential speedup on a quantum device. However, since a quantum annealer could run the algorithm natively, it would be expected to run it many, many times faster.

Experimentally, there is strong evidence for both sides of the debate. Cho [21] (2014) argued that quantum annealing could not generate a speedup, whilst Katz-graber [23] (2015) suggests that there was evidence that speedups existed. Mandra [22] (2018) showed that they could obtain a constant speedup on a selected set of problems, however showed identical exponential scaling behaviour. The current belief in the field, primarily based on the theoretical evidence, is that quantum annealing is likely to achieve speedups in one way. This is by reducing the prefactor in front of the exponential scaling, which Mandra found to be 100 times better in cases specially constructed to be difficult for the best classical algorithms [22]. An important result in the field was presented by Denchev et al. (2016) [53], where they found a 100 million ( $10^8$ ) asymptotic speedup over simulated annealing showing that the quantum tunnelling effect is important. However, it is important to recognise that this was a comparison against one specific algorithm in simulated annealing, whilst compared to the best-known classical algorithm this speedup was a constant-factor modest speedup. However, all of this work was also done using D-Wave's controversial device, highlighting the difficulty in making any conclusive statements about quantum annealing due to the inherent uncertainty in whether the device is even performing the task.

Overall, quantum annealing is still a promising field, with strong theoretical foundations for being able to improve on a large class of important algorithms. However, due to the lack of trust in the existing quantum annealing devices, making conclusive statements about experimental results is all but impossible. This highlights the need of designing and building a quantum annealer that does not suffer from thermal problems, and with decoherence times on the same order of magnitude as the annealing time.

## 2.8 The Nitrogen-Vacancy Centre in Diamond

The Nitrogen-Vacancy Centre in Diamond (NV Centre) is a point defect in diamond made up of a substitutional Nitrogen and adjacent Carbon Vacancy. Whilst hundred of interesting point defects have been discovered in diamond [54, 55], the NV centre became of particular interest towards the end of the last century [56, 57]. In 1997, the isolation of single NV centres at room temperature through scanning confocal optical microscopy [58] led to attempts to use the NV Centre to perform quantum computation. In 2001, a Carbon-13 nucleus nearby the NV centre was proposed to perform quantum

computation. Then soon after, it was discovered that there was coherent coupling between Carbon-13 nuclei and the Nitrogen nuclei in the NV, with multiple qubit quantum computation being performed in 2014 [59, 60]. There are currently large scale-attempts at developing these results to enable industrial production of many NV Centre qubit quantum computers.

The NV Centre has broader applications than quantum computing, with laboratory demonstrations of electrometry and thermometry. Most notably however are the applications in magnetometry and quantum nano-sensing and microscopy. In magnetometry Lockheed Martin have commercialised the NV centre for geophysical surveying, military, and navigation applications [61, 62]. In microscopy, the NV Centre can be used for atomic-scale detection of local electric and magnetic fields [63, 64, 65, 66, 67]. However, the focus of this thesis is the NV Centre’s possibility to be used as a device capable of adiabatic quantum computing.

The aim of this section is to help the reader develop a mental model of using the NV Centre as a foundation for a quantum computer, and to provide mathematical foundations for the derivations in Chapter 3. Importantly, we consider the NV Centre where the Nitrogen atom is Nitrogen-15, as it enables an extra spin-half quantum register and can be trivially engineered to be so [68].

### 2.8.1 The Structure and Quantum Properties of the NV Diamond Quantum Processor

There are two charge states  $NV^0$  and  $NV^-$ , where  $NV^-$  has the electronic structure useful for quantum computation. With appropriate doping of the diamond, the  $NV^-$  state dominates, and adding photoionisation mechanisms allows for extremely high fidelity initialisation into this state. When I talk about the NV Centre from now on, I mean the  $NV^-$  charge state. The  $NV^-$  electronic structure is a ground state triplet ( ${}^3A_2$ ), and an excited triplet  ${}^3E$ , with two intermediate singlets ( ${}^1E, {}^1A$ ). By exciting optically the  ${}^3A_2 \rightarrow {}^3E$  transition, the electron spin can be initialised with high fidelity. Similarly, the intensity of fluorescence under exciting this transition depends on the spin-state of the electron, allowing for optical readout of the electronic spin state [69]. After high fidelity optical initialisation, the NV Centre has the longest electron spin coherence time, ( $\approx 2.4\text{ms}$ ), of any solid state spin at room temperature [70].

The electronic structure is coupled to a nuclear spin structure, where the nuclear spins are what will be used as qubits. For many of the NV quantum computer designs, there is also the replacement of a Carbon-12 atom with a Carbon-13 atom to produce a spin-1/2 register. The substitutional Nitrogen and Carbon-13 then couple via the hyperfine interaction to the electron spin. When the hyperfine couplings are not equal, this allows for driving resonantly specific transitions that allow for single qubit opera-

tions. By entangling the electron and nuclear spin we can read-out of the nuclear spin state via the electron fluorescence.

The vacancy of the NV is electronic in nature, and has Spin-1. The operators that act on this electronic component are denoted by  $\hat{S}_i$ . The nucleus of a Nitrogen-15 and Carbon-13 is Spin-1/2, and the operators that act on the nuclear component are denoted by  $\hat{I}_i$ . An effective Hamiltonian for the NV Centre from [69] is

$$\hat{H}_{\text{stationary}} = \underbrace{D_{zfs}(\hat{S}_Z^2 - \frac{2}{3}) + \gamma_e B_0 \hat{S}_Z}_{\text{electronic component}} + \sum_i \underbrace{\mathbf{S} \cdot \vec{A} \cdot \mathbf{I} - \gamma_I B_0 \hat{I}_Z}_{\text{nuclear components}}, \quad (2.45)$$

where  $B_0$  is the strength of an external magnetic field that splits the electron spin states, and  $\vec{A}$  is the hyperfine tensor.

Along with the other electronic level states, and with expanding this Hamiltonian describing the ground state triplet, gives rise to the energy structure diagram in Fig. (2.5).

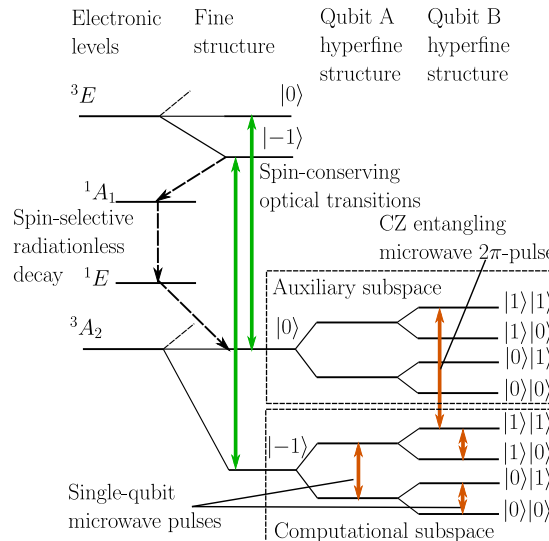


Figure 2.5: The energy structure of an NV Centre with two hyperfine coupled spin-half nuclear spins. The green transitions allow for excitation that allow for electron spin initialisation and readout. The orange transitions represent different single and two-qubit operations on our qubits. By driving transitions from  $|-1\rangle$  to  $|0\rangle$  conditioned on the state of the nuclear spin, we can imprint the nuclear spin state onto the electron state, which can then be read out.

By combining the need for optical initialisation and readout mechanisms, microwave control for qubit operations, a D-C magnetic field to split the energy levels and doping for charge-state initialisation, we generate the current design of a diamond quantum processor shown in Fig. (2.6).

Currently, many NV Centres are characterised for how many neighbouring Carbon-

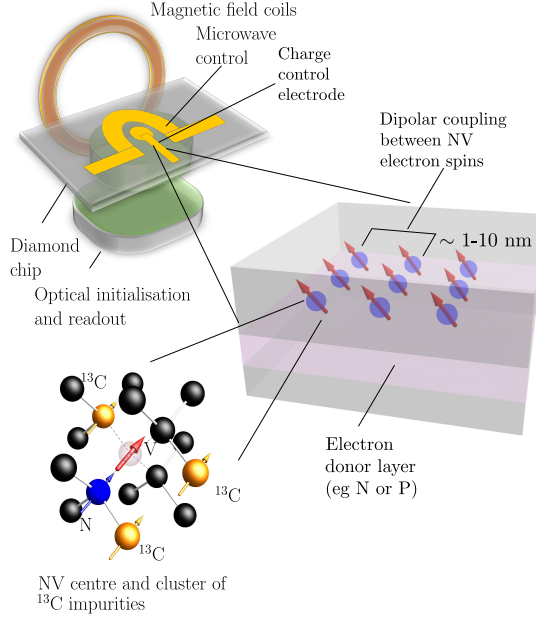


Figure 2.6: The currently proposed design of a diamond quantum processor will be explored for its potential to perform quantum annealing in Chapter 3. The magnetic field coils are on each side giving approximately linear gradients over the NVs, and a strong external magnetic field gives the electron spin splittings.

13 atoms are adjacent, and specific Centres with many neighbouring Carbons are selected. However, the focus of the designs presented in this thesis is their ability to scale. As it is currently not possible to engineer the Carbon-13 atoms into the lattice, I proceed mathematically as if there were no Carbon-13 atoms nearby. Due to the trigonal symmetry of the NV Centre,  $\vec{A}$  is

$$\vec{A} = \begin{pmatrix} A_{\perp} & 0 & 0 \\ 0 & A_{\perp} & 0 \\ 0 & 0 & A_{\parallel} \end{pmatrix} \quad (2.46)$$

We can now perform first-order perturbation theory to understand the magnitude of the effects of perpendicular components of the hyperfine tensor [71]. This will allow us to make the secular approximation, and neglect these terms entirely. Consider one of the terms in the perturbation to first-order of the  $|0\rangle$  and  $| -1\rangle$  transition given by (Eq. 2.47). The energy splitting of these two levels is approximately  $\Delta E = \gamma_e B_0$ .

$$| -1 \rangle^{(1)} = \frac{\langle 0 | \hat{H} | -1 \rangle}{\Delta E} | 0 \rangle \quad (2.47)$$

$$= \frac{A_{\perp}}{\gamma_e B_0} | 0 \rangle. \quad (2.48)$$

Substituting with  $B_0 = 1T$ ,  $A_{\perp} \approx 1\text{MHz}$ ,  $\gamma_e \approx 28\text{GHz}$  gives the size of the perturbation (Eq. 2.49) as

$$\frac{1\text{MHz}}{28000\text{MHz}} = 3.57 \times 10^{-5}. \quad (2.49)$$

Therefore, these perturbations are insignificant and safe to ignore. This leaves us with a simplified Hamiltonian (Eq. 2.50)

$$\hat{H}_{\text{secular}} = D \left( \hat{S}_Z^2 - \frac{2}{3} \right) + \gamma_e B_0 \hat{S}_z - \gamma_I B_0 \hat{I}_z + A_{\parallel} \hat{S}_z \hat{I}_z \quad (2.50)$$

This gives rise to an energy structure as shown in Fig. 2.7.

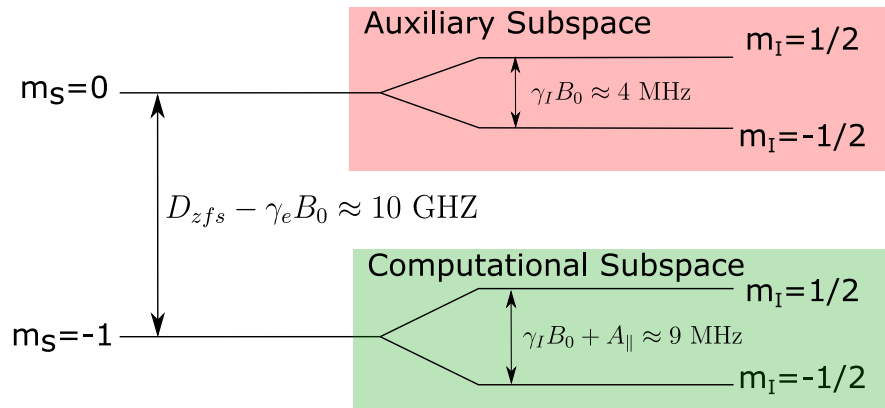


Figure 2.7: The energy structure of a Spin-1/2 nuclear spin with a Spin-1 electronic system behaving under Eq. (2.50).

The current proposal to control the quantum dynamics of the NV Centre involves putting a radio-frequency (RF) transmitter that resonantly drives transitions. This adds a time-dependent component to the Hamiltonian

$$\hat{H}_{\text{control}} = \hat{H}_{\text{secular}} + B_e(t) \hat{S}_X + B_I(t) \hat{I}_X. \quad (2.51)$$

This Hamiltonian is the starting point for the derivations followed in Chapter 3.

### 2.8.2 Creating NV Centres (Semi-)Deterministically

There are broadly three existing and a single proposed method for creating NV rich diamond. The first, pioneered in 1999 [72], used a nitrogen-rich (type 1b) diamond, and through irradiation creates vacancies. Then, the diamond, now with many Nitrogen substitutions and Vacancies throughout, although not adjacent, is heated to around 600 °C where the vacancies move under a random walk, until they find a Nitrogen and create a stable (at 600 °C, up to 2000 °C) NV Centre. This puts an upper bound on the density of NV centres as the amount of Nitrogen in the initial diamond sample. In 2011, an NV density of 1% or 10,000 ppm (2.75 NVs per nanometre cubed) was claimed to be achieved [73], however this result could not be validated in 2013, where a more modest 400 ppm was achieved [74]. Importantly, the creation of NV Centres through this method involves an inherent randomness in the placement of the Nitrogens. While high densities are achievable, they are randomly distributed. The spatial resolution for creation of NVs is on the order of 200 nm, which is two orders of magnitude greater than what is needed for building an ideal diamond quantum computer [72].

Second is by Nitrogen ion implantation, where a beam of 2 MeV N<sup>+</sup> ions is accelerated onto a type IIa (extremely pure) diamond [75]. This method allows for the creation of many, localised NV centres at specific locations in the diamond. However, the beam diameter was only 0.3 μm, focused using a 15 T solenoid lens. Using nanopores, then this technique has achieved a spatial resolution on the order of 20nm [76, 77]. However, the magnetic interactions which allow for coupling between adjacent NV Centres in our design can maximally extend over approximately 10 nanometres before becoming too weak. Furthermore, there is a large variation in how deeply the Nitrogen-Vacancies centres are created due to ion straggling and channelling effects. Therefore this technique is not yet able to provide the spatial resolution required for the precise design.

Lastly, is through delta-doping, allowing the creation of surface-level aligned Nitrogen-Vacancy Centres. Using plasma-enhanced chemical vapour deposition (PE-CVD), high purity <sup>15</sup>N<sub>2</sub> gas is deposited onto the surface of pure diamond, followed by irradiation and annealing [78]. This gives extremely low variance (sub-nanometre) in the depth that the NV Centre is created. However, controlling the location of where the Nitrogen implants can still only be done with a nanopore mask. The best delta doping to date achieved a density of 0.18nm<sup>-3</sup> [79], which is the minimum value explored in Chapter 4.

The proposed technique, but which has not been realised, is through atom-scale fabrication processes, such as scanning tunnelling microscopy (STM). In 1989, Eigler and Chweizer at IBM used an STM to pick up 35 Xenon atoms and place them to atom-level precision on the surface of a cold nickel substrate [80]. This demonstration

proved that it was possible to manufacture and engineer at the atomic scale. The proposal is to use atomically precise hydrogen depassivation lithography (remove the Hydrogen, create a dangling bond), and then dope the surface using gaseous nitrogen which will preferentially attach to the dangling bonds, followed by diamond overgrowth, irradiation and annealing. In my opinion, this is the most likely method for producing scalable gate-based diamond quantum computers, as it allows for the precision required to create a perfect array of NV Centres. However, there is much engineering research required in realising this approach. A design using the possibilities afforded by this technique is proposed in Chapter (3).

This setting of currently being able to generate high-density ensembles of NVs, but not yet being able to position them precisely motivates Chapter 4, which proposes a design that takes advantage of the high-density random ensembles techniques.

## 2.9 Instance Space Analysis

With the growth of the importance of approximate algorithms that leverage heuristics to find ‘good enough’ solutions to computationally intractable problems, a focus of modern computer science research is evaluating and comparing these algorithms. Prior to the development of Instance Space Analysis (ISA) [81], the standard practise was to obtain a collection of *instances* from a *problem space*, and execute each algorithm on each of these problems, and to select the algorithm which had the highest mean performance. As a concrete example of an instance and problem space, the *problem space* considered in Chapter 5 is 10-node mathematical graphs, and different instances of these graphs have different edges. Instances could either be randomly generated, or could be taken from real-world data.

However, this standard practice has three major shortcomings. First, the mean performance ignores that certain heuristic algorithms have specific strengths and weaknesses. For example, an algorithm could have significantly worse *mean* performance, however still be the best performing algorithm on a collection of instances. Second, there is no consideration as to whether the data collected or generated forms an unbiased representation of all of the possible instances. Therefore, when research into new algorithms is performed, there is a bias towards optimising against a benchmark, which may not be representative of the problems it will face in reality. Lastly, it allows for researchers to cherry-pick a collection of instances for which their algorithm performed optimally, and highlight these.

ISA attempts to solve these problems by introducing a standard workflow for analysing new approximate algorithms and their application to problem spaces. Importantly, ISA allows for efficiently selecting the algorithm most likely to be optimal

for a particular new, unseen instance based off of statistical techniques. Furthermore, ISA attempts to put visualisation at the forefront so that algorithm performance can be understood more readily by the researcher.

ISA has the following steps that will be described in this section:

1. generate a *feature set* that allows conversion of an instance space to a feature space.
2. execute a selection of approximate algorithms for each instance.
3. perform a dimensionality reduction technique to compress into 2D for visualisation.
4. statistically determine the optimal algorithms for a given region of feature space.

A *feature* is an efficiently computable numerical value that describes some aspect of a particular instance. For example, a feature of a graph is the density, the number of edges divided by the total number of possible edges. Not all features will necessarily be predictive, however we use statistical techniques to isolate the useful features from the non-useful ones for a particular task. We call the collection of features the *feature vector*, the space over which the features are mathematically sensible (e.g. positive number of nodes), the feature space. For a feature space to be useful it should preserve the property that instances that are ‘similar’, should have feature vectors that are close together (in Euclidean distance). We create a feature matrix where each column is the feature vector of a particular instance.

Once we have a collection of instances each with an associated feature vector, we run a series of approximate algorithms over each instance, with each giving the best value found.

Then, we perform a Principal Component Analysis (PCA) on the feature matrix [82], which allows for compression of the information in the feature matrix in a way that minimises the information loss to an arbitrary target dimension. Principal component analysis gives an output transformation matrix that can be applied to a feature vector that reduces it. For ISA, compress the feature space to 2D, with the dimension names  $Z_1$  and  $Z_2$ .

Then, we can use supervised learning classification techniques using the known performance of each algorithm on a given instance to learn the regions within which each algorithm performs optimally. If we use Support Vector Machines (SVM) [83], which allow for a nonlinear partitioning of a space into classification boundaries, we can produce a plot similar to Fig. (2.8). To use this plot, an unseen instance has the feature

extraction routine executed to generate its feature vector, which is compressed according to the principal component analysis. Then, the SVM predicts which algorithm is the best choice for the instance.

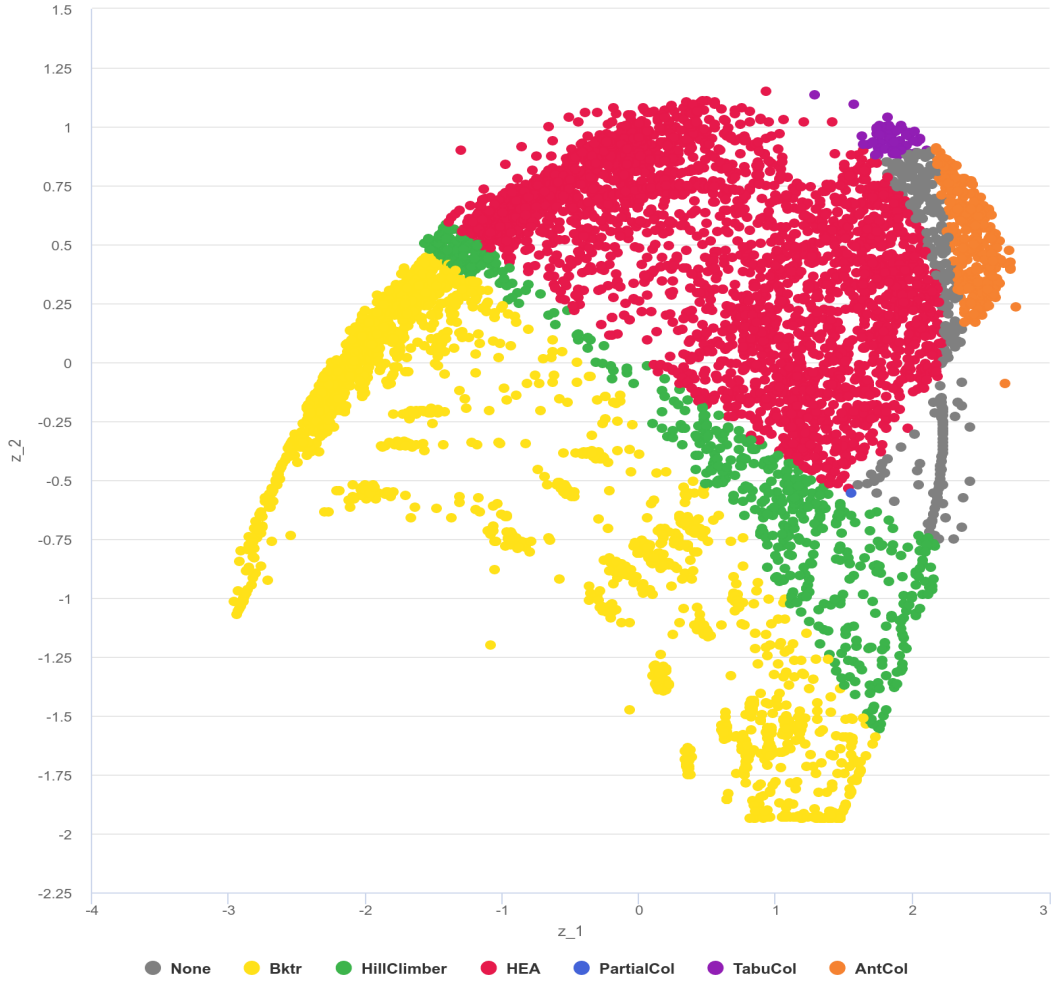


Figure 2.8: The SVM prediction partitions the compressed feature space into regions where a particular algorithm performs optimally. Using the mean approach, we might conclude that algorithms HEA or Bktr are optimal due to them having the largest optimal footprint, however this would provide sub-optimal results since there are algorithms which perform better in small, localised regions of instance space. Since the features are efficiently computable, this allows a pipeline where these features are computed, then the SVM predicts the optimal algorithm(s) that should be executed. Figure taken from [81]

In this thesis, ISA is predominantly used not as a way of partitioning the instance space, but to compare how different approaches ‘view’ the difficulty of problems from a qualitative perspective. Intuitively, if two algorithms rely on the same underlying heuristics or theory, then I expect them to have the same view of instance difficulty

when represented in this instance space framework.

---

# Design for an Ideal Diamond Quantum Annealer Using an Array of N-V Centres

---

To design a diamond quantum annealer we need the following pieces

1. a scalable design of non-degenerate physical qubits that can be coupled together.
2. a method to implement the quantum annealing Hamiltonians  $\hat{H}_i = \sum_j \hat{I}_{X,j}$  and  $\hat{H}_T = \sum_i J_i \hat{I}_{Z,i} + \sum_{ij} \hat{I}_{Z,i} \hat{I}_{Z,j}$ .
3. a qubit connectivity graph that is dense enough to be able to realise a large class of annealing problems.

I will treat these separately in the following three sections.

## 3.1 Array of Diamond N-V Centres

In this section I design an adiabatic quantum computer that could only be achieved with atom-precise manufacturing techniques. The design that I will be building towards is shown in Figure (3.1).

Our radiofrequency transmitter is applied over the whole diamond simultaneously. In fact, it would be impossible to isolate certain qubits by focusing the RF field, since the wavelength of the RF field is microwave (10s of millimetres) to radiowaves (10s of metres), and the N-V Centre separation is on the nanometre order. Therefore, to be able to address each N-V Centre separately the transitions that I will resonantly drive all need to be non-degenerate.

Recalling that the stationary Hamiltonian for an N-V Centre is

$$\hat{H} = D \left( \hat{S}_Z^2 - \frac{2}{3} \right) + \gamma_e B_0(x, y, z) \hat{S}_z - \gamma_I B_0(x, y, z) z \hat{I}_z + A_{\parallel} \hat{S}_z \hat{I}_z, \quad (3.1)$$

we notice that the only controllable variable is the magnetic field  $B_0(x, y, z)$ .

To ensure each N-V Centre has non-degenerate transitions, I apply magnetic field gradients of  $\delta B_x$  and  $\delta B_y$ . Combined with the DC magnetic field, this produces a total

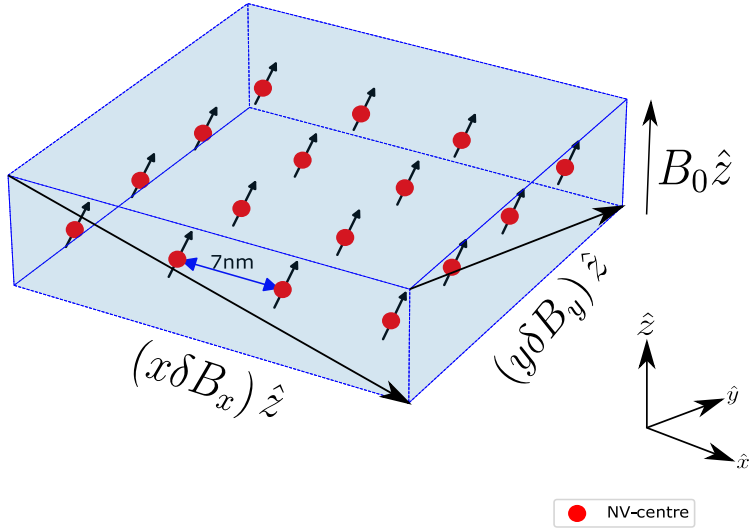


Figure 3.1: Using a regular array allows for qubits with extremely high quality, and a simple model for qubit connectivity.

magnetic field of

$$\mathbf{B}_{\text{external}} = (B_0 + x \times \delta B_x + y \times \delta B_y) \hat{z}. \quad (3.2)$$

To realise this magnetic field, we have two orthogonal pieces of wire running atop the Diamond sample that produce an approximately linear field over part of the  $x$ - $y$  plane, similar to the coil design of magnetic resonance imaging[84]. This equation (Eq. 3.2) for the magnetic field defines a plane with a linear drop-off in the  $x$ - $y$  directions, and a  $z$  offset. Since there is a plane, there will be linear manifolds which have equal values of  $B$ . Importantly, the reason for the introduction of these magnetic field gradients was to ensure that no two N-V Centres have a degenerate transition gap, which will be violated along these manifolds. By choosing  $\delta B_x$  and  $\delta B_y$  carefully, we can guarantee mathematically that they will not pass through the exact point. Ideally, I maximise the distance between any given qubit and any other qubits line of equal value. Fig. (3.2) shows how careful choice of magnetic field gradients and spacing partially avoids this problem. However, it is immediately clear that as we scale to larger number of qubits, the density of parallel lines in Fig. (3.2) will increase, and as such this problem will become increasingly challenging.

There are interesting engineering possibilities by having degenerate qubits spread out, which will be briefly discussed in Section 3.2.2, however solving these issues is not of near-term importance as building large arrays of physical qubits itself is not yet possible.

To allow for the approximations later to be valid, our controlling fields need to be

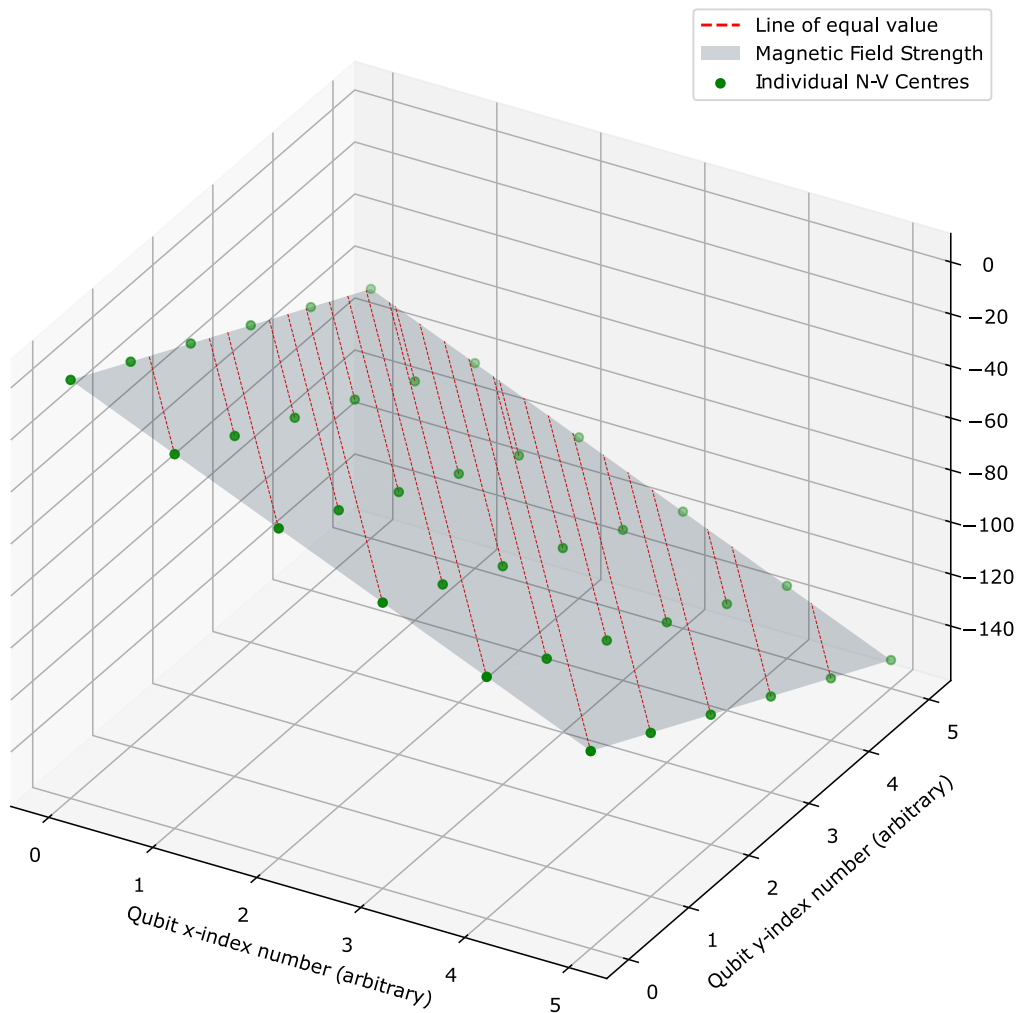


Figure 3.2: The linearity of the magnetic field gradient implies that lines of equal value are straight and parallel, and hence will become dense as the number of the qubits increases, which will eventually make certain physical qubits approximately degenerate.

in the strong driving limit, which means we need a minimum differentiability of about 0.1 MHz. The interaction between two N-V Centres is mediated by the magnetic dipole interactions due to the electronic configuration. Whilst this is fully derived in Section 3.2.2, this is approximately

$$\frac{g_e^2 \mu_B^2 \mu_0}{4\pi} \frac{1}{|r'|^3}, \quad (3.3)$$

where  $|r'|$  is the separation between adjacent qubits. Converting this to MHz and solving for  $r'^3$  gives

$$|r'|^3 = \frac{g_e^2 \mu_B^2 \mu_0}{4\pi h} / 10^6 \quad (3.4)$$

$$\implies |r'| = 8.29 \text{ nm}. \quad (3.5)$$

With all of these pieces of the puzzle, this produces the design (Fig. 3.1) introduced at the beginning of this section.

## 3.2 Derivation of the Quantum Annealing Hamiltonian from the N-V Hamiltonian

In this section, I present a novel derivation which shows how the Hamiltonian of the N-V Centre can be converted into the quantum annealing Hamiltonian. For simplicity, this is broken into two parts. Firstly, I present each of the required transformations for a single N-V Centre for simplicity. Then, I add an additional qubit which then gets converted finally into the quantum annealing Hamiltonian.

### 3.2.1 Example of the Transformations on a Single Qubit

As stated in the background, the ground state of the NV-centre is a  ${}^3A_2$  triplet, which has effective Hamiltonian

$$\hat{H} = D \left( \hat{S}_Z^2 - \frac{2}{3} \right) + \gamma_e B_0 \hat{S}_z - \gamma_I B_0 \hat{I}_z + A_{\parallel} \hat{S}_z \hat{I}_z, \quad (3.6)$$

where  $D$  is the zero-field splitting, and  $\vec{A}$  is the hyperfine coupling tensor, and  $\vec{S}, \vec{I}$  are the spin operator vectors (e.g.  $(\hat{S}_x, \hat{S}_y, \hat{S}_z)$ ).

In operation,  $B_0 \gg D$  which will make the energy splittings between the  $z$  projections large. Furthermore, due to the gyromagnetic ratio of the electron being four orders of magnitude larger than the nuclear projections, we can model these quantum mechanical systems as independent of one another. Therefore, a very good approximate eigenstate is the  $|m_s, m_I\rangle$  combined z-projections.

Since all of our operators are acting in  $Z$ , it can be immediately seen that our eigenbasis is the tensor product space of the spin-z eigenbasis for the electron spin-1 system and the nuclear spin-1/2 system. It will turn out that we will not need to use the  $|1\rangle$  projection of the electron spin, and that upon making the rotating wave approximation we can neglect this subspace entirely. So that all of the rotating wave approximations are done together, this will be performed later. However, this is the reason that we will only calculate the energies of certain levels.

To calculate numerically the energy levels we will define the parameters as in Tab. 3.1

Parameter	Value
$D$	$2.87 \times 10^3$ MHz
$B_0$	0.62 T
$A_{\parallel}$	5 MHz
$\gamma_e$	$2.8 \times 10^4$ MHz
$\gamma_I$	4.3 MHz

Table 3.1: The values of the parameters in the Hamiltonian

Calculating the full energy structure of the lower two electron spin projections produces Tab. 3.2. We can simply substitute our spin-Z projection for the electronic structure and nuclear spin and compute the energy splitting. Recall we only care about the lower two spin projections of the electron.

$m_s$	$m_I$	Energy Expression	Energy (MHz)
0	$\frac{1}{2}$	$-2/3 D - 1/2 \gamma_I B_0$	-1914.67
0	$-\frac{1}{2}$	$-2/3 D + 1/2 \gamma_I B_0$	-1912
-1	$\frac{1}{2}$	$D/3 - \gamma_e B_0 - 1/2 \gamma_I B_0 - 1/2 A_{\parallel}$	-16407.2
-1	$-\frac{1}{2}$	$D/3 - \gamma_e B_0 + 1/2 \gamma_I B_0 + 1/2 A_{\parallel}$	-16399.5

Table 3.2: The values of the parameters in the Hamiltonian

Now that we have these energies, we know what frequencies to tune our control fields to. By the selection rules, we can drive transitions that preserve either nuclear spin or electron spin. This implies that in total there are four transitions that we will be driving, pictured below (Fig. 3.3).

This then allows us to write our control Hamiltonian tuned to resonant driving of

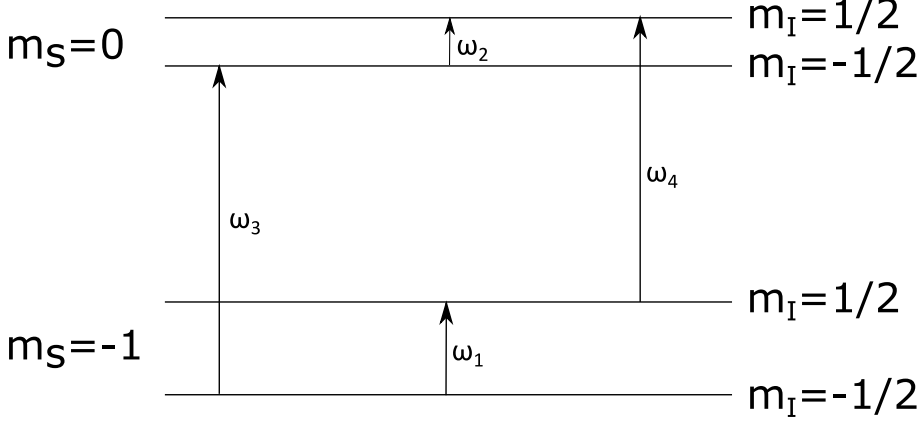


Figure 3.3: The possible transitions and their frequencies of a single NV centre.

these transitions as

$$\begin{aligned} \hat{H}_t = & \left( \hat{S}_x + \hat{I}_x \right) (B_1(t) \cos(\omega_1 t + \phi_1) + B_2(t) \cos(\omega_2 t + \phi_2) \\ & + B_3(t) \cos(\omega_3 t + \phi_3) + B_4(t) \cos(\omega_4 t + \phi_4)), \end{aligned} \quad (3.7)$$

where  $B_i(t)$  is the amplitude of the incident electromagnetic wave at time  $t$ .

Since our control Hamiltonian has explicit time dependence, it is quite difficult to work with. As such, we transform into the interaction picture and make the rotating wave approximation. Transformation into the interaction picture follows

$$\hat{H}_{\text{int}} = \tau \hat{H}_t \tau^\dagger \text{ where} \quad (3.8)$$

$$\tau = e^{i\hat{H}t} \quad (3.9)$$

Because we know that our time-independent part of the Hamiltonian was diagonal in the  $z$  basis, we can immediately write down that

$$\tau = \sum_{i,j} e^{iE_it} |i\rangle \langle j|, \quad (3.10)$$

where  $i \in \{-1, 0, 1\}$  and  $j \in \{\uparrow, \downarrow\}$ . Therefore, we can write down explicitly what the  $(i, j)^{\text{th}}$  component of the resulting Hamiltonian will be as

$$\hat{H}_{\text{int},ij} = e^{i(E_i - E_j)t} (\hat{S}_{x,ij} + \hat{I}_{x,ij}) \left( \sum_k B_k(t) \cos(\omega_k t + \phi_k) \right) \quad (3.11)$$

Now, we can recall that our  $\omega$  values are actually particular instances of  $E_i - E_j$ . Let's consider an on-resonance term. If we are on resonance, then our equation will

have be of the form with  $\omega_1 \neq \omega_2$ .

$$e^{i\omega_1 t} (B_1 \cos(\omega_1 t + \phi_1) + B_2 \cos(\omega_2 t + \phi_2)). \quad (3.12)$$

Expanding our phasor and applying our double angle formulae and reducing

$$(\cos(\omega_1 t) + i \sin(\omega_1 t))(B_1 \cos(\omega_1 t + \phi_1) + B_2 \cos(\omega_2 t + \phi_2)) \quad (3.13)$$

$$\begin{aligned} &= \frac{1}{2} \left( B_1 (\cos \phi_1 + \cos(2\omega_1 t \phi_1)) - i B_1 (\sin \phi_1 - \sin(2\omega_1 t + \phi_1)) \right. \\ &\quad + B_2 (\cos(\omega_2 t - \omega_1 t + \phi_2) + \cos(\omega_2 t + \omega_1 t + \phi_2)) \\ &\quad \left. - i B_2 (\sin(\omega_2 t - \omega_1 t + \phi_2) - \sin(\omega_1 t + \omega_2 t + \phi_2)) \right) \end{aligned} \quad (3.14)$$

The rotating wave approximation states that (when solving for the dynamics) the effect of off non-resonant terms is negligible with respect to the on-resonant terms and oscillate rapidly around the on-resonant transition. By neglecting all of the off-resonant terms, we derive

$$e^{i\omega_1 t} (B_1 \cos(\omega_1 t + \phi_1) + B_2 \cos(\omega_2 t + \phi_2)) \approx \frac{B_1(t)}{2} (\cos \phi_1 - i \sin \phi_1). \quad (3.15)$$

We can then apply this to each term in the control Hamiltonian, since now all off-resonance terms immediately go to zero.

Since we are not driving any transitions into the  $|1\rangle$  projection, all of those elements of the  $\hat{S}_x \otimes \hat{I}_x$  will be multiplied by zero according to the rotating wave approximation. This directly means that we are living in the  $|-\rangle, |0\rangle$  subspace of the electronic spin projection, and then we can describe this system perfectly using spin-1/2 matrices.

Then, labelling the eigenstates by  $|m_s\rangle |m_I\rangle$  we can express the rotating wave approximation as selecting out specific terms as in (Eq. 3.16)

$$\begin{aligned} e^{i\omega_1 t} B_1 \cos(\omega_1 t + \phi_1) &\rightarrow \frac{B_1}{2} ((\cos \phi_1 - i \sin \phi_1) |\downarrow\uparrow\rangle \langle \downarrow\downarrow| + (\cos \phi_1 + i \sin \phi_1) |\downarrow\downarrow\rangle \langle \downarrow\uparrow|) \\ e^{i\omega_2 t} B_2 \cos(\omega_2 t + \phi_2) &\rightarrow \frac{B_2}{2} ((\cos \phi_2 - i \sin \phi_2) |\uparrow\uparrow\rangle \langle \uparrow\downarrow| + (\cos \phi_2 + i \sin \phi_2) |\uparrow\downarrow\rangle \langle \uparrow\uparrow|) \\ e^{i\omega_3 t} B_3 \cos(\omega_3 t + \phi_3) &\rightarrow \frac{B_3}{2} ((\cos \phi_3 - i \sin \phi_3) |\uparrow\downarrow\rangle \langle \downarrow\downarrow| + (\cos \phi_3 + i \sin \phi_3) |\uparrow\downarrow\rangle \langle \uparrow\downarrow|) \\ e^{i\omega_4 t} B_4 \cos(\omega_4 t + \phi_4) &\rightarrow \frac{B_4}{2} ((\cos \phi_4 - i \sin \phi_4) |\uparrow\uparrow\rangle \langle \downarrow\uparrow| + (\cos \phi_4 + i \sin \phi_4) |\downarrow\uparrow\rangle \langle \uparrow\uparrow|) \end{aligned} \quad (3.16)$$

Now, we notice that

$$((\cos \phi_1 - i \sin \phi_1) |\downarrow\uparrow\rangle \langle \downarrow\downarrow| + (\cos \phi_1 + i \sin \phi_1) |\downarrow\downarrow\rangle \langle \downarrow\uparrow|) \quad (3.17)$$

$$= \cos \phi_1 |\downarrow\rangle \langle \downarrow| (|\uparrow\rangle \langle \downarrow| + |\downarrow\rangle \langle \uparrow|) + i \sin \phi_1 |\downarrow\rangle \langle \downarrow| (|\downarrow\rangle \langle \uparrow| - |\uparrow\rangle \langle \downarrow|) \quad (3.18)$$

$$= (|\downarrow\rangle \langle \downarrow|)(\cos \phi_1(\hat{I}_X) - \sin \phi_1(\hat{I}_Y)) \quad (3.19)$$

$$= \frac{1}{2}(\mathbb{1} - \hat{S}_Z)(\hat{I}_X \cos \phi_1 - \hat{I}_Y \sin \phi_1) \quad (3.20)$$

$$((\cos \phi_2 - i \sin \phi_2) |\uparrow\uparrow\rangle \langle \uparrow\downarrow| + (\cos \phi_2 + i \sin \phi_2) |\uparrow\downarrow\rangle \langle \uparrow\uparrow|) \quad (3.21)$$

$$= \cos \phi_2 |\uparrow\rangle \langle \uparrow| (|\uparrow\rangle \langle \downarrow| + |\downarrow\rangle \langle \uparrow|) + i \sin \phi_2 |\uparrow\rangle \langle \uparrow| (|\downarrow\rangle \langle \uparrow| - |\uparrow\rangle \langle \downarrow|) \quad (3.22)$$

$$= (|\uparrow\rangle \langle \uparrow|)(\cos \phi_2(\hat{I}_X) - \sin \phi_2(\hat{I}_Y)) \quad (3.23)$$

$$= \frac{1}{2}(\mathbb{1} + \hat{S}_Z)(\hat{I}_X \cos \phi_2 - \hat{I}_Y \sin \phi_2) \quad (3.24)$$

$$((\cos \phi_3 - i \sin \phi_3) |\uparrow\downarrow\rangle \langle \downarrow\downarrow| + (\cos \phi_3 + i \sin \phi_3) |\uparrow\downarrow\rangle \langle \uparrow\downarrow|) \quad (3.25)$$

$$= \cos \phi_3 (|\uparrow\rangle \langle \downarrow| + |\downarrow\rangle \langle \uparrow|) |\downarrow\rangle \langle \downarrow| + i \sin \phi_3 (|\downarrow\rangle \langle \uparrow| - |\uparrow\rangle \langle \downarrow|) |\downarrow\rangle \langle \downarrow| \quad (3.26)$$

$$= (\cos \phi_3(\hat{S}_X) - \sin \phi_3(\hat{S}_Y))(|\downarrow\rangle \langle \downarrow|) \quad (3.27)$$

$$= (\hat{S}_X \cos \phi_3 - \hat{S}_Y \sin \phi_3) \frac{1}{2}(\mathbb{1} - \hat{I}_Z) \quad (3.28)$$

$$((\cos \phi_4 - i \sin \phi_4) |\uparrow\downarrow\rangle \langle \downarrow\downarrow| + (\cos \phi_4 + i \sin \phi_4) |\uparrow\downarrow\rangle \langle \uparrow\downarrow|) \quad (3.29)$$

$$= \cos \phi_4 (|\uparrow\rangle \langle \downarrow| + |\downarrow\rangle \langle \uparrow|) |\uparrow\rangle \langle \uparrow| + i \sin \phi_4 (|\downarrow\rangle \langle \uparrow| - |\uparrow\rangle \langle \downarrow|) |\uparrow\rangle \langle \uparrow| \quad (3.30)$$

$$= (\cos \phi_4(\hat{S}_X) - \sin \phi_4(\hat{S}_Y))(|\uparrow\rangle \langle \uparrow|) \quad (3.31)$$

$$= (\hat{S}_X \cos \phi_4 - \hat{S}_Y \sin \phi_4) \frac{1}{2}(\mathbb{1} + \hat{I}_Z) \quad (3.32)$$

Now, multiplying these out with (Eq. 3.21) we get

$$\begin{aligned} \hat{H} = & \left( \frac{B_1}{2} \frac{1}{2} (\mathbb{1} - \hat{S}_Z)(\hat{I}_X \cos \phi_1 - \hat{I}_Y \sin \phi_1) \right. \\ & + \frac{B_2}{2} \left( \frac{1}{2} (\mathbb{1} + \hat{S}_Z)(\hat{I}_X \cos \phi_2 - \hat{I}_Y \sin \phi_2) \right. \\ & + \frac{B_3}{2} (\hat{S}_X \cos \phi_3 - \hat{S}_Y \sin \phi_3) \frac{1}{2} (\mathbb{1} - \hat{I}_Z) \\ & \left. \left. + \frac{B_4}{2} (\hat{S}_X \cos \phi_4 - \hat{S}_Y \sin \phi_4) \frac{1}{2} (\mathbb{1} + \hat{I}_Z) \right) \right). \end{aligned} \quad (3.33)$$

### 3.2.2 Deriving the Full Annealing Hamiltonian with Multiple N-V Centres

Now I want to include interactions between neighbouring qubits, and show that I can derive the quantum annealing Hamiltonian.

Consider that we have two qubits, which will each have their own single qubit Hamiltonian (Eq. (3.33)), as well as a coupling term, as in

$$\hat{H} = \hat{H}_1 + \hat{H}_2 + \hat{H}_{12}, \quad (3.34)$$

where  $\hat{H}_{12}$  represents the electromagnetic interaction between the spins in the NV centres.

This interaction is given by

$$\hat{H}_{12} = \vec{S}_1 \cdot \vec{C} \cdot \vec{S}_2, \quad (3.35)$$

where  $\vec{C}$  is a tensor of coupling values and is due to the magnetic dipole interactions of the two spins. Let's define the separation vector between the two spins as  $\vec{r} = (x, y, z)$ , then the coupling is given by

$$\vec{C} = -\frac{g_e \mu_B}{h} \vec{B}_{\text{dip}}(r) \quad (3.36)$$

$$= \frac{g_e \mu_B}{h} \frac{g_e \mu_B}{4\pi} \frac{1}{r^3} \left( \mathbb{1} - \frac{3(\vec{r}' \otimes \vec{r})}{r^2} \right) \quad (3.37)$$

$$= C_0 \begin{pmatrix} \frac{1}{r^3} - \frac{3x^2}{r^5} & -\frac{3xy}{r^5} & -\frac{3xz}{r^5} \\ -\frac{3yx}{r^5} & \frac{1}{r^3} - \frac{3y^2}{r^5} & -\frac{3yz^2}{r^5} \\ -\frac{3zx^2}{r^5} & -\frac{3x^2}{r^5} & \frac{1}{r^3} - \frac{3z^2}{r^5} \end{pmatrix} \quad (3.38)$$

Making the secular approximation as in Background Section 2.8.1 allows us to neglect all terms not including  $\hat{S}_z \hat{S}_z$ . Further, knowing that the qubits all lie in the  $x$ - $y$  plane means  $z = 0$  and I write

$$\hat{H}_{12} = C_{zz} \hat{S}_{1Z} \hat{S}_{2Z} \quad (3.39)$$

$$= C_0 \hat{S}_{1Z} \hat{S}_{2Z} \left( \frac{1}{r^3} \right) \quad (3.40)$$

So, we can now write down the total Hamiltonian

$$\begin{aligned}\hat{H} = & D(\hat{S}_{1,z}^2 - \frac{2}{3}) + \gamma_e \hat{S}_{1,z} B(x_1) - \gamma_I \hat{I}_{1,z} B(x_1) + \hat{S}_{1,z} A_{zz} \hat{I}_{1,z} \\ & + D(\hat{S}_{2,z}^2 - \frac{2}{3}) + \gamma_e \hat{S}_{2,z} B(x_2) - \gamma_I \hat{I}_{2,z} B(x_2) + \hat{S}_{2,z} A_{zz} \hat{I}_{2,z} \\ & \frac{g_e^2 \mu_B \mu_B}{h} \frac{1}{4\pi} \hat{S}_{1Z} \hat{S}_{2Z} \left( \frac{1}{r^3} \right)\end{aligned}\quad (3.41)$$

Now, as before, we can see immediately that the only operators present are (explicitly)  $\hat{I}_z, \hat{S}_z$  and (implicitly)  $\hat{\mathbb{1}}$ . Therefore, we can immediately conclude that the eigenvectors are going to be the vector products of the spin-z projection states for each qubit.

That is, explicitly, the eigenvectors are

$$\{\boldsymbol{\nu}\} = \left\{ \prod_{i,j,k,l \in \{\uparrow, \downarrow\}} |i\rangle |j\rangle |k\rangle |l\rangle \right\} \quad (3.42)$$

Let's move to qubit notation and call  $|\uparrow\rangle := |1\rangle$  and  $|\downarrow\rangle := |0\rangle$ . Then we can see that our eigenvectors are going to be the computational basis.

I only use one spin projection on the first electron, for simplicity let's say I use the  $| -1 \rangle$  projection. This means that we have eight states, with selection rules on the transitions between them. For the electron spin transition, it must preserve each nuclear spin. The nuclear spin transitions can only flip a single nuclear spin at a time and preserve electron projection. To conserve energy, flipping the first nuclear spin then the second must sum to the same energy as flipping the second followed by the first. This means that there are only two distinct transition energies in each electron spin projection. Expanding all of this out, we produce Fig. (3.4).

If we tune to the transitions that correspond to flipping the electron spin  $B_5(t) \times \omega_5, B_6(t) \times \omega_6$ , and follow the same steps of transforming into the interaction picture and making the rotating wave approximation we generate the following

$$B_5(t)((\cos \phi_5 + i \sin \phi_5) |\uparrow\uparrow\downarrow\rangle \langle \downarrow\uparrow\downarrow| + (\cos \phi_5 - i \sin \phi_5) |\downarrow\uparrow\downarrow\rangle \langle \uparrow\uparrow\downarrow|) \quad (3.43)$$

$$= B_5(t)(|\uparrow\rangle \langle \downarrow| + |\downarrow\rangle \langle \uparrow|)((\cos \phi_5 + i \sin \phi_5) |\uparrow\downarrow\rangle \langle \uparrow\downarrow| + (\cos \phi_5 - i \sin \phi_5) |\uparrow\downarrow\rangle \langle \uparrow\downarrow|) \quad (3.44)$$

$$= B_5(t)(\hat{S}_X \cos \phi_5 + \hat{S}_Y \sin \phi_5)(2 |\uparrow\downarrow\rangle \langle \uparrow\downarrow|), \quad (3.45)$$

and

$$B_6(t)(\hat{S}_X \cos \phi_6 + \hat{S}_Y \sin \phi_6)(2 |\downarrow\uparrow\rangle \langle \downarrow\uparrow|), \quad (3.46)$$

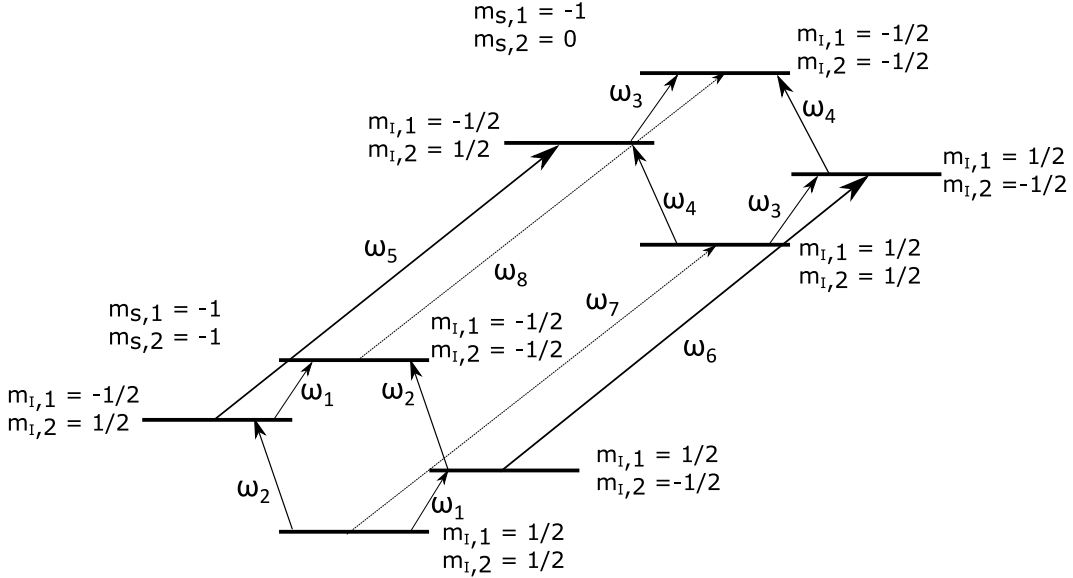


Figure 3.4: The distinct transitions in the subspace that we use for quantum computation with two NV centres, where the transitions in bold,  $\omega_5, \omega_6$  are the ones that produce the quantum annealing Hamiltonian.

setting  $\phi_5 = \phi_6 = 0$  we get

$$\hat{H} = \hat{S}_X(2B_5(t)|\uparrow\downarrow\rangle\langle\uparrow\downarrow| + 2B_6(t)|\downarrow\uparrow\rangle\langle\downarrow\uparrow|). \quad (3.47)$$

Now, setting  $B_5 = B_6$ ,

$$\hat{H} = B(t)\hat{S}_X(2|\uparrow\downarrow\rangle\langle\uparrow\downarrow| + 2|\downarrow\uparrow\rangle\langle\downarrow\uparrow|) \quad (3.48)$$

$$= B(t)\hat{S}_X(\hat{\mathbb{1}} - \hat{I}_{1Z}\hat{I}_{2Z}), \quad (3.49)$$

$$(3.50)$$

giving us exactly the interaction terms that we needed. From one qubit, we already saw that tuning to the single-electron spin transitions gave us the one-qubit terms that we desired.

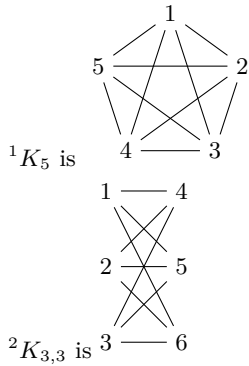
However, we see that there is also the electron operator multiplying the entire equation. So that this has no effect on the adiabatic evolution, we initialise the electron spin in the lower energy  $x$  eigenstate, and factor it from the final N-V Hamiltonian.

$$\hat{H}_{\text{N-V Annealer}} = (1 - s(t)) \left( \sum_i \hat{I}_{i,X} \right) + \hat{S}_X \left( \sum_i B_i \hat{I}_{i,Z} + \sum_{ij} s(t) B_{ij} \hat{I}_{i,Z} \hat{I}_{j,Z} \right). \quad (3.51)$$

### 3.3 The Possible Qubit Connectivity Graphs

In this section I briefly touch upon the qubit connectivity graphs that naturally arise from this design from a qualitative perspective. Clearly, this array design with a separation that allows for coupling only between nearest neighbour N-V Centres produces a square lattice qubit connectivity graph, such as shown in Fig. (3.5a). However, Ising models defined over a planar graph (which includes this square lattice), have an efficient polynomial time approximation scheme [85]. This is extremely important, as it would completely exclude the possibility of the type of quantum advantage that people are most excited about, which is an exponential improvement. Since this polynomial algorithm exists, this problem could be efficiently computed on a classical computer. Furthermore, there are major classes of graphs that, according to Wagner's theorem [86], cannot possibly be a minor of a planar graph. Importantly, this includes a fully connected graph with 5 nodes ( $K_5^1$ ) and a complete bipartite graph ( $K_{3,3}^2$ ) with 6 nodes. Importantly, the Chimera graph that D-Wave use, shown in Fig. (2.2), contains complete bipartite graphs with 8 nodes ( $K_{4,4}$ ). This means that it would be impossible to find a minor for any graph that was native to D-Wave in a square lattice.

Readers who are intimately familiar with the field may have noticed hints of a contradiction, where in Section 2.3, I stated that an arbitrary qubit connectivity graph can be embedded into a square lattice grid with polynomially many qubits using the LHZ architecture [13]. If this were possible, then there would be a polynomial transformation, as well as a polynomial time approximation scheme for an arbitrary graph, which would cause  $P = NP$ . However, the caveats mentioned regarding the LHZ architecture mean that the qubit connectivity graph cannot be thought of as a traditional graph. In particular, it requires either a *qutrit*, a three-level quantum system that is used like a qubit, or a coupling between 4 qubits, which would have to be represented by a *hyperedge* (a graph edge that connects arbitrary numbers of nodes). With these extra degrees of freedom, a contradiction is avoided. Fortunately, the NV Centre can be trivially engineered to operate as a qutrit instead of as a qubit by selecting the isotope of Nitrogen to be Nitrogen-14, which is Spin-1, and therefore has three possible



states. This is shown in Fig. (3.5b).

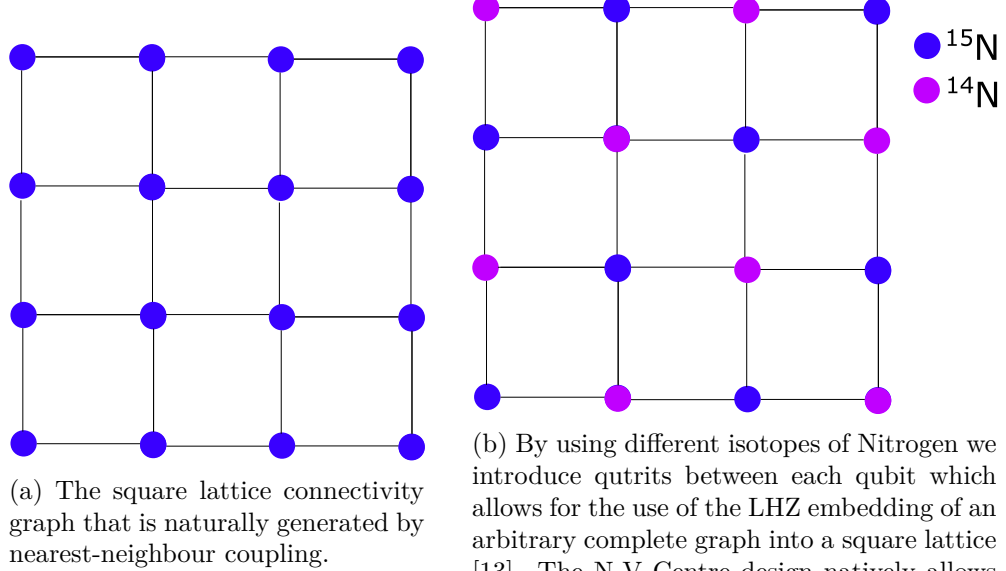


Figure 3.5: The square-lattice of  $^{15}\text{N}$  (left) would have a polynomial time approximation scheme and not be able to accommodate minor embeddings of important classes of graphs. However, through the introduction of Spin-1 Nitrogen-14 atoms we can create qutrits, which allow the use of the LHZ architecture [13], and restores universality.

Despite being theoretically able to embed an arbitrary problem using the LHZ architecture, a recent study found that there was a major scaling overhead for doing so [87]. Therefore, it will almost certainly be worth immediately pursuing denser connectivity graphs, even at the cost of increased decoherence processed by doing so. Fig. (3.6) shows the next two natural iterations of the qubit connectivity graph. To achieve coupling between these qubits however, the separation between adjacent qubits will need to be reduced, to allow for the 0.1 MHz coupling. However, to ensure the separation in frequency, this will mean that the magnetic field gradients will need to increase. As mentioned in the design at the start of this chapter, the magnetic field gradient is produced by wires, and so increasing the magnetic field gradient requires increasing the current through the wires, which rapidly generates too much heat. Therefore, there is a large amount of work that will need to be explored to balance frequency separation and connectivity.

This Chapter presented a novel derivation showing how the Hamiltonian of the N-V Centre can be transformed directly into the quantum annealing Hamiltonian by applying well-known approximations and tuning to the correct transition energies. Furthermore, it explored some of the issues with particular types of qubit connectivity graphs, however highlighted how the N-V Centre is an ideal candidate for the phys-

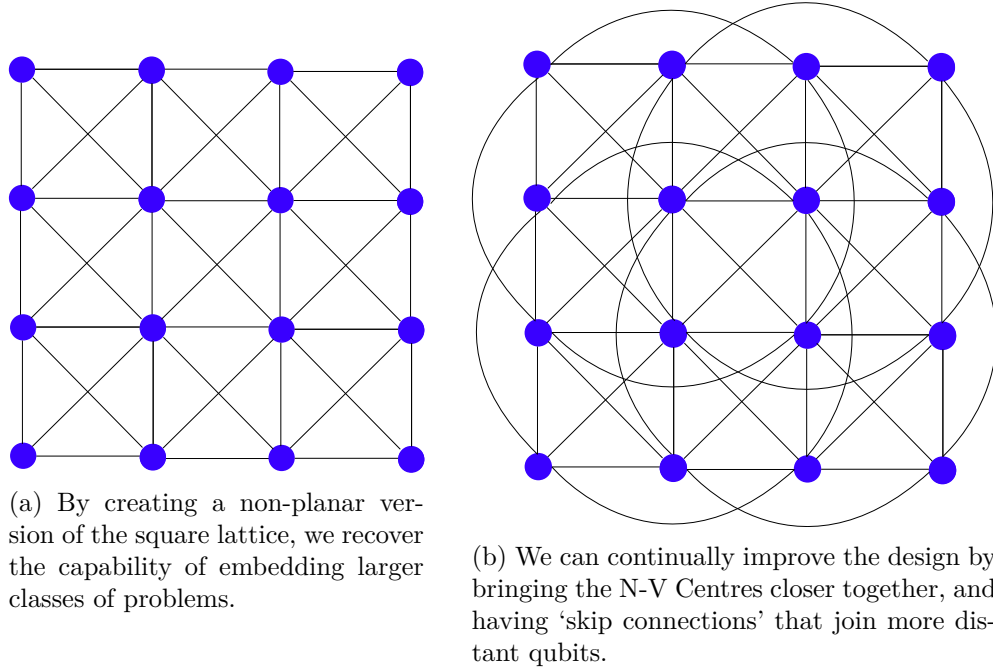


Figure 3.6: The natural next two iterations of the qubit connectivity graph of a diamond quantum annealer, achieved by decreasing the separation between the array of N-V Centres.

ical realisation of the LHZ architecture [13], and then produced a roadmap forward for improving the connectivity. Overall, this Chapter demonstrated that a diamond quantum processor can natively run the Ising Hamiltonian, and could also (depending on design) natively execute arbitrary problems.

---

# Using Ensembles of Diamond NV Centres as Effective Qubits

---

Currently, the design for the quantum computer requires atom-scale fabrication and ultra-precise placement of the NV. These fabrication processes are still being researched, and are likely to be very expensive and with low yield to begin with. By contrast the proposed design uses a well-established technique to produce a high density of randomly distributed spins. Fig. (4.1a) shows the existing design, whereas Fig. (4.1b) shows the design presented here. It's important to note that the inter-effective qubit distance should be able to be much bigger than the 7nm required for the left design, since the many spins produce a larger magnetic field.

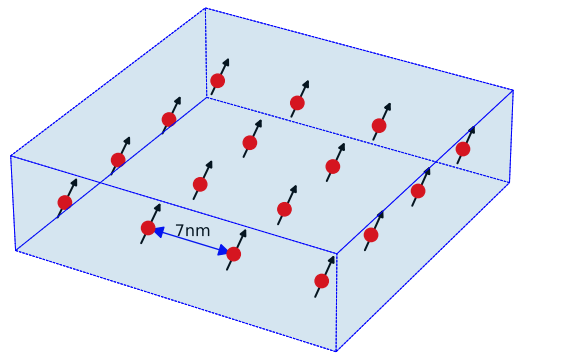
This Chapter explores the possibility of using frequency selection to organise patches of physical NV centres to work together as a single effective qubit.

## 4.1 Effective Qubits

To construct a quantum computer, physical two-level quantum systems need to be manufactured into a medium and then coupled and controlled. As discussed in Section 2.1, this means that describing the full quantum state requires an exponentially large vector. However, to reduce decoherence, improve the total qubit connectivity, simplify or improve readout schemes, or simply due to manufacturing constraints it is often preferable to make collections of physical qubits all identical, degenerate quantum systems. Since many physical qubits are being used as if they were a single qubit, these new collections are called *effective qubits*. These are most commonly used in error-correction schemes, where they can be called *logical qubits*. This term is avoided here to avoid confusion with the logical qubits of an embedded qubit connectivity graph.

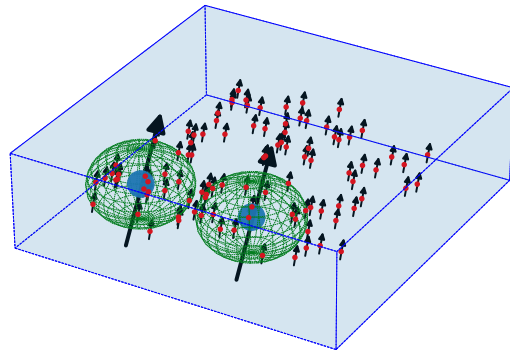
When we use NV-centres as physical qubits, we differentiate them as quantum systems using frequency selection, where the on-resonant transition frequencies depend on the strength of an external magnetic field, and the rotating wave approximation allows us to neglect off-resonant driving with other qubits. However, if we apply a constant magnetic field, then the quantum systems are approximately degenerate.

However, due to the spatial variation of the NV-centres, the coupling between them



● NV-centre

- (a) The existing design requires precise placement of NV Centres in a regular grid with a spacing of approximately 7nm. This is difficult to achieve from an engineering perspective.



● NV-centre  
● Logical qubit  
Region where physical qubits are degenerate

- (b) This proposed design leverages existing manufacturing techniques to create a random dense distribution of NV centres and frequency selection selection to get groups of physical qubits to behave like single qubits

Figure 4.1: The design proposed in this Chapter (4) uses many NV centres as a single effective qubit addressed through frequency selection, allowing me to take advantage of existing manufacturing strategies.

will be distributed. This has the effect of inhomogeneous broadening, which increases the linewidth of the transition. If the broadening is approximately Lorentzian, there is a duality between inhomogeneous broadening and pure dephasing (Section 2.4.1), which we can treat using a Lindblad operator in the master equation.

## 4.2 The Design for a Diamond Quantum Computer based on Effective Qubits

For the first exploration into the use of effective qubits in N-V Centre Diamond, I make the following two assumptions:

- A spherical region of space has an identical magnetic field distinct from its surroundings. Whilst this would violate Gauss' law for magnetism, there is a major benefit in allowing the treatment of one region as a magnetised sphere producing a point dipole.
- The NV-centres are a continuous spin density instead of randomly distributed point dipoles. This increases uniformity and is approximately correct for high densities of N-Vs. This assumption allows for computing the expectation value of interactions between these two systems directly. However, in reality I would generate a detailed picture of where the spins are in reality and optimise over the geometry, suggesting this approximation would underperform smart engineering.

Formally, I consider two magnetised spheres of radius  $R_0$ , one  $S_1$  centred at the origin and the other one  $S_2$  centred at  $(x_0, 0, 0)$  with an internal constant spin density of  $\rho$ . Since  $S_1$  is a magnetised sphere with spherical symmetry, outside the sphere the magnetic field is a dipole which at point  $r = (x, y, z)$  has strength

$$\vec{C}(\vec{r}) = \frac{4}{3}\pi R_0^3 g_e \mu_B \rho \frac{\mu_0}{4\pi r^3} (\mathbb{1} - 3\frac{\vec{r} \otimes \vec{r}}{r^2}) \quad (4.1)$$

Then, the coupling term in the Hamiltonian between the collections of spins and a single spin is

$$H_{\text{int}} = \vec{S}_1 \cdot \iint_{S_2} \vec{C}(\vec{r}') \cdot \rho \vec{S}(\vec{r}') d^3 r', \quad (4.2)$$

where  $\vec{C}(\vec{r}')$  is the same coupling tensor as described in Section (3.2.2) calculated at position  $r'$ , and  $\vec{S}(\vec{r}')$  is the spin vector associated with the volume of spins in  $d^3 r'$ .

Due to the the  $\vec{r}'$  dependence of the coupling tensor, the ‘spins’ in  $S_2$  are inhomogeneous, and instead of there being a single transition energy, there will be a distribution

of energies. To treat this effect as a decoherence term, I calculate the distribution of transition energies. Eq. (4.3) shows how to calculate the probability density of  $\omega_0$ .

$$P(\omega_0) = \frac{1}{V} \iint_{S_2} \delta(\omega_0 - C(\vec{r}')) d^3 r', \quad (4.3)$$

where  $V$  is the volume of  $S_2$ , and  $C(\vec{r}')$  is the coupling strength at  $\vec{r}'$ . Since this integral has a complicated analytic form, I instead take a numerical approach, sampling points randomly distributed throughout  $S_2$ , computing  $C$  at those points, and building up statistics. Doing so produces Fig. (4.2).

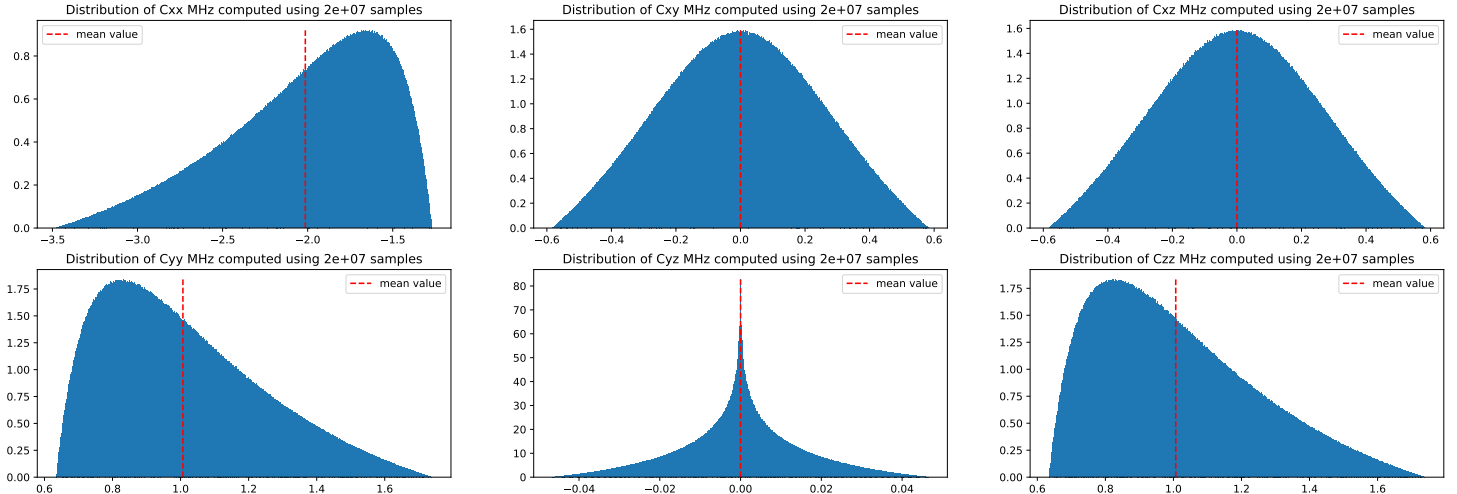


Figure 4.2: The distributions of the coupling tensor components across the volume of  $S_2$

Since these coupling terms are now distributions instead of constants, I treat them as decoherence terms in a Linblad master equation. I make the secular approximation as in Section 2.8.1, which allows us to decompose the secular and non-secular terms. The master equation is then

$$\frac{\partial \hat{\rho}}{\partial t} = -\frac{i}{\hbar}[H, \rho] + \gamma_z \mathcal{L}_{\text{sec}} + \sum_{i,j} \Gamma_{i,j} \mathcal{L}_{\text{non-sec},ij} + \frac{1}{2T_1} \mathcal{L}_{\text{bath}}, \quad (4.4)$$

where  $\mathcal{L}_i$  is the Linblad operator associated with decoherence of type  $i$ ,  $\gamma_z$  is proportional to the width of the secular term distribution,  $\Gamma$  is related to the overlap between state energies, and  $T_1$  is the experimentally known decoherence time of pure diamond.

I firstly treat the secular term, which will be  $C_{zz} S_{1,z} S_{2,z}$ . To take advantage of the

duality between inhomogeneous broadening and pure dephasing discussed in Section 2.4.1, I am forced to fit a Lorentzian distribution to the  $C_{zz}$  component and calculate the full-width at half max (which is the strength of our spin dephasing term  $\gamma_z$  in the Linblad operator). As shown in Fig. (4.3) this is a bad fit. However, the thing that will really matter for the accuracy of the decoherence term will be the (signed) area difference between the fitted Lorentzian and the calculated function. Because our region is bounded, therefore so is our computed distribution, the Lorentzian is still large while the computed distribution is zero. Because of this, this for a rough approximation of the decoherence time associated with this term. Importantly, I had no choice but to make use of a Lorentzian distribution fit because it allows for the dephasing strength to not have time-dependence. In fact, it was only last year that a full study was done into the use of non-Lorentzian (generated by an underlying non-Markovian process) quantum dephasing [30].

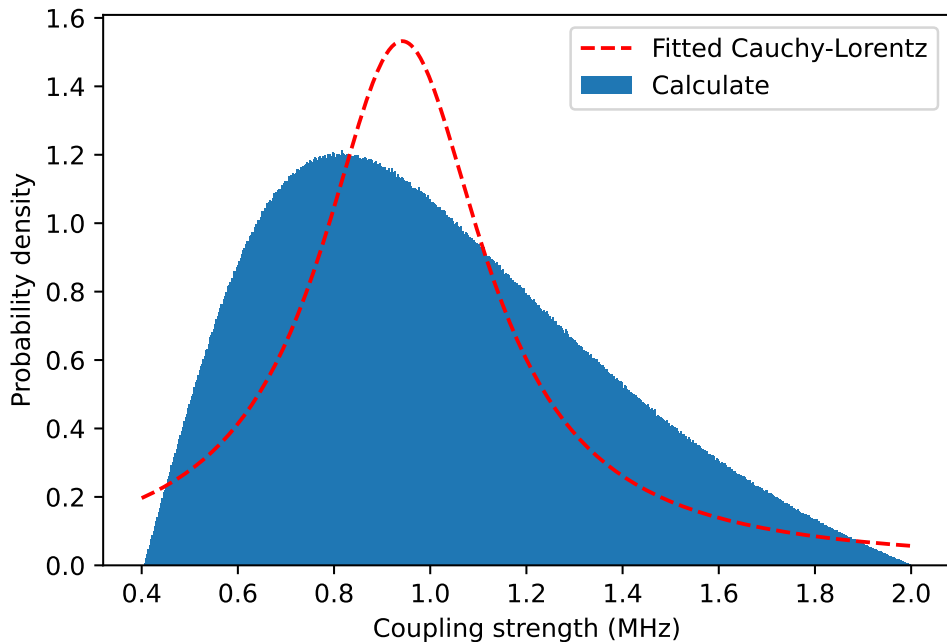


Figure 4.3: The fit overlaid on top of the computed probability distribution. Whilst this is clearly a really bad fit, the important thing is actually the summed area difference, which due to the fact that our region is bounded, and hence the computed distribution is zero where the Lorentzian is still large, the ‘badness’ of this fit will have little impact on the actual computed dephasing time.

The pure dephasing associated with a Cauchy-Lorentz distribution is the same as

the scale parameter of that distribution,  $\gamma$ . For our parameters, that is

$$\gamma_z = 0.207 \text{ MHz} \quad (4.5)$$

Secondly, I treat the non-secular terms using perturbation theory. The perturbative Hamiltonian is

$$\hat{V} = \vec{S}_1 \cdot (\langle \tilde{C} \rangle - \langle C_{zz} \rangle \hat{z}\hat{z}) \cdot \vec{S}_2. \quad (4.6)$$

Looking at Fig. 4.2 it is immediately clear that  $\langle C_{xy} \rangle = \langle C_{xz} \rangle = \langle C_{yz} \rangle = 0$ . The Hamiltonian is then

$$\hat{V} = \hat{S}_{1,x} \langle C_{xx} \rangle \hat{S}_{2,x} + \hat{S}_{1,y} \langle C_{yy} \rangle \hat{S}_{2,y}. \quad (4.7)$$

Applying Fermi's golden rule I calculate the transition rate for each of the possible states of the system, which are simply the spin-1/2 projections of each electron. Fermi's golden rule calculates the transition rate from an arbitrary state  $|i\rangle$  to  $|j\rangle$  using

$$\Gamma_{ij} = \frac{2\pi}{\hbar h} \left| \langle j | \hat{V} | i \rangle \right|^2 \rho(\Delta ij), \quad (4.8)$$

where  $\rho(\Delta ij)$  is the density of states with that transition energy. By enumerating all possible transitions, I calculate the expectation value of each component. Then, To calculate the density of states  $\rho(\Delta ij)$ , I consider the overlap between transition energies of the states based on the fitted Cauchy-Lorentz distribution with scale parameter  $\gamma_0$  as in Eq. (4.9)

$$\rho(\Delta ij) = \int P(\omega; 0, \gamma_0) P(\omega; \Delta ij = \gamma_e \Delta B, \gamma_0) d\omega, \quad (4.9)$$

where  $P(\omega; x_0, \gamma)$  is the Cauchy-Lorentz distribution centred at  $x_0$  with scale parameter  $\gamma$ .

Doing this calculation produces

$$\Gamma_{\text{non-sec}} = 3.597 \times 10^{-4} \text{ MHz}. \quad (4.10)$$

Finally, the experimentally known decoherence time of the NV-centre is approximately  $T_1 = 1$  ms, therefore

$$\Gamma_{\text{bath}} = \frac{1}{2T_1} 5 \times 10^{-4} \text{ MHz}. \quad (4.11)$$

We see that the dominant decoherence channel is the dephasing and that our overall

decoherence parameter and time is approximately

$$\Gamma = \Gamma_{\text{non-sec}} + \Gamma_{\text{bath}} + \gamma_z = 0.207 \approx 0.2 \text{MHz} \quad (4.12)$$

$$T_{\text{decoherence}} = \frac{1}{\Gamma} \approx 5 \text{ } \mu\text{s}. \quad (4.13)$$

Putting this all together, I write down the Hamiltonian

$$\hat{H}_{\text{eff}} = \hat{H}_{\text{intrinsic}, 1} + \hat{H}_{\text{intrinsic}, 2} + \langle C_{zz} \rangle \hat{S}_{1,Z} \hat{S}_{2,Z}, \quad (4.14)$$

where  $\hat{H}_{\text{intrinsic}}$  is the Hamiltonian of a single N-V Centre. Then, everything else is accounted for in the master equation

$$i\hbar \frac{\partial \hat{\rho}}{\partial t} = [\hat{H}_{\text{eff}}, \rho] + \gamma_z \mathcal{L}(\hat{S}_{2z}) + \Gamma \mathcal{L}(|\uparrow\downarrow\rangle\langle\downarrow\uparrow|) + \frac{1}{2T_1} \mathcal{L}_{\text{bath}}, \quad (4.15)$$

Following an identical argument as for the multiple qubit case in Section 3.2.2, the coupling strength  $\Omega$  between adjacent qubits is then  $\langle C_{zz} \rangle$ . With this we can enforce that the driving must be executed within the decoherence time through the inequality

$$\Omega t_{\text{anneal}} \gg \Gamma \implies t_{\text{anneal}} \ll \frac{\Omega}{\Gamma}. \quad (4.16)$$

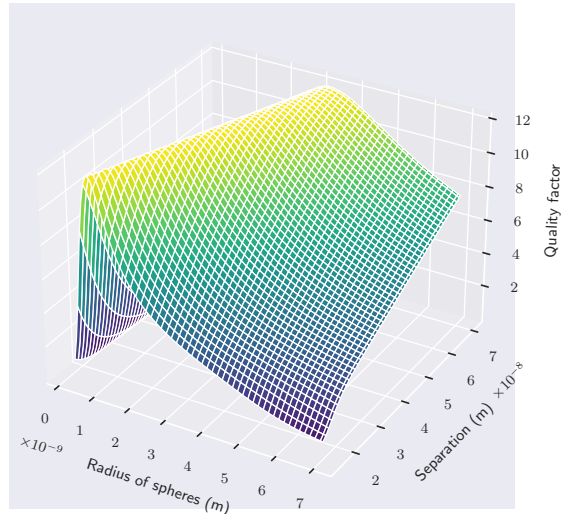
This gives us a parameter  $\frac{\Omega}{\Gamma}$ , the *Quality factor*, that I will optimise.

### 4.3 Optimising the Geometry for the Quality Factor

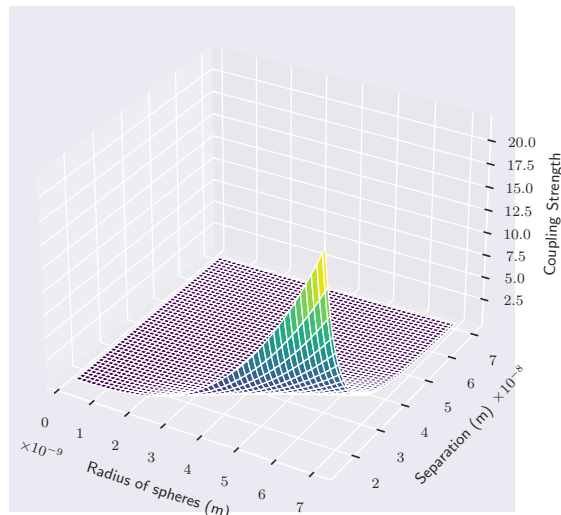
In this section, we optimise the two free parameters the radius of the sphere  $R_0$ , and the separation  $x_0$  in the model above for differing values of the continuous spin density  $\rho$ . This was done by fixing the value of  $\rho$ , and creating a dense grid of possible  $R_0, x_0$  pairs. Then the computation done in Section (4.2) is performed for each of these pairs. Fig. (4.4) shows that whilst very high Quality Factors can be achieved, the optimum is actually outside of the usable range since the coupling is too small for the applied field.

As such, we set a constraint to look only at the locations in the Quality Factor plot Fig. (4.4a) where  $\Omega > 1$ . To determine the sensitivity to the density, we calculated for a range of densities, producing Fig. 4.5. Interestingly, there is little variation in the optimal radius. This is because, as can be seen in Fig. (4.4a), the surface is reasonably flat along the radius dimension, whereas grows rapidly along the separation. The quality factor is then approximately  $\frac{\omega}{\Gamma} = 5$ .

Comparing this to D-Wave, which has a decoherence time of approximately 5 ns,

The Quality Factor for  $\rho=1$  against separation and radius

- (a) The Quality Factor is highest when the radius and separation are small, however in this regime  $\Omega$  is too small to be useful.

The Coupling Strength  $\Omega$  for  $\rho=1$  against separation and radius

- (b) The Coupling Strength is too small to be useful for most values in the space so we set a constraint of  $\Omega > 1$ .

Figure 4.4: By fixing a minimum usable value of  $\Omega$  based on applied field noise, we can find the optimal separation and radius using a grid search.

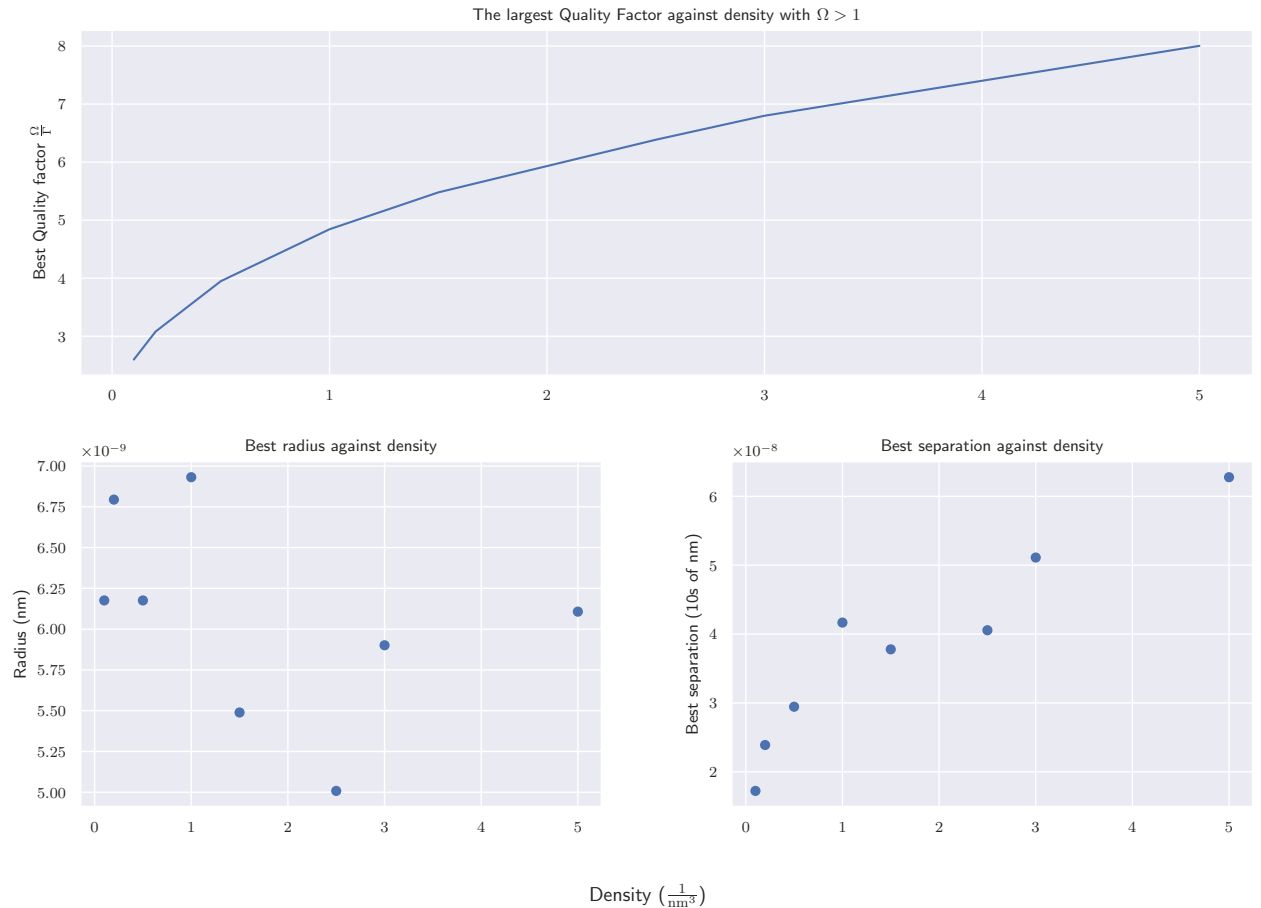


Figure 4.5: Top: The optimal Quality Factor against the density. We can see that in all cases our quality factor is on the same order as D-Wave's (5). However, it seems that for large values of the density, it does begin to saturate, and that it looks like it might start declining sharply for densities lower than the minimum of 0.1 considered here. Bottom: The optimal radius and separation against the densities. Interestingly, these are non-monotonic. Without more points, it is hard to guess at what functional form the relationship takes, and why.

and a maximum coupling of approximately 1 GHz [88], they have a Quality Factor of

$$Q_{\text{ours}} = 5 \quad (4.17)$$

$$Q_{\text{D-Wave}} = 5. \quad (4.18)$$

Therefore, even in the worst case we have an approximately equal Quality Factor as the major competitor D-Wave. Furthermore, as manufacturing improves, this quality factor will only continue to improve. Importantly, having a similar quality factor would allow for an experimental comparison between the importance of the thermal effects in the D-Wave device, since the diamond quantum annealer would operate at room temperature, and have a similar quantum decoherence profile. This would be extremely exciting research as it would be clear experimental evidence as to whether D-Wave was really a quantum device.

#### **4.4 Implications and Avenues for Future Work**

This design clearly has strong potential for constructing a quantum annealer. Furthermore, this design can easily be changed without building a new device. If deeper analysis determines that a different external magnetic field geometry performs better, or that empirically we should reduce the Quality Factor to improve coupling, these are simple changes that have almost no engineering cost to implement.

However, this analysis neglects some important aspects of ‘quantum annealing’ as it is currently performed. When D-Wave performs quantum annealing, they use an anneal time of approximately  $20 \mu\text{s}$ , many orders of magnitude higher than the decoherence time, and in direct violation of the adiabatic condition. Therefore, they cannot be exploiting solely quantum effects during their anneal, relying on the cold  $25 \text{ mK}$  environment to leverage classical annealing as well. In this device, since the shortest timescale is a dephasing and not a decoherence into the external environment, then we can consider our device to operate cold for a period of time after the quantum phase information is random, also leveraging classical annealing. As of yet, there is no understanding of how to efficiently simulate quantum annealing followed by classical annealing in a way that mirrors what is seen experimentally [89, 90]. As such, understanding the trade-off for this design requires building the design.

Furthermore, since this design can change at no cost, it would be very useful as a test-bed for understanding the effects of Qubit Connectivity Graphs. Since the coupling extends over longer distances, we can sacrifice the Quality Factor of pairs of coupled qubits to connect them over longer regions, which allows for denser connectivity graphs.

# Understanding the Diamond Quantum Annealer compared to D-Wave Advantage and an Ideal Quantum Annealer through Instance Space Analysis

---

In this Chapter I explore a comparison between the diamond quantum annealing design presented in Chapter 4, an ‘ideal’ quantum annealer, and D-Wave’s latest generation Advantage quantum processor. I compare these using a performance metric that relies on the brute force calculation of the optimal energy. In doing so, I

- explore the extent to which D-Wave Advantage can be modelled as a quantum Annealer.
- explore the effects of decoherence on performance.
- compare the diamond quantum annealer to the physical quantum annealer implemented by D-Wave through performing the first Instance Space Analysis with data generated by a real quantum device.

## 5.1 The Maximum Cut Problem

To compare these approaches I used the common graph problem of Maximum Cut (MaxCut). MaxCut is a common benchmark problem since it is extremely simple, and forms part of the complexity class NP-Complete [91]. When a problem is NP-Complete, that means that there exists an isomorphism between *every* problem in the broader complexity class NP and the problem that is NP-Complete. Directly, this means that if a polynomial time algorithm is found to a single NP-Complete problem, then instantaneously P=NP and the polynomial hierarchy collapses. By contrast, if a polynomial time algorithm is found for a generic NP problem, it just changes the complexity class of that problem, and does not necessarily collapse the

hierarchy. This means that NP-Complete problems are at least as difficult as any other NP problem. [91] Furthermore, not only is it NP-Complete, it is also APX-Hard [92]. An APX-Hard problem means that there cannot exist a polynomial time algorithm that can be guaranteed to get within some  $\varepsilon$  of the best solution. This means that any existing efficient algorithms are purely heuristic and effective based on empirical evidence, with strong theoretical foundations being mathematically impossible. For context, the Travelling Salesman Problem (as well as many other graph optimisation problems) are also NP-Complete and APX-Hard, so strong MaxCut performance is good evidence for strong general graph optimisation performance.

For these reasons as well as its simplicity, MaxCut has become a standard benchmark problem for quantum computation [9, 93, 94].

The Maximum Cut problem is the problem of partitioning the nodes of graph, generally labelled  $x_1, \dots, x_n$ , into two disjoint sets  $L, R$  such that the maximum number of edges connect a node from  $L$  to a node from  $R$ . As a concrete example, Fig. (5.1) shows three possible partitions of a graph with three different disjoint nodes, where the right ‘cut’ is clearly optimal.

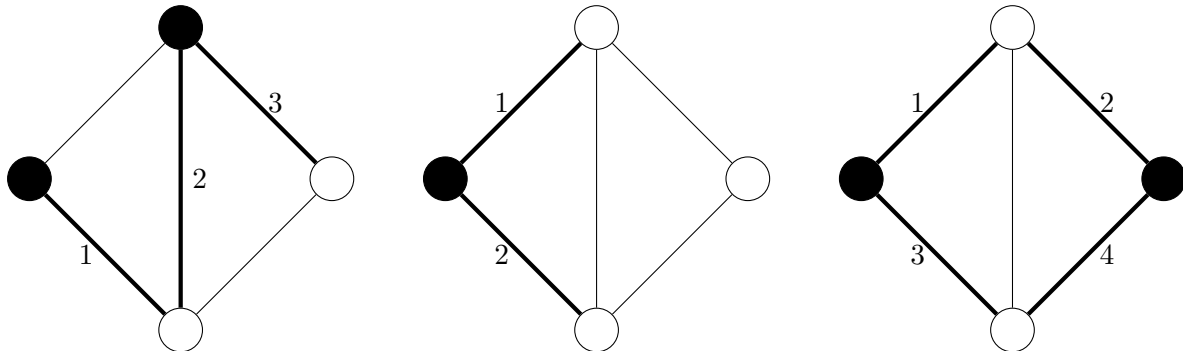


Figure 5.1: Three possible partitions (or cuts) of a graph with four nodes and five edges, where the right graph corresponds to the optimal. Clearly, the optimal can be non-unique such as in the case of a direct swap of the nodes assigned to  $L \leftrightarrow R$ . However, other non-trivial degenerate solutions can also exist. Taken from Author’s work [95]

We can formulate the MaxCut problem in terms of an Ising Hamiltonian (and equivalently a QUBO), by allows nodes in the set  $L$  to take the value  $-1$ , and nodes in the partition  $R$  to take  $+1$ . Then, we can write the objective function as

$$C(x_1 \dots x_n) = \sum_{i,j \in E} \frac{1 - x_i \times x_j}{2}, \quad (5.1)$$

where  $E$  is the set of edges connecting nodes  $x_i, x_j$ . Clearly, if  $x_i \neq x_j$ , then  $(1 - (-1)(1))/2 = 2/2 = 1$ , and if  $x_i = x_j$  then  $1 - 1 = 0$ , so this counts the number

---

of edges that connect nodes from opposite sets. By convention (and for quantum Hamiltonians) we want to minimise a cost function, so we just take the negative to get

$$\text{Loss} = -C. \quad (5.2)$$

## 5.2 Methods

I generate 115 10 node graph problems generated using Algorithm 1 (taken from Author’s work [95]). Then, I run a statevector simulation of quantum annealing using a linear schedule for  $3\mu\text{s}$  to act as a benchmark, a density matrix simulation using the decoherence parameters from Chapter 4, submit the job to the physical D-Wave Advantage quantum processor, and finally run a brute-force solver to find the true optimal.<sup>1</sup>

---

**Algorithm 1** Random connected graph generation function

---

**Require:**  $n > 0, p \in (0, 1]$

```

1: procedure GENERATERANDOMGRAPH( $n, p$ , seed)
2:   Graph  $\leftarrow$  GraphWithoutEdges (numNodes  $\leftarrow n$ )
3:   Edges  $\leftarrow$  Combinations (popSize  $\leftarrow n, 2$ )
4:   RandomGenerator  $\leftarrow$  Random.Uniform (0,1,seed)
5:   for all Edge of Edges do
6:     if RandomGenerator.Produce()  $\leq p$  then
7:       Graph.AddEdge (Edge)
8:     end if
9:   end for
10: end procedure

```

---

For each of these graphs, I calculate features in Table 5.1 following other graph optimisation problems [81].

The performance criteria is simply

$$P_{\text{algo}} = \frac{\langle L \rangle}{L_{\text{optimal}}}, \quad (5.3)$$

where  $\langle L \rangle$  is known exactly for the density matrix and statevector simulations and is calculated from 50 runs of the D-Wave device.

Then, I run an Instance Space Analysis using Matilda [81].

---

<sup>1</sup>Code can be found at <https://github.com/milanleonard/QuantumAnnealers>

Graph Features	
Feature type	Feature name
Node and edge statistics	Number of edges Graph density Min, Max, Std, Mean, Harmonic Mean, Geometric Mean, Skewness, Kurtosis of Node Degree
Graph structure	Number of 3-cycles Average shortest path Average Clustering Graph diameter Graph radius
Spectral properties	Connectivity Laplacian Energy Log ratio of largest eigenvalues of the normalised Laplacian matrix Log ratio of smallest eigenvalues of the normalised Laplacian matrix

Table 5.1: The graph features used are all easily computable using any reputable graph computation library in polynomial time in the number of nodes in the graph.

### 5.3 Projecting the Instance Space into 2-Dimensions

The first step in running an ISA is to understand a compression of the feature space into a two-dimensional form. Before doing so, I calculate the correlation matrix as shown in Fig. 5.2. This shows that there are really not many independent features, with many features being dependent (correlation of  $\pm 1$ ) on another, or strongly correlated. Future work should definitely consider finding a larger set of significantly less correlated graph features that could be used. However, this could also be a product of the small (10 nodes) graphs that I am forced to use due to computational time constraints. To reduce the computational runtime, I remove all features that have a correlation of 1 with another feature since this information is redundant.

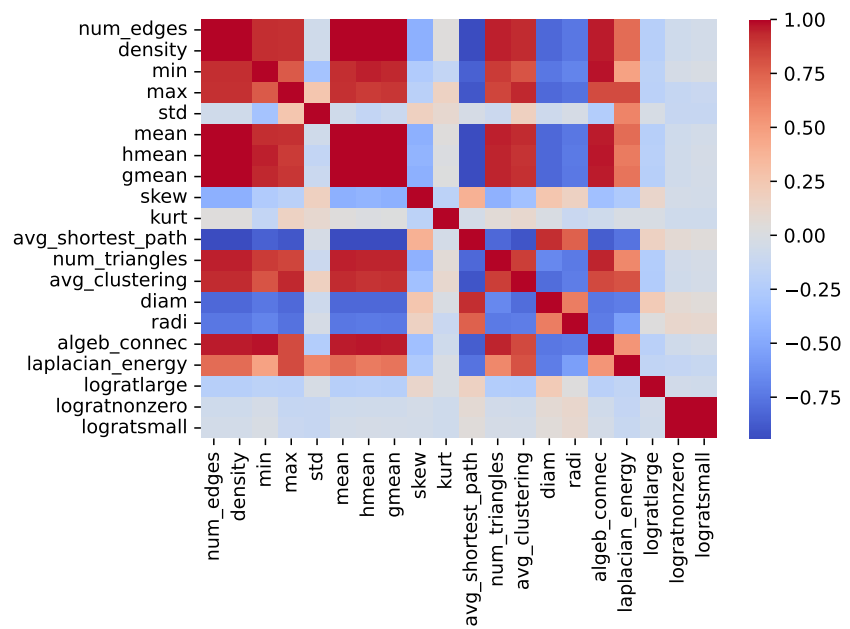


Figure 5.2: The correlation matrix between the features listed in Tab. 5.1 shows extremely strong correlations between many of the graph features, which limits the usefulness of collecting as many features. This highlights the need for considering new graph features or performing this analysis using larger numbers of qubits, which could not be done due to computational constraints.

The compression of the feature space after removing redundant features is

$$\begin{bmatrix} Z_1 \\ Z_2 \end{bmatrix} = \begin{bmatrix} -0.723 & -0.6201 \\ 0.1355 & -0.3063 \\ -0.0583 & -0.2686 \\ -0.4099 & 0.03 \\ -0.6365 & 0.3332 \\ 0.3116 & -0.5797 \\ 0.0348 & 0.3242 \\ 0.2699 & 0.3984 \\ 0.1284 & -0.3306 \\ -0.9809 & -0.0468 \end{bmatrix}^T \begin{bmatrix} num\_edges \\ min \\ max \\ skew \\ avg\_shortest\_path \\ avg\_clustering \\ diam \\ radi \\ laplacian\_energy \\ logratlarge \end{bmatrix}. \quad (5.4)$$

## 5.4 How Legitimate are Comparisons to the D-Wave Device?

As of now, there has been no study into whether D-Wave behaves like an actual quantum annealer through the lens of an instance space analysis. The closest analysis was done by Steiger et al. (2015) [96], where they looked at distributions of success between simulated quantum annealing (SQA, the path-integral Monte Carlo version, not full statevector simulation), simulated classical annealing and the D-Wave device. They concluded that D-Wave must be somewhat quantum since it had a success probability distribution that was more like SQA than classical annealing. However, there are many factors that could have generated this result, which were not discussed in the paper, including sources of error, qubit connectivity etc.

Therefore, by leveraging the ISA technique, we can compare the distribution of instance performance between D-Wave and an ideal quantum annealer. Doing so produces Fig. (5.3), where the difficulty of an instance as viewed by D-Wave's device is radically different to that of an ideal quantum annealer. Whilst this is not necessarily direct evidence that D-Wave is not performing as a quantum annealer, since D-Wave has to perform a minor embedding into their native graph, it highlights the difficulties in doing a comparison between different computing architectures through simulated dynamics, as an apples-to-apples comparison using D-Wave's embedded version of the problem is not possible.

The obvious solution is to only analyse graphs that are native to D-Wave, or to perform a minor embedding to the graph that we construct. For the first approach, it has been shown that the class of graphs that are native to D-Wave (planar arrangement of bipartite cells), are extremely easy instances of the MaxCut problem [97]. The second

approach would be ideal, but density matrix simulations requires  $O(2^{2n})$  bits and operations, and rapidly becomes infeasible, meaning that with the limited computational power I could only simulate trivial graphs.

Unfortunately, meaningful comparisons to the D-Wave device are not possible with the computational resources I have access to. Future work should consider if there are computational tricks like tensor network simulation of noisy quantum operations that could be used to make more efficient use of the available computational resources.

## 5.5 The Computational Cost of Decoherence

One of the major unanswered questions in the field is exactly how various forms of error effect quantum annealing. In 2019, Pearson et al. showed that large analog errors in the control Hamiltonian cause a worse scaling in the time-to-solution than an exhaustive brute-force classical solver via a mechanism known a *J-Chaos*[98]. Being worse than brute-force is clearly as bad as it can possibly be, however they showed that with simple error suppression they could drastically mitigate this effect. A comprehensive theoretical study into decoherence driven by dephasing was performed by Ablash and Lidar (2015), where they showed a theoretical foundation for how quantum effects can persist past the dephasing time  $T_2$ [99]. Whilst this theoretical foundation was established, in the absence of thermal effects it is clear that the optimal annealing time is still less than  $T_2$ , as shown in Fig 5.4. One thing which has not been studied, is the scaling behaviour of the decoherence effect, which is numerically studied in this Section for the specific case of the diamond quantum annealer.

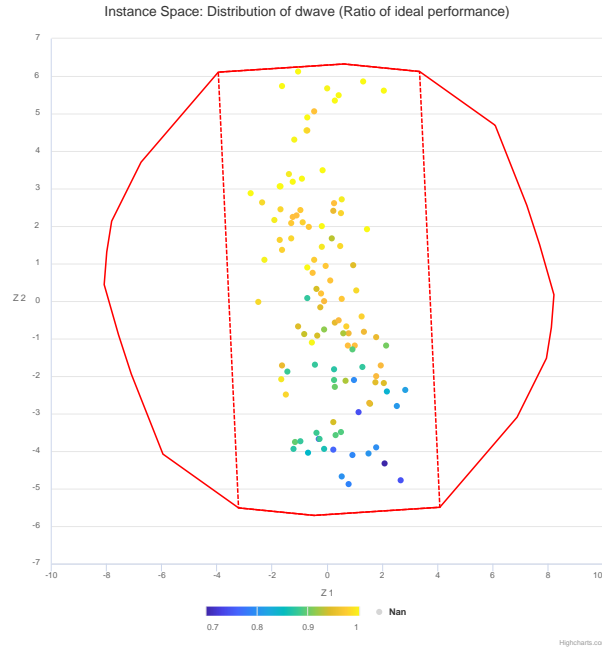
To do so, I continue with the MaxCut example, and generate many instances from 5 to 10 nodes, with the anneal time of  $3 \mu\text{s}$ , and seek to understand the difference in performance between the ideal and diamond. Performance is defined in the same way as above. Doing so produces Fig. (5.5), where we can see two clear trends. Less surprisingly, there is a significant cost to performance through the introduction of decoherence. More surprisingly, and very promisingly, this difference seems to be scale independent. That's not to say that more nodes don't have a negative effect on the overall success which is clear, but instead that the degradation in relative performance seems scale independent.

To analyse the second point in more detail, we define the performance delta as

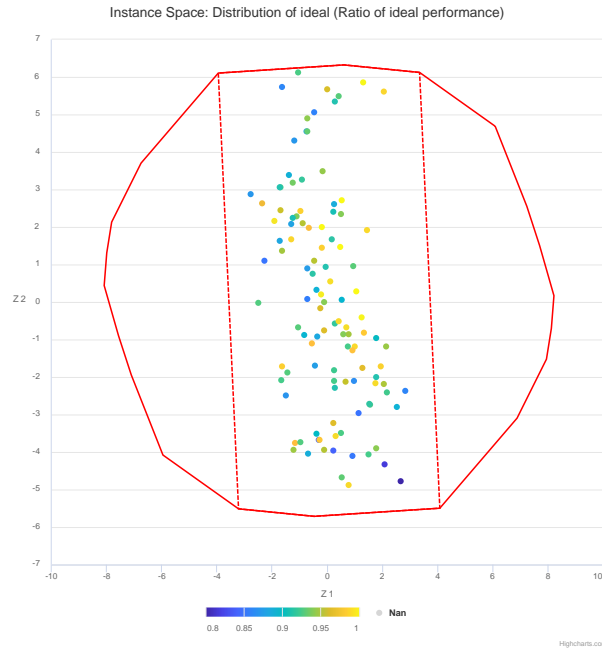
$$\Delta_{\text{performance}} = L_{\text{ideal}} - L_{\text{diamond}}. \quad (5.5)$$

We calculate the mean per number of nodes producing Table 5.2 which reinforces this conclusion.

However, as discussed in background Section 2.9, looking at the mean performance



(a) D-Wave shows a strong trend that as  $Z_2$  decreases and as  $Z_1$  increases, there is a sharp decline in performance.



(b) The ideal quantum annealer, on the other hand, seems to have a reasonably random distribution of performance.

Figure 5.3: By comparing the performance of the D-Wave quantum annealer against the ideal quantum annealer, we see that D-Wave is not viewing the difficulty of a problem in the same way that the the ideal quantum annealer is.

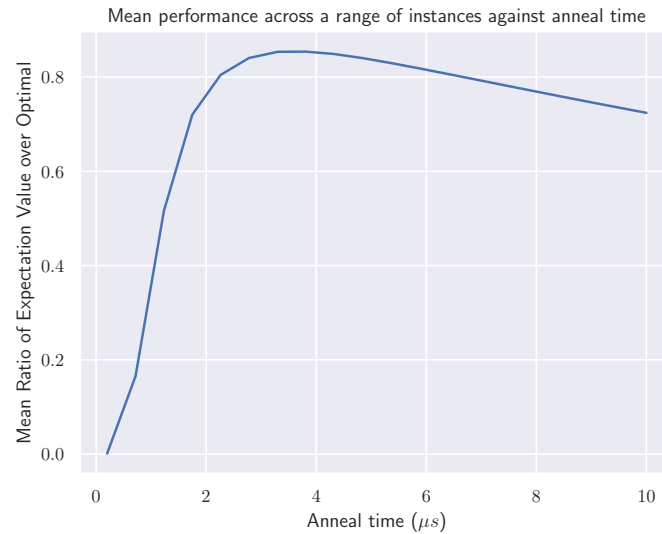


Figure 5.4: I choose an annealing time which is optimal across a random range of MaxCut problems of different sizes, being  $3\mu\text{s}$ .

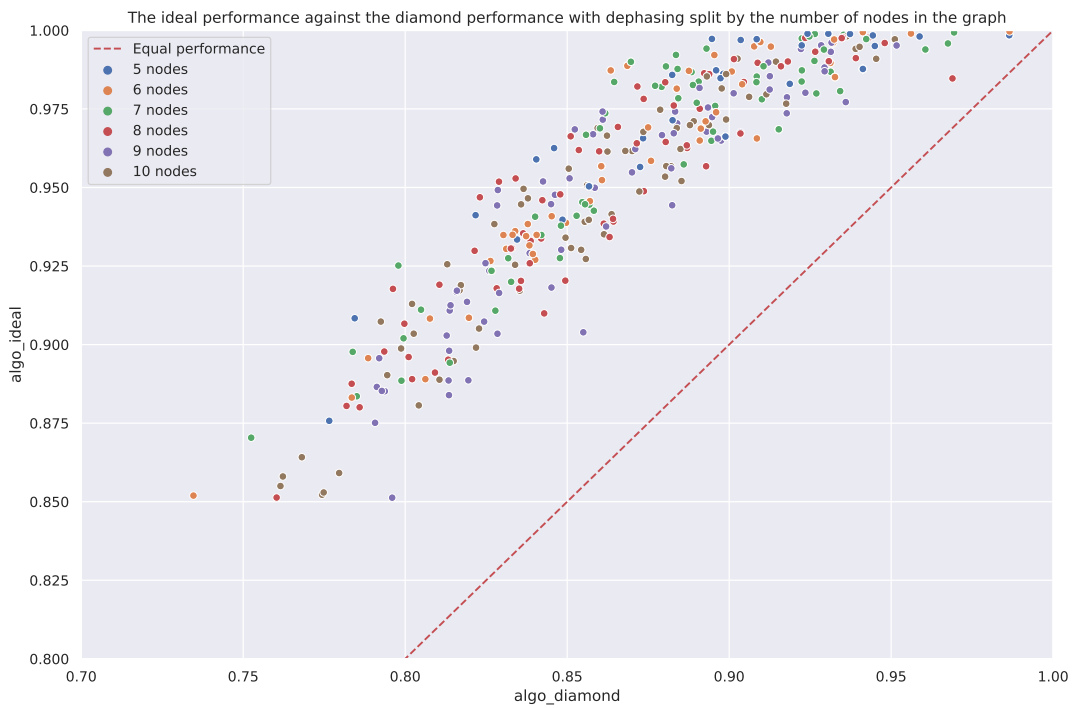


Figure 5.5: Plotting the optimal annealing result against the result achieved from simulating decoherence in a diamond quantum annealer reveals that the performance degradation due to dephasing seems to be scale independent.

Number of nodes	Mean Delta
5	0.0780
6	0.0854
7	0.0824
8	0.0862
9	0.0830
10	0.0852

Table 5.2: The mean performance delta does not depend on the number of nodes.

can be misleading. As such, we produce Fig. 5.6, where it is clear that the large overlap in the histograms does not depend on the number of qubits.

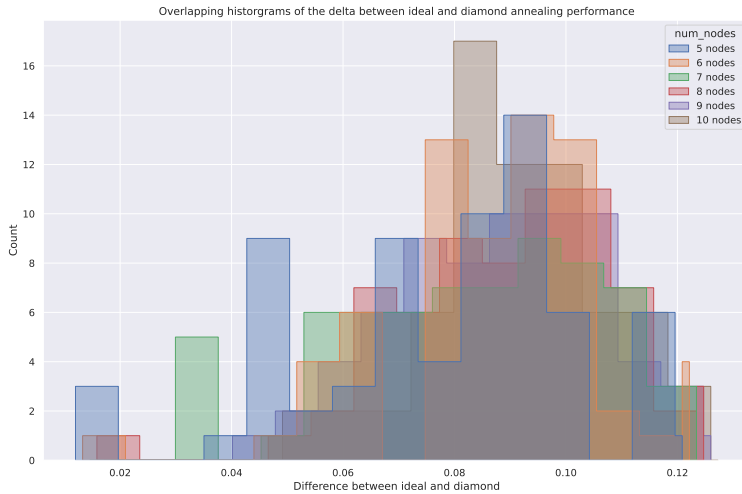


Figure 5.6: The histograms of the difference in performance show that the distributions are approximately equal regardless of the number of nodes in the computational problem.

This is an important result, as it suggests that the negative effects of decoherence do not seem to scale with the number of qubits involved in the quantum annealing computation.

# Conclusion

---

On two occasions I have been asked [by members of Parliament], 'Pray, Mr. Babbage, if you put into the machine wrong figures, will the right answers come out?' I am not able rightly to apprehend the kind of confusion of ideas that could provoke such a question.

---

*Charles Babbage  
Life of a Philosopher (1864) [1]*

Charles Babbage, famous as "the father of computing" and inventor of the first mechanical computer, remarked in his 1864 book *Passages from the Life of a Philosopher* disbelief at the confusion of optimistic parliamentarians about the deterministic nature of computation and its ability to solve all their problems [1]. The answer to Parliament was of course a resounding no. Amusingly, with the upcoming revolution of quantum computing, the answer to their question is 'well, sometimes,' and even when the right figures are put into the machine, the answer is still sometimes, but hopefully *more often*.

Since Babbage and his difference engine, computation has become a critical piece of modern society. However, we have discovered that the computers we currently rely on have whole classes of problems we will likely never be able to solve. For these problems, computer scientists have gotten comfortable with accepting that sometimes the right answer is the one that can be efficiently computed, and not the one that would be optimal. Quantum computing in both of its proposed realisations, adiabatic or gate-based, promise to dramatically expand computational capability.

However, as discussed in the literature review of Chapter 2, there are still major challenges to be solved to fulfil these promises. Noting that there is a massive disparity between investment into gate-based approaches and adiabatic approaches, with a huge lean towards the former, this thesis has focused on designing the first scalable adiabatic quantum computer using diamond N-V Centres, and attempting to understand how it would perform on as many relevant metrics as I could discover.

For the fundamental design of an adiabatic quantum computer a series of problems need to be solved. In particular, in Chapter 3 I showed a design that could be realised through atom-scale fabrication techniques. Firstly, I demonstrated how it was possible to leverage the dipole-dipole interaction of two NVs to allow for coupling. I described

the different types of qubit connectivity that was possible, and highlighted the trade-offs between frequency separation of adjacent NV Centres and the qubit connectivity. Then, I derived the quantum annealing Hamiltonian from the Hamiltonian of the NV Centre by making a series of reasonable common quantum mechanical transformations and approximations. I highlighted how careful selection of the phase and amplitudes of control fields allowed for implementation of an arbitrary Ising Hamiltonian.

The design in Chapter 3 assumed access to proposed atom-precise manufacturing capabilities. In Chapter 4, with the focus on how adiabatic quantum computing is likely to be an intermediate technology as gate-based quantum computing is developed, I introduced a design using existing manufacturing techniques. In particular, I demonstrated how using regions of equal magnetic field led to having near-degenerate physical qubits. Utilising this near-degeneracy allowed the creation of effective qubits, which could be treated for as if they were a single qubit with extra decoherence terms. This treatment allows directly using the results derived in Chapter 3. These decoherence terms, larger than for the ideal design in Chapter 3, depended on geometry parameters of the design. This naturally led to a key metric, the quality factor, which was the coupling strength divided by the decoherence parameter, which defined the total time available for adiabatic quantum evolution. This design was parameterised by the size of the magnetic field regions, the separation between effective qubits, and the density of N-V Centres. The density should be maximised as far as manufacturing will allow, however I optimised the quality factor over a range of manufacturable densities. This revealed that the design was highly resilient to the density, with even the lowest densities considered producing a quality factor that was en par with a fully commercial quantum annealer produced by D-Wave.

Finally, in an attempt to understand the differences between the designs in Chapters 3 and 4, and how they compare to D-Wave's commercial device, I performed the first Instance Space Analysis of noisy and physical quantum annealers. This highlighted the difficulties in comparing quantum annealers due to differing native qubit connectivity graphs. In particular, it demonstrated that the instances that are difficult for D-Wave's quantum annealer, were not the same as for an ideal fully connected quantum annealer. Then, I compared between an ideal quantum annealer and the diamond quantum annealer design as in Chapter 4. This revealed a surprising but extremely promising result, which was that the dramatically reduced dephasing time did not seem to negatively impact how the quantum annealer scaled. However, due to computational constraints, this could only be empirically verified for a small number number of qubits.

In summary, this work provides the theoretical and practical considerations required for creating a diamond adiabatic quantum computer (AQC). Furthermore, it seeks to understand how existing manufacturing techniques could be leveraged to build the

diamond AQC as an intermediate stepping stone between now and the long-term goal of fault-tolerant gate-based quantum computing. Lastly, it compared the diamond quantum annealer to the best existing devices and concluded that even the first iteration of the diamond device would be as good as the very best existing devices, with the potential to be dramatically improved.

## Future Work

This thesis has laid out a roadmap for realising adiabatic quantum computation using diamond NV Centres. Achieving this requires four milestones. Firstly, will be through experimental verification of annealing of the form derived in Chapter 3 on a single NV Centre with neighbouring Carbon-13 atoms. By performing this demonstration on a single NV Centre using neighbouring Carbon-13 atoms as extra qubits, there are no considerations around manufacturing, and the demonstration could follow exactly the methods used when the NV was demonstrated as a gate-based quantum computer. Secondly, will be to show that the design is scalable by doing quantum annealing across multiple NV Centres using the derivations in Section 3.2.2. Thirdly, will be to obtain a sample of high-density NV Centre, and construct a design that uses effective qubits as in Chapter 4. Finally, there will be the construction and then miniaturisation of a precisely fabricated array of single NV Centres, and then implementing adiabatic quantum computing on it. When this is done, studies into whether a truly quantum device provides a computational advantage through quantum annealing will be performed to determine its commercial viability.

Alongside executing this roadmap, there is immense value in deepening our understanding of the qubit connectivity graphs that are naturally afforded by the lattice approach. Unlike superconducting loops, which naturally extend along long superconducting wires allowing for more exotic connectivity graphs, the lattice can only get denser allowing for the qubit connectivity graphs (and their obvious extensions) discussed in Section 3.3. This study should seek to understand the classes of minor graphs which can be embedded into a densely connected lattice, and to determine heuristic algorithms for finding these embeddings.

Lastly, unlike D-Wave’s device which takes advantage of thermal effects due to operating at 25 mK, the diamond adiabatic quantum processor will be operating purely as a quantum device. By doing detailed study comparing between the diamond quantum annealer, and D-Wave’s quantum annealer, it will be possible to settle the long, vigorous debate about how ‘quantum’ the D-Wave device. The major roadblock in the way of studying this important question has been the existence of another adiabatic quantum processor that did not operate at such cold temperatures, and which had a

qubit connectivity graph that was suited to the annealing problem.

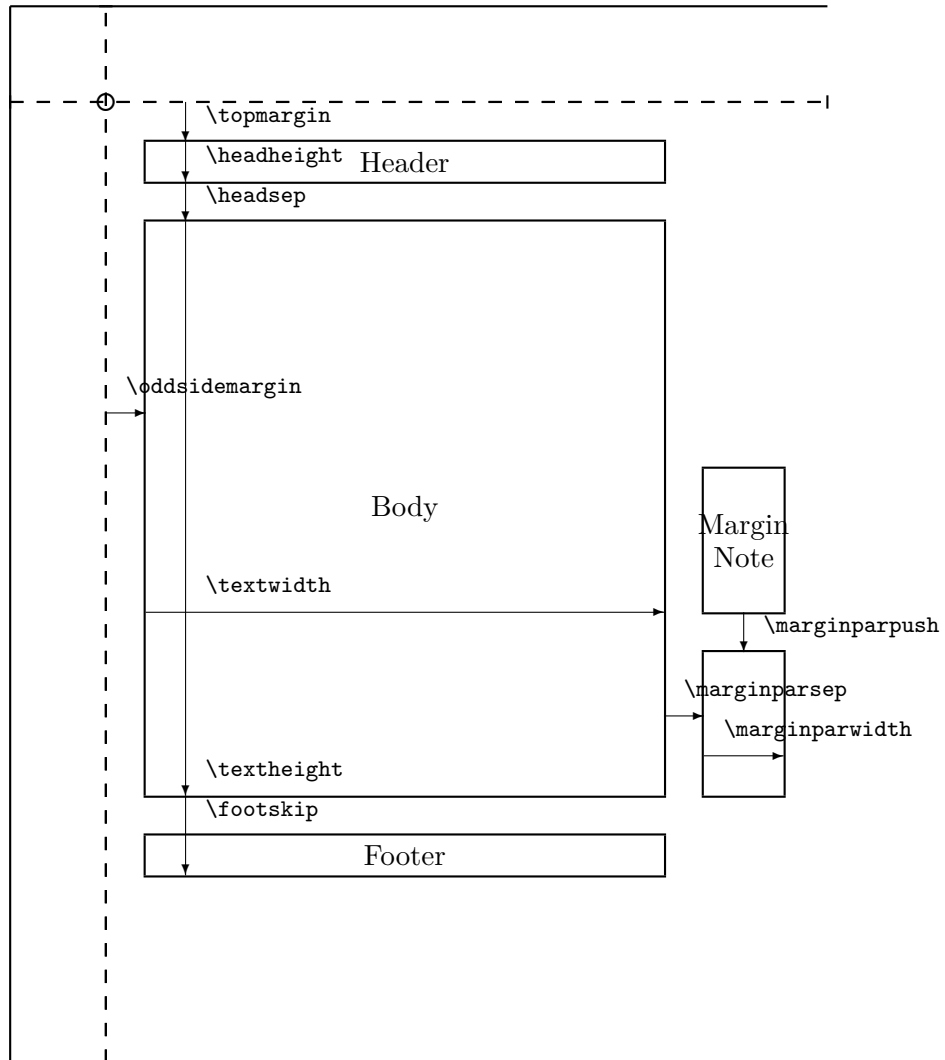
Here are the parameters for the page layout. If you modify the template, do not decrease: the font size, the line spacing (1.5), the margin size.

Actual page layout values.

\paperheight = 296.9965mm	\paperwidth = 209.99753mm
\hoffset = 0mm	\voffset = 0mm
\evensidemargin = 0mm	\oddsidemargin = 14.59982mm
\topmargin = -2.99995mm	\headheight = 10.54367mm
\headsep = 7.02911mm	\textheight = 219.9974mm
\textwidth = 144.5983mm	\footskip = 9.65201mm
\marginparsep = 2.46019mm	\marginparpush = 1.75728mm
\columnsep = 3.51456mm	\columnseprule = 0mm
1em = 3.84843mm	1ex = 1.65694mm

\marginparwidth: 24.9997mm

The circle is at 1 inch from the top and left of the page. Dashed lines represent (`\hoffset + 1 inch`) and (`\voffset + 1 inch`) from the top and left of the page.



---

# Bibliography

---

- [1] Charles Babbage. *Passages from the Life of a Philosopher*. Good Press, 2019.
- [2] Peter W. Shor. Polynomial-Time Algorithms for Prime Factorization and Discrete Logarithms on a Quantum Computer. *SIAM Journal on Computing*, 26(5):1484–1509, October 1997. ISSN 0097-5397. doi: 10.1137/S0097539795293172. URL <https://pubs.siam.org/doi/10.1137/S0097539795293172>. Publisher: Society for Industrial and Applied Mathematics.
- [3] J Atalla and D Kahng. Metal oxide semiconductor (MOS) transistors demonstrated. The Silicon Engine. *Computer History Museum*, 1960.
- [4] Gordon E Moore and others. Cramming more components onto integrated circuits, 1965.
- [5] Richard H Stulen and Donald W Sweeney. Extreme ultraviolet lithography. *IEEE journal of quantum electronics*, 35(5):694–699, 1999. Publisher: IEEE.
- [6] Ramish Zafar. Apple A13 & Beyond: How Transistor Count And Costs Will Go Up, April 2019. URL <https://wccftech.com/apple-5nm-3nm-cost-transistors/>.
- [7] Muhammad Fahad, Arsalan Shahid, Ravi Manumachu, and Alexey Lastovetsky. Accurate Energy Modelling of Hybrid Parallel Applications on Modern Heterogeneous Computing Platforms Using System-Level Measurements. *IEEE Access*, 8:93793 – 93829, May 2020. doi: 10.1109/ACCESS.2020.2994953.
- [8] John Preskill. Quantum Computing in the NISQ era and beyond. *Quantum*, 2:79, August 2018. doi: 10.22331/q-2018-08-06-79. URL <https://quantum-journal.org/papers/q-2018-08-06-79/>. Publisher: Verein zur Förderung des Open Access Publizierens in den Quantenwissenschaften.
- [9] Frank Arute, Kunal Arya, Ryan Babbush, Dave Bacon, Joseph C. Bardin, Rami Barends, Rupak Biswas, Sergio Boixo, Fernando G. S. L. Bradao, David A. Buell, Brian Burkett, Yu Chen, Zijun Chen, Ben Chiaro, Roberto Collins, William Courtney, Andrew Dunsworth, Edward Farhi, Brooks Foxen, Austin Fowler, Craig Gidney, Marissa Giustina, Rob Graff, Keith Guerin, Steve Habegger, Matthew P. Harrigan, Michael J. Hartmann, Alan Ho, Markus Hoffmann, Trent Huang, Travis S. Humble, Sergei V. Isakov, Evan Jeffrey, Zhang Jiang, Dvir Kafri, Kostyantyn Kechedzhi, Julian Kelly, Paul V. Klimov, Sergey Knysh, Alexander Korotkov, Fedor Kostritsa, David Landhuis, Mike Lindmark, Erik Lucero, Dmitry Lyakh, Salvatore Mandrà, Jarrod R. McClean, Matthew McEwen, Anthony Megrant, Xiao Mi, Kristel Michelsen, Masoud Mohseni, Josh Mutus, Ofer Naaman, Matthew Neeley, Charles Neill, Murphy Yuezhen Niu, Eric Ostby, Andre Petukhov, John C. Platt, Chris Quintana, Eleanor G. Rieffel, Pedram Roushan, Nicholas C. Rubin, Daniel Sank, Kevin J. Satzinger, Vadim Smelyanskiy, Kevin J. Sung, Matthew D. Trevithick, Amit Vainsencher, Benjamin Villalonga, Theodore White, Z. Jamie Yao, Ping Yeh, Adam Zalcman, Hartmut Neven, and John M. Martinis. Quantum supremacy using a programmable superconducting processor. *Nature*, 574(7779):505–510, October 2019. ISSN 1476-4687. doi: 10.1038/s41586-019-1666-5.

- URL <https://www.nature.com/articles/s41586-019-1666-5>. Bandiera\_abtest: a Cg\_type: Nature Research Journals Number: 7779 Primary\_atype: Research Publisher: Nature Publishing Group Subject\_term: Quantum information;Quantum physics Subject\_term\_id: quantum-information;quantum-physics.
- [10] John Chiaverini, Dietrich Leibfried, Tobias Schaetz, Murray D Barrett, RB Blakestad, Joseph Britton, Wayne M Itano, John D Jost, Emanuel Knill, Christopher Langer, and others. Realization of quantum error correction. *Nature*, 432(7017):602–605, 2004. Publisher: Nature Publishing Group.
  - [11] Daniel A Lidar and Todd A Brun. *Quantum error correction*. Cambridge university press, 2013.
  - [12] Vittorio Giovannetti, Seth Lloyd, and Lorenzo Maccone. Quantum Random Access Memory. *Physical Review Letters*, 100(16):160501, April 2008. doi: 10.1103/PhysRevLett.100.160501. URL <https://link.aps.org/doi/10.1103/PhysRevLett.100.160501>. Publisher: American Physical Society.
  - [13] Wolfgang Lechner, Philipp Hauke, and Peter Zoller. A quantum annealing architecture with all-to-all connectivity from local interactions. *Science advances*, 1(9):e1500838–e1500838, October 2015. ISSN 2375-2548. doi: 10.1126/sciadv.1500838. URL <https://pubmed.ncbi.nlm.nih.gov/26601316>. Publisher: American Association for the Advancement of Science.
  - [14] Michael A. Nielsen and Isaac L. Chuang. *Quantum Computation and Quantum Information: 10th Anniversary Edition*. Cambridge University Press, Cambridge, 2010. ISBN 978-1-107-00217-3. doi: 10.1017/CBO9780511976667. URL <https://www.cambridge.org/core/books/quantum-computation-and-quantum-information/01E10196D0A682A6AEFFEA52D53BE9AE>.
  - [15] Alexey Uvarov and Jacob Biamonte. On barren plateaus and cost function locality in variational quantum algorithms. *arXiv:2011.10530 [cond-mat, physics:quant-ph]*, November 2020. URL <http://arxiv.org/abs/2011.10530>. arXiv: 2011.10530.
  - [16] Lennart Bittel and Martin Kliesch. Training Variational Quantum Algorithms Is NP-Hard. *Physical Review Letters*, 127(12):120502, September 2021. doi: 10.1103/PhysRevLett.127.120502. URL <https://link.aps.org/doi/10.1103/PhysRevLett.127.120502>. Publisher: American Physical Society.
  - [17] Tameem Albash and Daniel A. Lidar. Adiabatic quantum computation. *Reviews of Modern Physics*, 90(1):015002, January 2018. doi: 10.1103/RevModPhys.90.015002. URL <https://link.aps.org/doi/10.1103/RevModPhys.90.015002>. Publisher: American Physical Society.
  - [18] M. H. S. Amin, Dmitri V. Averin, and James A. Nesteroff. Decoherence in adiabatic quantum computation. *Physical Review A*, 79(2):022107, February 2009. ISSN 1050-2947, 1094-1622. doi: 10.1103/PhysRevA.79.022107. URL <http://arxiv.org/abs/0708.0384>. arXiv: 0708.0384.
  - [19] M. H. S. Amin, C. J. S. Truncik, and D. V. Averin. Role of Single Qubit Decoherence Time in Adiabatic Quantum Computation. *Physical Review A*, 80(2):022303, August 2009. ISSN 1050-2947, 1094-1622. doi: 10.1103/PhysRevA.80.022303. URL <http://arxiv.org/abs/0803.1196>. arXiv: 0803.1196.
  - [20] Kamran Karimi, Neil G. Dickson, Firas Hamze, M. H. S. Amin, Marshall Drew-Brook, Fabian A. Chudak, Paul I. Bunyk, William G. Macready, and Geordie Rose. Investigating the Performance

- 
- of an Adiabatic Quantum Optimization Processor. *arXiv:1006.4147 [cond-mat, physics:quant-ph]*, January 2011. URL <http://arxiv.org/abs/1006.4147>. arXiv: 1006.4147.
- [21] Adrian Cho. Quantum or not, controversial computer yields no speedup. *Science*, 344(6190):1330–1331, June 2014. ISSN 0036-8075, 1095-9203. doi: 10.1126/science.344.6190.1330. URL <https://science.sciencemag.org/content/344/6190/1330>. Publisher: American Association for the Advancement of Science Section: In Depth.
  - [22] Salvatore Mandrà and Helmut G Katzgraber. A deceptive step towards quantum speedup detection. *Quantum Science and Technology*, 3(4):04LT01, July 2018. ISSN 2058-9565. doi: 10.1088/2058-9565/aac8b2. URL <https://iopscience.iop.org/article/10.1088/2058-9565/aac8b2>.
  - [23] Helmut G. Katzgraber, Firas Hamze, Zheng Zhu, Andrew J. Ochoa, and H. Munoz-Bauza. Seeking Quantum Speedup Through Spin Glasses: The Good, the Bad, and the Ugly. *Physical Review X*, 5(3):031026, September 2015. doi: 10.1103/PhysRevX.5.031026. URL <https://link.aps.org/doi/10.1103/PhysRevX.5.031026>. Publisher: American Physical Society.
  - [24] T. Albash, T.F. Rønnow, M. Troyer, and D.A. Lidar. Reexamining classical and quantum models for the D-Wave One processor. *The European Physical Journal Special Topics*, 224(1):111–129, February 2015. ISSN 1951-6401. doi: 10.1140/epjst/e2015-02346-0. URL <https://doi.org/10.1140/epjst/e2015-02346-0>.
  - [25] Stephen P. Jordan, David Gosset, and Peter J. Love. Quantum-Merlin-Arthur-complete problems for stoquastic Hamiltonians and Markov matrices. *Physical Review A*, 81(3):032331, March 2010. doi: 10.1103/PhysRevA.81.032331. URL <https://link.aps.org/doi/10.1103/PhysRevA.81.032331>. Publisher: American Physical Society.
  - [26] Gopalakrishnan Balasubramanian, Philipp Neumann, Daniel Twitchen, Matthew Markham, Roman Kolesov, Norikazu Mizuuchi, Junichi Isoya, Jocelyn Achard, Johannes Beck, Julia Tissler, Vincent Jacques, Philip R. Hemmer, Fedor Jelezko, and Jörg Wrachtrup. Ultralong spin coherence time in isotopically engineered diamond. *Nature Materials*, 8(5):383–387, May 2009. ISSN 1476-4660. doi: 10.1038/nmat2420. URL <https://www.nature.com/articles/nmat2420>. Bandiera\_abtest: a Cg\_type: Nature Research Journals Number: 5 Primary\_atype: Research Publisher: Nature Publishing Group.
  - [27] Guido Burkard, Roger H Koch, and David P DiVincenzo. Multilevel quantum description of decoherence in superconducting qubits. *Physical Review B*, 69(6):064503, 2004. Publisher: APS.
  - [28] Michael A Nielsen and Isaac L Chuang. *Quantum Computation and Quantum Information*.
  - [29] László Lovász. Graph minor theory. *Bulletin of the American Mathematical Society*, 43(1):75–86, 2006. ISSN 0273-0979, 1088-9485. doi: 10.1090/S0273-0979-05-01088-8. URL <https://www.ams.org/bull/2006-43-01/S0273-0979-05-01088-8/>.
  - [30] Jun Cai, William Macready, and Aidan Roy. A practical heuristic for finding graph minors. June 2014.
  - [31] A. Yu Kitaev. Quantum computations: algorithms and error correction. *Russian Mathematical Surveys*, 52(6):1191, December 1997. ISSN 0036-0279. doi: 10.1070/RM1997v052n06ABEH002155. URL <https://iopscience.iop.org/article/10.1070/RM1997v052n06ABEH002155/meta>. Publisher: IOP Publishing.

- [32] Christopher M. Dawson and Michael A. Nielsen. The Solovay-Kitaev algorithm. *Quantum Information & Computation*, 6(1):81–95, January 2006. ISSN 1533-7146.
- [33] Martin Plesch and Časlav Brukner. Quantum-state preparation with universal gate decompositions. *Physical Review A*, 83(3):032302, March 2011. doi: 10.1103/PhysRevA.83.032302. URL <https://link.aps.org/doi/10.1103/PhysRevA.83.032302>. Publisher: American Physical Society.
- [34] Ville Bergholm, Juha J. Vartiainen, Mikko Möttönen, and Martti M. Salomaa. Quantum circuits with uniformly controlled one-qubit gates. *Physical Review A*, 71(5):052330, May 2005. doi: 10.1103/PhysRevA.71.052330. URL <https://link.aps.org/doi/10.1103/PhysRevA.71.052330>. Publisher: American Physical Society.
- [35] Gavin E. Crooks. Gradients of parameterized quantum gates using the parameter-shift rule and gate decomposition. *arXiv:1905.13311 [quant-ph]*, May 2019. URL <http://arxiv.org/abs/1905.13311>. arXiv: 1905.13311.
- [36] Mateusz Ostaszewski, Edward Grant, and Marcello Benedetti. Structure optimization for parameterized quantum circuits. *Quantum*, 5:391, January 2021. doi: 10.22331/q-2021-01-28-391. URL <https://quantum-journal.org/papers/q-2021-01-28-391/>. Publisher: Verein zur Förderung des Open Access Publizierens in den Quantenwissenschaften.
- [37] Tosio Kato. On the Adiabatic Theorem of Quantum Mechanics. *Journal of the Physical Society of Japan*, 5(6):435–439, November 1950. ISSN 0031-9015. doi: 10.1143/JPSJ.5.435. URL <https://journals.jps.jp/doi/10.1143/JPSJ.5.435>. Publisher: The Physical Society of Japan.
- [38] Mohammad Amin. Consistency of the Adiabatic Theorem. *Physical review letters*, 102:220401, July 2009. doi: 10.1103/PhysRevLett.102.220401.
- [39] Dorit Aharonov, Wim Van Dam, Julia Kempe, Zeph Landau, Seth Lloyd, and Oded Regev. Adiabatic quantum computation is equivalent to standard quantum computation. *SIAM review*, 50(4):755–787, 2008. Publisher: SIAM.
- [40] Jérémie Roland and Nicolas J. Cerf. Quantum search by local adiabatic evolution. *Physical Review A*, 65(4):042308, March 2002. doi: 10.1103/PhysRevA.65.042308. URL <https://link.aps.org/doi/10.1103/PhysRevA.65.042308>. Publisher: American Physical Society.
- [41] Sergey Bravyi, David P. Divincenzo, Roberto Oliveira, and Barbara M. Terhal. The complexity of stoquastic local Hamiltonian problems. *Quantum Information & Computation*, 8(5):361–385, May 2008. ISSN 1533-7146.
- [42] K. H. Hoffmann and P. Salamon. The optimal simulated annealing schedule for a simple model. 23(15):3511–3523, August 1990. ISSN 0305-4470. doi: 10.1088/0305-4470/23/15/023. URL <https://doi.org/10.1088/0305-4470/23/15/023>. Publisher: IOP Publishing.
- [43] Satoshi Morita. Faster Annealing Schedules for Quantum Annealing. 2007. doi: 10.1143/JPSJ.76.104001.
- [44] Satoshi Morita and Hidetoshi Nishimori. Mathematical foundation of quantum annealing: Journal of Mathematical Physics: Vol 49, No 12, July 2008. URL [https://aip.scitation.org/doi/full/10.1063/1.2995837?casa\\_token=GtShVS0kYwEAAAAA%3ATH8hGv0wZie0j3vJ6znI2Ekfy0xuhzNMfPVqh8Gocd7u7X1q1qpUqsH\\_0eJk2QLmFEIWv9nzQA](https://aip.scitation.org/doi/full/10.1063/1.2995837?casa_token=GtShVS0kYwEAAAAA%3ATH8hGv0wZie0j3vJ6znI2Ekfy0xuhzNMfPVqh8Gocd7u7X1q1qpUqsH_0eJk2QLmFEIWv9nzQA).

- [45] Sudip Mukherjee and Bikas K Chakrabarti. Multivariable optimization: Quantum annealing and computation. *The European Physical Journal Special Topics*, 224(1):17–24, 2015. Publisher: Springer.
- [46] Arnab Das, Bikas K Chakrabarti, and Robin B Stinchcombe. Quantum annealing in a kinetically constrained system. *Physical Review E*, 72(2):026701, 2005. Publisher: APS.
- [47] Lishan Zeng, Jun Zhang, and Mohan Sarovar. Schedule path optimization for adiabatic quantum computing and optimization. 49(16):165305, March 2016. ISSN 1751-8121. doi: 10.1088/1751-8113/49/16/165305. URL <https://doi.org/10.1088/1751-8113/49/16/165305>. Publisher: IOP Publishing.
- [48] Gary Kochenberger, Jin-Kao Hao, Fred Glover, Mark Lewis, Zhipeng Lü, Haibo Wang, and Yang Wang. The unconstrained binary quadratic programming problem: a survey. *Journal of Combinatorial Optimization*, 28(1):58–81, July 2014. ISSN 1573-2886. doi: 10.1007/s10878-014-9734-0. URL <https://doi.org/10.1007/s10878-014-9734-0>.
- [49] Seung Woo Shin, Graeme Smith, John A. Smolin, and Umesh Vazirani. How "Quantum" is the D-Wave Machine?, 2014. eprint: 1401.7087.
- [50] Rolando D. Somma, Daniel Nagaj, and Mária Kieferová. Quantum Speedup by Quantum Annealing. *Physical Review Letters*, 109(5):050501, July 2012. doi: 10.1103/PhysRevLett.109.050501. URL <https://link.aps.org/doi/10.1103/PhysRevLett.109.050501>. Publisher: American Physical Society.
- [51] Tommaso Zanca and Giuseppe E Santoro. Quantum annealing speedup over simulated annealing on random Ising chains. *Physical Review B*, 93(22):224431, 2016. Publisher: APS.
- [52] Elizabeth Crosson and Aram W. Harrow. Simulated Quantum Annealing Can Be Exponentially Faster Than Classical Simulated Annealing. In *2016 IEEE 57th Annual Symposium on Foundations of Computer Science (FOCS)*, pages 714–723, October 2016. doi: 10.1109/FOCS.2016.81. ISSN: 0272-5428.
- [53] Vasil S. Denchev, Sergio Boixo, Sergei V. Isakov, Nan Ding, Ryan Babbush, Vadim Smelyanskiy, John Martinis, and Hartmut Neven. What is the Computational Value of Finite-Range Tunneling? *Phys. Rev. X*, 6(3):031015, August 2016. doi: 10.1103/PhysRevX.6.031015. URL <https://link.aps.org/doi/10.1103/PhysRevX.6.031015>. Publisher: American Physical Society.
- [54] J. E. Field, editor. *The Properties of diamond*. Academic Press, London ; New York, 1979. ISBN 978-0-12-255350-9.
- [55] Karl E Spear and John P Dismukes. *Synthetic diamond: emerging CVD science and technology*, volume 25. John Wiley & Sons, 1994.
- [56] E. van Oort, N. B. Manson, and M. Glasbeek. Optically detected spin coherence of the diamond N-V centre in its triplet ground state. *Journal of Physics C: Solid State Physics*, 21(23):4385–4391, August 1988. ISSN 0022-3719. doi: 10.1088/0022-3719/21/23/020. URL <https://doi.org/10.1088/0022-3719/21/23/020>. Publisher: IOP Publishing.
- [57] G. Davies, M. F. Hamer, and William Charles Price. Optical studies of the 1.945 eV vibronic band in diamond. *Proceedings of the Royal Society of London. A. Mathematical and Physical Sciences*, 348(1653):285–298, February 1976. doi: 10.1098/rspa.1976.0039. URL <https://royalsocietypublishing.org/doi/10.1098/rspa.1976.0039>. Publisher: Royal Society.

- [58] A. Gruber, A. Dräbenstedt, C. Tietz, L. Fleury, J. Wrachtrup, and C. von Borczyskowski. Scanning Confocal Optical Microscopy and Magnetic Resonance on Single Defect Centers. *Science*, 276(5321):2012–2014, June 1997. doi: 10.1126/science.276.5321.2012. URL <https://www.science.org/doi/abs/10.1126/science.276.5321.2012>. Publisher: American Association for the Advancement of Science.
- [59] T. H. Taminiau, J. Cramer, T. van der Sar, V. V. Dobrovitski, and R. Hanson. Universal control and error correction in multi-qubit spin registers in diamond. *Nature Nanotechnology*, 9(3):171–176, March 2014. ISSN 1748-3395. doi: 10.1038/nnano.2014.2. URL <https://www.nature.com/articles/nnano.2014.2>. Bandiera\_abtest: a Cg\_type: Nature Research Journals Number: 3 Primary\_atype: Research Publisher: Nature Publishing Group Subject\_term: Qubits Subject\_term\_id: qubits.
- [60] G. Waldherr, Y. Wang, S. Zaiser, M. Jamali, T. Schulte-Herbrüggen, H. Abe, T. Ohshima, J. Isoya, J. F. Du, P. Neumann, and J. Wrachtrup. Quantum error correction in a solid-state hybrid spin register. *Nature*, 506(7487):204–207, February 2014. ISSN 1476-4687. doi: 10.1038/nature12919. URL <https://www.nature.com/articles/nature12919>. Bandiera\_abtest: a Cg\_type: Nature Research Journals Number: 7487 Primary\_atype: Research Publisher: Nature Publishing Group Subject\_term: Quantum information Subject\_term\_id: quantum-information.
- [61] Matthew W Dale and Gavin W Morley. Medical applications of diamond magnetometry: commercial viability. *arXiv preprint arXiv:1705.01994*, 2017.
- [62] D DiFrancesco\*. Advances in geophysical exploration: Sensors and platforms. In *International Workshop on Gravity, Electrical & Magnetic Methods and Their Applications, Xi'an, China, May 19–22, 2019*, pages 9–12. Society of Exploration Geophysicists and Chinese Geophysical Society, 2019.
- [63] CL Degen. Scanning magnetic field microscope with a diamond single-spin sensor. *Applied Physics Letters*, 92(24):243111, 2008. Publisher: American Institute of Physics.
- [64] JM Taylor, Paola Cappellaro, L Childress, Liang Jiang, Dmitry Budker, PR Hemmer, Amir Yacoby, R Walsworth, and MD Lukin. High-sensitivity diamond magnetometer with nanoscale resolution. *Nature Physics*, 4(10):810–816, 2008. Publisher: Nature Publishing Group.
- [65] Florian Dolde, Helmut Fedder, Marcus W Doherty, Tobias Nöbauer, Florian Rempp, Gopalakrishnan Balasubramanian, Thomas Wolf, Friedemann Reinhard, Lloyd CL Hollenberg, Fedor Jelezko, and others. Electric-field sensing using single diamond spins. *Nature Physics*, 7(6):459–463, 2011. Publisher: Nature Publishing Group.
- [66] Jeronimo R Maze, Paul L Stanwix, James S Hodges, Seungpyo Hong, Jacob M Taylor, Paola Cappellaro, Liang Jiang, MV Gurudev Dutt, Emre Togan, AS Zibrov, and others. Nanoscale magnetic sensing with an individual electronic spin in diamond. *Nature*, 455(7213):644–647, 2008. Publisher: Nature Publishing Group.
- [67] Gopalakrishnan Balasubramanian, IY Chan, Roman Kolesov, Mohannad Al-Hmoud, Julia Tisler, Chang Shin, Changdong Kim, Aleksander Wojcik, Philip R Hemmer, Anke Krueger, and others. Nanoscale imaging magnetometry with diamond spins under ambient conditions. *Nature*, 455(7213):648–651, 2008. Publisher: Nature Publishing Group.

- 
- [68] JR Rabeau, Patrick Reichart, Grigori Tamanyan, DN Jamieson, Steven Prawer, Fedor Jelezko, Torsten Gaebel, Iulian Popa, Michael Domhan, and J Wrachtrup. Implantation of labelled single nitrogen vacancy centers in diamond using N 15. *Applied Physics Letters*, 88(2):023113, 2006. Publisher: American Institute of Physics.
  - [69] Marcus W. Doherty, Neil B. Manson, Paul Delaney, Fedor Jelezko, Jörg Wrachtrup, and Lloyd C. L. Hollenberg. The nitrogen-vacancy colour centre in diamond. *Physics Reports*, 528(1):1–45, July 2013. ISSN 0370-1573. doi: 10.1016/j.physrep.2013.02.001. URL <https://www.sciencedirect.com/science/article/pii/S0370157313000562>.
  - [70] E. D. Herbschleb, H. Kato, Y. Maruyama, T. Danjo, T. Makino, S. Yamasaki, I. Ohki, K. Hayashi, H. Morishita, M. Fujiwara, and N. Mizuochi. Ultra-long coherence times amongst room-temperature solid-state spins. *Nature Communications*, 10(1):3766, August 2019. ISSN 2041-1723. doi: 10.1038/s41467-019-11776-8. URL <https://www.nature.com/articles/s41467-019-11776-8>. Bandiera\_abtest: a Cc\_license\_type: cc\_by Cg\_type: Nature Research Journals Number: 1 Primary\_atype: Research Publisher: Nature Publishing Group Subject\_term: Quantum information;Qubits;Sensors;Sensors and biosensors Subject\_term\_id: quantum-information;qubits;sensors;sensors-and-biosensors.
  - [71] Jun John Sakurai and Eugene D Commins. Modern quantum mechanics, revised edition, 1995.
  - [72] J. Martin, R. Wannemacher, J. Teichert, L. Bischoff, and B. Köhler. Generation and detection of fluorescent color centers in diamond with submicron resolution. *Applied Physics Letters*, 75(20):3096–3098, November 1999. ISSN 0003-6951. doi: 10.1063/1.125242. URL <https://aip.scitation.org/doi/10.1063/1.125242>. Publisher: American Institute of Physics.
  - [73] Pavel G. Baranov, Alexandra A. Soltamova, Daniel O. Tolmachev, Nikolay G. Romanov, Roman A. Babunts, Fedor M. Shakhov, Sergey V. Kidalov, Alexandr Y. Vul’, Georgy V. Mamin, Sergei B. Orlinskii, and Nikolai I. Silkin. Enormously High Concentrations of Fluorescent Nitrogen-Vacancy Centers Fabricated by Sintering of Detonation Nanodiamonds. *Small*, 7(11):1533–1537, 2011. ISSN 1613-6829. doi: 10.1002/smll.201001887. URL [https://onlinelibrary.wiley.com/doi/abs/10.1002/smll.201001887.\\_eprint](https://onlinelibrary.wiley.com/doi/abs/10.1002/smll.201001887._eprint): <https://onlinelibrary.wiley.com/doi/pdf/10.1002/smll.201001887>.
  - [74] Long-Jyun Su, Chia-Yi Fang, Yu-Tang Chang, Kuan-Ming Chen, Yueh-Chung Yu, Jui-Hung Hsu, and Huan-Cheng Chang. Creation of high density ensembles of nitrogen-vacancy centers in nitrogen-rich type Ib nanodiamonds. *Nanotechnology*, 24(31):315702, July 2013. ISSN 0957-4484. doi: 10.1088/0957-4484/24/31/315702. URL <https://doi.org/10.1088/0957-4484/24/31/315702>. Publisher: IOP Publishing.
  - [75] J. Meijer, B. Burchard, M. Domhan, C. Wittmann, T. Gaebel, I. Popa, F. Jelezko, and J. Wrachtrup. Generation of single color centers by focused nitrogen implantation. *Applied Physics Letters*, 87(26):261909, December 2005. ISSN 0003-6951. doi: 10.1063/1.2103389. URL <https://aip.scitation.org/doi/10.1063/1.2103389>. Publisher: American Institute of Physics.
  - [76] Janine Riedrich-Möller, Sébastien Pezzagna, Jan Meijer, Christoph Pauly, Frank Mücklich, Matthew Markham, Andrew M Edmonds, and Christoph Becher. Nanoimplantation and Purcell enhancement of single nitrogen-vacancy centers in photonic crystal cavities in diamond. *Applied Physics Letters*, 106(22):221103, 2015. Publisher: AIP Publishing LLC.

- [77] P Spinicelli, A Dréau, L Rondin, F Silva, J Achard, S Xavier, S Bansropun, T Debuisschert, S Pezzagna, J Meijer, and others. Engineered arrays of nitrogen-vacancy color centers in diamond based on implantation of CN<sup>-</sup> molecules through nanoapertures. *New Journal of Physics*, 13(2):025014, 2011. Publisher: IOP Publishing.
- [78] Kenichi Ohno, F. Joseph Heremans, Lee C. Bassett, Bryan A. Myers, David M. Toyli, Ania C. Bleszynski Jayich, Christopher J. Palmstrøm, and David D. Awschalom. Engineering shallow spins in diamond with nitrogen delta-doping. *Applied Physics Letters*, 101:082413, August 2012. ISSN 0003-6951. doi: 10.1063/1.4748280. URL <https://ui.adsabs.harvard.edu/abs/2012ApPhL.101h2413O>. ADS Bibcode: 2012ApPhL.101h2413O.
- [79] Tzach Jaffe, Mohammed Attrash, Mohan Kumar Kuntumalla, Roza Akhvlediani, Shaul Michaelson, Lior Gal, Nina Felgen, Miri Fischer, Johann Peter Reithmaier, Cyril Popov, Alon Hoffman, and Meir Orenstein. Novel Ultra Localized and Dense Nitrogen Delta-Doping in Diamond for Advanced Quantum Sensing. *Nano Letters*, 20(5):3192–3198, May 2020. ISSN 1530-6984. doi: 10.1021/acs.nanolett.9b05243. URL <https://doi.org/10.1021/acs.nanolett.9b05243>. Publisher: American Chemical Society.
- [80] Stephen Shankland. IBM's 35 atoms and the rise of nanotech. URL <https://www.cnet.com/news/ibms-35-atoms-and-the-rise-of-nanotech/>.
- [81] Kate Smith-Miles, Davaatseren Baatar, Brendan Wreford, and Rhŷd Lewis. Towards objective measures of algorithm performance across instance space. *Computers & Operations Research*, 45:12–24, May 2014. ISSN 0305-0548. doi: 10.1016/j.cor.2013.11.015. URL <https://www.sciencedirect.com/science/article/pii/S0305054813003389>.
- [82] Rasmus Bro and Age K Smilde. Principal component analysis. *Analytical methods*, 6(9):2812–2831, 2014. Publisher: Royal Society of Chemistry.
- [83] Bernhard E Boser, Isabelle M Guyon, and Vladimir N Vapnik. A training algorithm for optimal margin classifiers. In *Proceedings of the fifth annual workshop on Computational learning theory*, pages 144–152, 1992.
- [84] Silvia S. Hidalgo-Tobón. Theory of gradient coil design methods for magnetic resonance imaging. *Concepts in Magnetic Resonance Part A*, 36:223–242, 2010.
- [85] Nikhil Bansal, Sergey Bravyi, and Barbara Terhal. Classical approximation schemes for the ground-state energy of quantum and classical Ising spin Hamiltonians on planar graphs. *Quant Info Comput*, 9, May 2007. doi: 10.26421/QIC9.7-8-12.
- [86] Klaus Wagner. Über eine Eigenschaft der ebenen Komplexe. *Mathematische Annalen*, 114(1):570–590, 1937. Publisher: Springer.
- [87] Mario S Könz, Wolfgang Lechner, Helmut G Katzgraber, and Matthias Troyer. Scaling overhead of embedding optimization problems in quantum annealing. *arXiv preprint arXiv:2103.15991*, 2021.
- [88] Mark W Johnson, Mohammad HS Amin, Suzanne Gildert, Trevor Lanting, Firas Hamze, Neil Dickson, Richard Harris, Andrew J Berkley, Jan Johansson, Paul Bunyk, and others. Quantum annealing with manufactured spins. *Nature*, 473(7346):194–198, 2011. Publisher: Nature Publishing Group.

- [89] Hiroki Oshiyama, Sei Suzuki, and Naokazu Shibata. Classical simulation and theory of quantum annealing in a thermal environment, 2021. *\_eprint:* 2102.02570.
- [90] Victor Bapst and Guilhem Semerjian. Thermal, quantum and simulated quantum annealing: Analytical comparisons for simple models. In *Journal of Physics: Conference Series*, volume 473, page 012011. IOP Publishing, 2013. Issue: 1.
- [91] Giorgio Ausiello, Pierluigi Crescenzi, Giorgio Gambosi, Viggo Kann, Alberto Marchetti-Spaccamela, and Marco Protasi. *Complexity and approximation: Combinatorial optimization problems and their approximability properties*. Springer Science & Business Media, 2012.
- [92] Christos H. Papadimitriou and Mihalis Yannakakis. Optimization, approximation, and complexity classes. *Journal of Computer and System Sciences*, 43(3):425–440, 1991. ISSN 0022-0000. doi: [https://doi.org/10.1016/0022-0000\(91\)90023-X](https://doi.org/10.1016/0022-0000(91)90023-X). URL <https://www.sciencedirect.com/science/article/pii/002200009190023X>.
- [93] Charles Moussa, Henri Calandra, and Vedran Dunjko. To quantum or not to quantum: towards algorithm selection in near-term quantum optimization. 5(4):044009, October 2020. ISSN 2058-9565. doi: 10.1088/2058-9565/abb8e5. URL <https://doi.org/10.1088/2058-9565/abb8e5>. Publisher: IOP Publishing.
- [94] Matthew P. Harrigan, Kevin J. Sung, Matthew Neeley, Kevin J. Satzinger, Frank Arute, Kunal Arya, Juan Atalaya, Joseph C. Bardin, Rami Barends, Sergio Boixo, Michael Broughton, Bob B. Buckley, David A. Buell, Brian Burkett, Nicholas Bushnell, Yu Chen, Zijun Chen, Ben Chiaro, Roberto Collins, William Courtney, Sean Demura, Andrew Dunsworth, Daniel Eppens, Austin Fowler, Brooks Foxen, Craig Gidney, Marissa Giustina, Rob Graff, Steve Habegger, Alan Ho, Sabrina Hong, Trent Huang, L. B. Ioffe, Sergei V. Isakov, Evan Jeffrey, Zhang Jiang, Cody Jones, Dvir Kafri, Kostyantyn Kechedzhi, Julian Kelly, Seon Kim, Paul V. Klimov, Alexander N. Korotkov, Fedor Kostritsa, David Landhuis, Pavel Laptev, Mike Lindmark, Martin Leib, Orion Martin, John M. Martinis, Jarrod R. McClean, Matt McEwen, Anthony Megrant, Xiao Mi, Masoud Mohseni, Wojciech Mruczkiewicz, Josh Mutus, Ofer Naaman, Charles Neill, Florian Neukart, Murphy Yuezhen Niu, Thomas E. O’Brien, Bryan O’Gorman, Eric Ostby, Andre Petukhov, Harald Putterman, Chris Quintana, Pedram Roushan, Nicholas C. Rubin, Daniel Sank, Andrea Skolik, Vadim Smelyanskiy, Doug Strain, Michael Streif, Marco Szalay, Amit Vainsencher, Theodore White, Z. Jamie Yao, Ping Yeh, Adam Zalcman, Leo Zhou, Hartmut Neven, Dave Bacon, Erik Lucero, Edward Farhi, and Ryan Babbush. Quantum approximate optimization of non-planar graph problems on a planar superconducting processor. *Nature Physics*, 17(3):332–336, March 2021. ISSN 1745-2481. doi: 10.1038/s41567-020-01105-y. URL <https://www.nature.com/articles/s41567-020-01105-y>. Bandiera\_abtest: a Cg\_type: Nature Research Journals Number: 3 Primary\_atype: Research Publisher: Nature Publishing Group Subject\_term: Computational science;Quantum information Subject\_term\_id: computational-science;quantum-information.
- [95] Milan Leonard. Optimization of Variational Hybrid Quantum-Classical Circuits for Noisy Intermediate-Scale Quantum Devices. October 2020.
- [96] Damian S. Steiger, Bettina Heim, Troels F. Rønnow, and Matthias Troyer. Performance of quantum annealing hardware. In *Electro-Optical and Infrared Systems: Technology and Applications XII; and Quantum Information Science and Technology*, volume 9648, page 964816. International Society for Optics and Photonics, October 2015. doi: 10.1117/

- 12.2202661. URL <https://www.spiedigitallibrary.org/conference-proceedings-of-spie/9648/964816/Performance-of-quantum-annealing-hardware/10.1117/12.2202661.short>.
- [97] Fanella McAndrew. Adiabatic Quantum Computing to solve the MaxCut graph problem. *The University of Melbourne School of Mathematics and Statistics*, 2020. URL <https://matilda.unimelb.edu.au/matilda/matildadata/maxcut/downloads/Adiabatic-Quantum-Computing-to-solve-the-MaxCut-graph-problem.pdf>.
- [98] Adam Pearson, Anurag Mishra, Itay Hen, and Daniel A. Lidar. Analog errors in quantum annealing: doom and hope. *npj Quantum Information*, 5(1):1–9, November 2019. ISSN 2056-6387. doi: 10.1038/s41534-019-0210-7. URL <https://www.nature.com/articles/s41534-019-0210-7>. Bandiera\_abtest: a Cc\_license\_type: cc\_by Cg\_type: Nature Research Journals Number: 1 Primary\_atype: Research Publisher: Nature Publishing Group Subject\_term: Information theory and computation;Quantum physics Subject\_term\_id: information-theory-and-computation;quantum-physics.
- [99] Tameem Albash and Daniel A. Lidar. Decoherence in adiabatic quantum computation. *Physical Review A*, 91(6):062320, June 2015. doi: 10.1103/PhysRevA.91.062320. URL <https://link.aps.org/doi/10.1103/PhysRevA.91.062320>. Publisher: American Physical Society.